Clinical Grade Active Guidewire and Catheter for Interventional Cardiovascular MRI

by

Özgür Kocatürk

M.S, Biomedical Engineering, Biomedical Engineering Institute, 2002

Submitted to the Institute of Biomedical Engineering
in partial fulfillment of the requirements
for the degree of
Doctor
of
Philosophy

Boğaziçi University
Month 2009

Clinical Grade Active Guidewire and Catheter for Interventional Cardiovascular MRI

APPROVED BY:

Assoc. Prof. Dr. Cengizhan Öztürk (Thesis Advisor)	.....
Prof. Dr. Ahmet Ademoğlu	.....
Prof. Dr. Ergin Atalar	.....
Assistant Prof. Dr. Arda Yalçınkaya	.....
Assistant Prof. Dr. Şenol Mutlu	.....

DATE OF APPROVAL: 7 May 2009

ACKNOWLEDGMENTS

I would like to convey my special thanks to my advisor, Assoc. Prof. Cengizhan Öztürk for his kind and warm support throughout my graduate studies.

As for Dr. Robert J. Lederman, I will always remember the support, guidance and opportunities presented. Also, a bundle of thanks to Christina E. Saikus for all the help that played an important role in the completion of this work.

To my parents, my brother, my wife and my son, thanks for your endless support and love.

ABSTRACT

Clinical Grade Active Guidewire and Catheter for Interventional Cardiovascular MRI

The success and safety of interventional magnetic resonance imaging (MRI) procedures requires conspicuous intravascular instruments that can be distinguished from surrounding tissues. In this dissertation work, an "active" (receiver-coil) clinical grade vascular guidewire and guiding catheter were developed with enhanced visibility and favorable mechanical characteristics for MRI guided cardiovascular interventions.

Both 0.035-inch guidewire and 7 Fr guiding catheter were designed combining two different antenna designs on independent channels. The devices incorporate a loop antenna to visualize the tip and determine orientation, and a dipole antenna to visualize the whole guidewire shaft. The MRI visibility performance and RF safety tests were performed at 1.5T in vitro and in vivo in swine.

The two channel active guidewire design provided accurate tip position information with 0.97 ± 0.42 mm and novel active shaft visibility technique was introduced to polymer based guiding catheter successfully without sacrificing device size or handling. Mechanical testing comparison with several commercially-available guidewires demonstrated that the new guidewire design provides the desired stiffer distal tip, moderate torquability, and pushability suitable for vascular applications. The RF power threshold and limitations were determined to provide reasonable amount of heating during MRI examination. This may enable a range of interventional procedures using real-time MRI.

Keywords: Interventional Magnetic Resonance Imaging, Active instrument, Equipment Design, Catheterization

ÖZET

Girişimsel Kardiyovasküler Manyetik Rezonans Görüntüleme için Klınikte kullanıma Uygun Çok Kanallı Klavuz Tel ve Kateter Tasarımı

Girişimsel tedavi yöntemlerinin Manyetik Rezonans Görüntüleme (MRG) altında başarılı ve güvenilir bir şekilde uygulanabilmesi için anatomik görüntüden kolaylıkla ayırt edilebilecek damariçi cihazlara gereksinim vardır. Bu amaçla klinikte kullanılmak üzere üstün görünebilirlik ve mekanik özelliklere sahip aktif klavuz tel ve kateter geliştirilmiştir.

0.035 inç çapındaki klavuz tel ve 7 Fr çapındaki kateter, bağımsız kanallara sahip iki farklı anten tasarımını birleştirerek gerçekleştirilmiştir. Klavuz tel ve kateter içerisine yerleştirilen halka anten sayesinde telin uç kısmı ve damar içindeki oryantasyonu; dipol anten sayesinde de cihazlarin tüm şaftı görüntülenebilmektedir. Klavuz tel tasarımının mekanik özellikleri aynı amaçla kullanılan ticari ürünlerle kıyaslanmıştır. MRG altında görünebilirlik ve Radyo Frekans (RF) güvenlik testleri 1.5 Tesla MR cihazı kullanılarak gerçekleştirilmiştir.

Klavuz telin fiziksel ucu 0.97 $\pm$ 0.42 mm hassasiyetle görüntülenmiş; metal tel örgüler kullanılarak geliştirilen anten tasarımı sayesinde MR uyumlu kateterin de tüm şaft görünebilirliği sağlanırken; kateterin ve klavuz telin standart profili ve gerekli mekanik özellikleri korunmuştur. Klavuz telin MRG altında kullanımı sırasında uygulanabilecek azami RF gücünün miktarı ısınma testleri sırasında belirlenmiştir.

Anahtar Sözcükler: Girişimsel Manyetik Rezonans Görüntüleme/metod, aktif cihaz, cihaz tasarımı, Kateterizasyon

TABLE OF CONTENTS

LIST OF FIGURES

LIST OF TABLES

LIST OF SYMBOLS

c	specific heat constant
δ_s	skin depth
ϵ	dielectric constant
Γ	reflection coefficient
μ	permeability constant
ω	frequency
ρ_m	the mass density
σ	electrical conductivity constant
τ	scan time

LIST OF ABBREVIATIONS

ASTM	American Society for Testing and Materials
BNC	Bayonet Neil Concelman
CNR	Contrast-to-noise Ratio
DC	Direct Current
FDA	Food and Drug Administration
FEP	Fluorinated Ethylene Propylene
FOV	Field of View
GUI	Graphical User Interface
HEC	Hydroxy Ethyl Cellulose
IDTE	Intravascular Device Test Equipment
iMRI	Interventional Magnetic Resonance Imaging
MMCX	Micro-miniature Connections
MRG	Manyetik Rezonans Görüntüleme
MRI	Magnetic Resonance Imaging
MR	Magnetic Resonance
NEMA	National Electrical Manufacturer Association
PAA	Polyacrylicacid
PIN	Positive-intrinsic-negative
Q	Quality Factor
RF	Radio Frequence
ROI	Region of Interest
RT	Real-Time
SAR	Specific Absorbtion Rate
SD	Standard Deviation
SNR	Signal-to-noise Ratio
SSFP	Steady State Free Precession
STD	Standard Deviation
TE	Echo Time

TEM	Transverse ElectroMagnetic
TR	Repetition Time
WB	Whole Body

1. Introduction

1.1 Overview of the Dissertation

This doctoral research was motivated by the desire to develop a clinical grade active guidewire and guiding catheter to develop safer intravascular procedures for minimally invasive catheter-based cardiovascular interventions under MRI. Although several experimental design have been proposed in the past, none of these has demonstrated simultaneous visualization of the distal tip and shaft in a 0.035 inch active guidewire and polymer based catheter. It is aimed to develop a clinical grade multi channel active MR compatible guidewire and catheter with adequate mechanical properties and visibility during imaging.

Chapter 2 contains a description of the active two channel guidewire design and both visibility performance under MRI and mechanical testings.

Chapter 3 contains the detailed description of a test method to compare the signal to noise ratio of antenna channels of identical active device prototypes.

Chapter 4 introduces a novel loopless antenna design method by using braiding layers of polymer catheter shaft. It outlines the manufacturing details and provides in vitro and in vivo visibility tests also.

Chapter 5 outlines RF safety tests performed for both active two channel guidewire and guiding catheter. It outlines the boundary conditions in terms of safe insertion length, horizontal offset from isocenter and scanner isocenter landmark position.

Chapter 6 provides summary of the specific aims and provides suggestions for future development and directions for developed prototypes.

1.2 Interventional Magnetic Resonance Imaging

MRI is principally used in a diagnostic capacity and recent advancement in MR technologies such as better gradient performance, new K-space trajectories and innovations in MR receiver hardware [1] made it possible to use this imaging modality for guidance and evaluation of therapeutic interventions. This relatively new research area is called interventional magnetic resonance imaging (iMRI) which deals with topics such as MR-guided ablation procedures [2], biopsies [3], cryotherapy and vascular procedures [4, 5, 6]. At present, X-ray fluoroscopy is the widely used imaging modality for guiding vascular interventions. The manipulation of the interventional instruments can be tracked easily due to their radiopacity and the vascular anatomy can be visualized by using iodinated contrast agents [7]. However, there are some patient population for which the use of x-ray fluoroscopy is problematic. For example, the ionizing radiation dose should be closely monitored for pediatric patients who are considered more sensitive to radiation. Even low-level exposure to ionizing radiation may contribute to the long-term risk of malignancy [8]. Also, the use of contrast agent may be prohibited for the patients who have an allergy to iodinated contrast agents [9] or patients who have renal insufficiency [10]. Especially during complex interventional procedures, X-ray exposure for both patient and operator increases dramatically. Also protective lead aprons may cause musculoskeletal injury to operators over years. The use of iMRI for guiding vascular procedures provides significant advantages relative to X-ray fluoroscopy. First of all, MRI does not involve ionizing radiation. Also related anatomy can be visualized with superior soft tissue contrast using desired image plane orientation and multiple contrast mechanisms. In addition, MRI can also provide vast number of functional parameters such as blood flow velocity, temperature, tissue perfusion or brain activation during acquisition of anatomical images [7]. Although real time MRI can provide 5-10 frames per second for imaging speed compare to X-ray fluoroscopy 15 frames per second with a reduced pixel imaging matrix such as 192 x 128 (compare to 1024 x 1024 pixel matrix of fluoroscopy), it still provides comparably rich anatomy information [11]. In MRI, image acquisition speed can be accelerated by using parallel imaging techniques that acquire undersampled datasets by skipping some phase-encoding lines and then reconstruct the missing data by exploiting the

sensitivity profiles of receiving coils [12]. Also custom design interactive programs by using external reconstruction computers operating in parallel can provide the multiple scan plane selection and display these slices in their relative anatomical position [13]. In addition, it can process and highlight individual receiving channels, especially those attached to active intravascular instruments. However, Interventional MRI still suffers from the limited availability of interventional instruments that are safe and visible under MRI.

1.3 Instrument Visualization Under MRI

The accurate position determination of interventional devices such as needles, catheters and guidewires is required to perform successful invasive interventional procedures guided by MRI. Interventional catheter devices for X-ray fluoroscopy procedures have intrinsic imaging signatures based on their X-ray attenuation that indicate device tip or its important segments. The device tip is most likely to injure, disrupt or perforate diseased tissue and generally requires the most attention. The device shaft must deliver a range of interventional devices which may be large, rigid, and bulky. Operators must identify devices uniquely, usually based on imaging "signatures" or appearance, by movement in response to operator manipulation, or by computer synthesized display [14]. However, invasive instrument visualization for interventional MRI procedures is more challenging and usually requires more complicated device structure compare to conventional devices. There are mainly two visualization methods that are called passive and active visualization.

1.3.1 Passive Visualization

Passive visualization usually relies on a difference in magnetic susceptibility between the instrument and the related anatomical tissue which creates a local magnetic field inhomogeneity. This field inhomogeneity causes $T2^*$ shortening, local signal loss and therefore misregistration in non-spin-echo sequences. Passive devices may cause

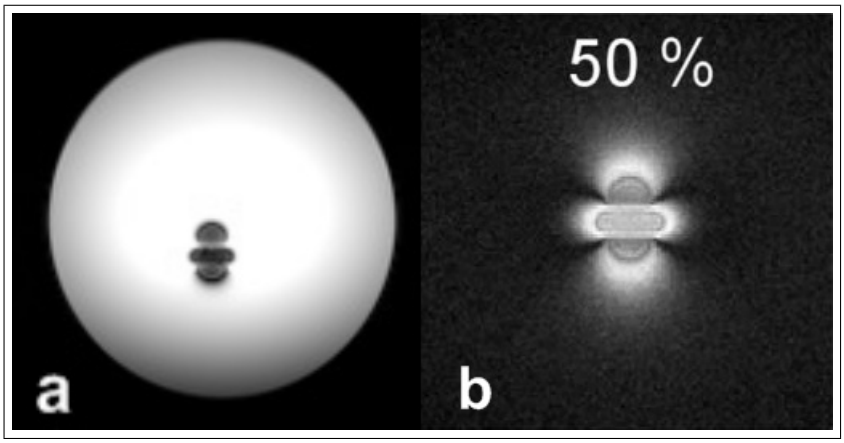

Figure 1.1 (a) Observed negative contrast of magnetic dipole moment of stainless steel marker at the 3T MRI scanner [16]. (b) A clear positive contrast is observed by using 50% rephrasing gradient strength during gradient echo imaging.

negative contrast through local distortions of the magnetic field (black spots) or positive contrast through enhanced local signal (bright spots) (Figure 1.1). Positive contrast can also be obtained by using off-resonance imaging sequences intended to make susceptibility markers appear bright. In general, after excitation, the slice selection gradient dephases the spins. When the rephrasing gradient is applied, the gradient balance is restored and signal remains conserved in spatial regions with a negative local gradient whereas other regions experience signal loss [15].

Black spots can reflect many causes, and those created by passive devices (signal voids from intentional magnetic susceptibility artifacts) have low contrast compared with tissue. Black spots also suffer volume averaging more readily than do sources of intense signal (such as local receiver coils). Susceptibility markers must have a high magnetic moment to induce an adequate artifact at a variety of scan techniques and tracking speeds. In other words, they must have sufficient contrast to noise ratio (CNR) with respect to the background in order to distinguish device in thick slab images. The CNR can be calculated as

$$CNR = -\frac{S_m}{\sigma_s} \tag{1.1}$$

With S_m the signal loss induced by marker, which is negative in the subtraction image, and σ_s is the noise in the background of the subtraction image. Because MR scanner

provides strong magnetic field with applied gradients, the passive marker material is magnetized homogenously. So magnetic moment (m) can directly be related to B_0 [17]. This relation can be written as

$$m(B_0) = \Delta M(B_0)V \tag{1.2}$$

With ΔM the magnetization difference between the marker and tissue and V the volume of the marker. For diamagnetic and paramagnetic materials, m is proportional to B_0. For other types of magnetism like ferro- and ferrimagnetism, a nonlinear relation exists. For a marker of subvoxel volume, the field distortion can be approximated by a dipole field [18].

$$\Delta B_z(x, y, z) = \frac{\mu_0 m(B_0)(2z^2 - y^2 - x^2)}{4\pi(x^2 + y^2 + z^2)^{\frac{5}{2}}} \tag{1.3}$$

With μ_0 the permeability in free space and x,y and z the spatial coordinates with ΔB_z and B_0 in z-direction.

The magnetic moment of the marker needs to be large with regard to the size of the marker and CNR of the artifacts. This excludes diamagnetic and weakly paramagnetic materials, since their magnetization is too low to create a large magnetic moment with only a small amount of material. High tracking speeds can be achieved when short echo times are used, and this requires an even higher magnetic moment for heavy $T2^*$ -weighting around the marker. Then, strongly paramagnetic markers become bulky in order to realize an adequate magnetic moment. Biocompatibility and safety can be achieved by embedding into another medium, e.g. the coating of the device. Again, easily magnetizable materials are preferred, since a lower concentration of marker material is needed. The optimal applicability regarding field strength may be realized with a field-strength-independent magnetic moment of the marker. Such a nonlinear magnetic property is partly exhibited by ferri- and ferromagnetic materials. In certain applications that allow to use large profile devices, CO_2-filled balloons can be used [19] to displace water in order to make devices conspicuous. The large profile

balloon catheters can also filled with T2*-shortening agents to make them conspicuous and distinguish them from blood during bright-blood imaging [20]. The susceptibility artifact depends on the shape of the interventional instrument, its orientation relative to the main magnetic field, relative susceptibility artifact difference between the related tissue and the device material and the bandwidth per pixel used acquire the image. Although passive instrument construction is comparably simple it is not attractive due to low contrast-to-noise ratios and usually difficult to distinquish the instrument image "signature" compared with image artifacts. Vascular anatomy in MR images may have long black lines that can be confused with the negative contrast created by in-plane susceptibility base instrument visualization under MRI. This is not acceptable especially if the intravascular device is positioned next to vital anatomical structures for interventional procedures. Another disadvantage of susceptibility-induced visualization is that negative contrast spots are much larger than the physical dimensions of the related passive markers. So it causes to extinguish signal from surrounding target tissue near the passive marker. Although positive contrast looks attractive in comparison to the negative contrast, bright signal strength depends on the marker orientation with respect to the main magnetic field of magnet and also detracts from tissue imaging [19]. Due to given limitations, the use of passive markers for instrument visualization is inferior for interventional procedures.

1.3.2 Active Visualization

Active visualization based on embedded antenna techniques generally employs a direct electrical connection between the device and the MR scanner or an external power source. Active visualization techniques can be grouped into three classes.

1.3.2.1 Direct Current Method. The first class of active visualization technique, in which a local field inhomogeneity is generated to provide instrument visualization, functions by sending small amounts of direct current through the transmission wires during imaging Figure 1.2. This small amount ellectrical current acts to cause

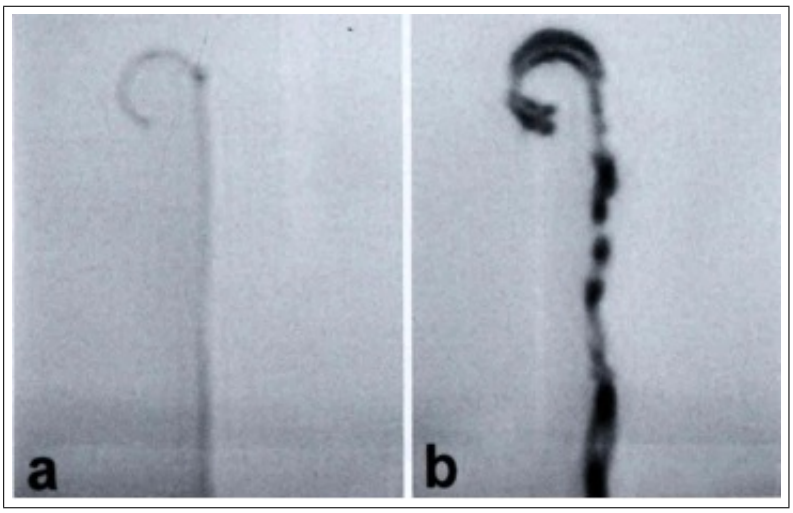

Figure 1.2 (a) A handmade 5 Fr catheter prototype image acquired in a waterbath with no current applied and (b) with a direct current of 150 mA [21].

magnetic field inhomogeneity locally [21]. This technique relies on the susceptibility differences like the previously described passive methods. Similarly, because field strength, device orientation to field and scanning parameters determine the local effects, it does not give consistent, easily distinguishable visualization markers.

1.3.2.2 Inductive Coupling. This technique relies on the inductive signal coupling between RF coils that are tuned to Larmour frequency. The solenoid coil that is tuned to Larmour frequency with the help of LC circuit design is embedded into catheter body. During MR scan, two different modes can provide enough contrast relative to background to visualize the active device. First, in body coil RF transmit mode, low flip angle excitation pulses of a real time imaging sequence are multiplied inside and in the close vicinity of the resonant embedded distal solenoid coil, resulting in locally increased effective flip angles. The low flip angle sequence will cause relatively lower received signal from the background anatomy, so a positive contrast appears between the distal catheter coil and the background. Second, in RF signal receiving mode, the resonant distal catheter coil picks up the MR signal from excited spins in its immediate vicinity, resulting in a B_1 field vector that can be inductively coupled to that of a surface RF coil. Both catheter coil and surface coil act as a local signal amplifier in deep-sited regions (Figure 1.3) [22].

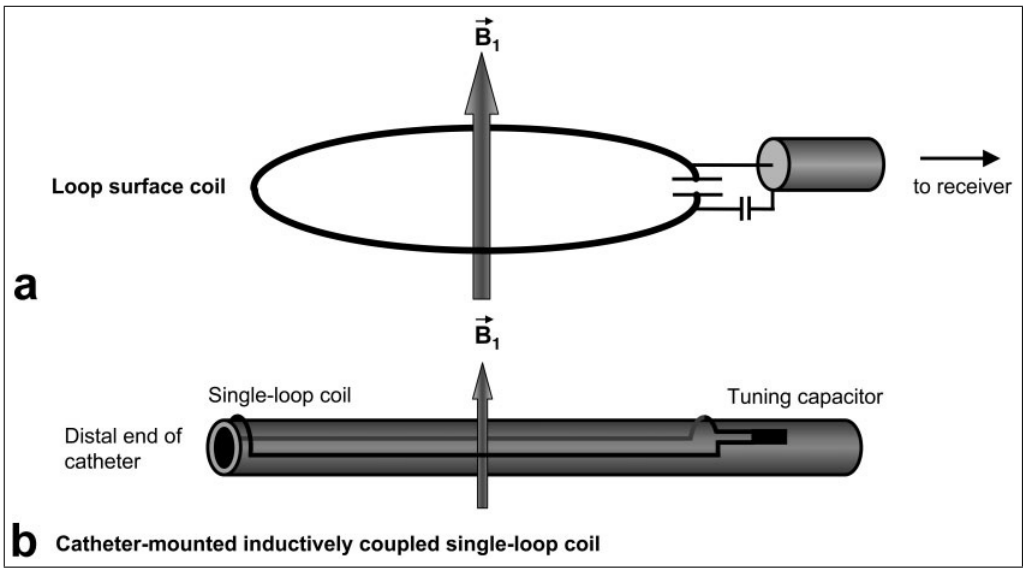

Figure 1.3 Schematic of inductive signal coupling between (a) loop receiver surface coil of scanner and (b) closed loop embedded coil into catheter distal tip. RF transmit mode, the resonant catheter loop coil multiplies the excitation flip angle. In RF receive mode, the resonant catheter coil picks up the MR signal in its vicinity, resulting B_1 vector can be inductively coupled to loop receiver surface coil of the scanner [22].

This technique looks attractive because it eliminates transmission line that may subject to RF heating during scan and also compromises handling of active instruments due to required wire connection between the device and scanner. However, inductive coupling between the body RF coil and the catheter RF coil in transmit mode and the catheter RF coil and the surface RF coil in signal receiving mode is highly dependent on the orientation of the coils relative to each other (Figure 1.4). Therefore this technique does not function well especially the interventional instrument is advanced into complex vessel curvatures. Also inductive coupling requires low flip angle imaging that limits the surrounding tissue context.

1.3.2.3 Capacitive Coupling. In this active visualization technique, a miniature solenoid coil [23, 24] or a dipole receive antenna [25, 26] is incorporated the device structure. Loop or dipole antenna that is positioned within the device detects the MR signal generated locally as excited spins relax back into equilibrium distribution. Several antenna designs have been explored in the past for interventional devices. The embedded receiver antenna that is connected to the scanner via a thin coaxial cable

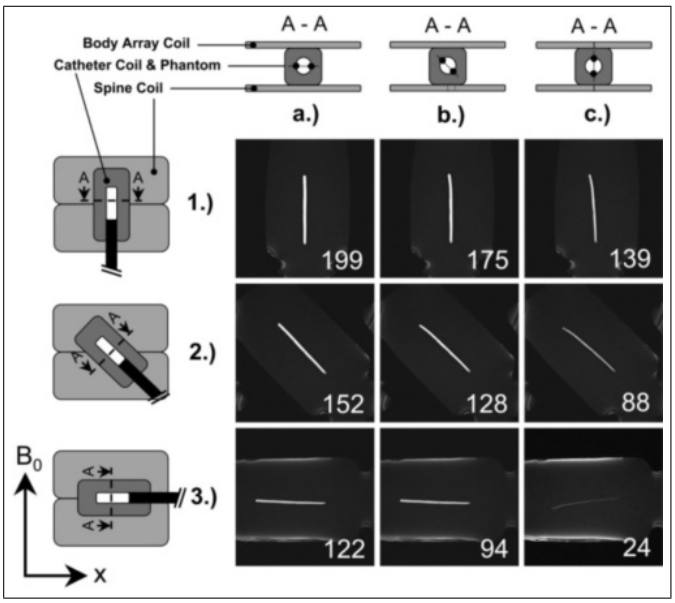

Figure 1.4 Schematic of phantom study performed by Harald Quick et al [22] to evaluate the signal coupling between the catheter coil and scanner coil in terms of SNR. Drawings in the left column represents the relative position of catheter coil longitudinal axis relative to B_0. Drawings in the first row show the orientation of the coil plane relative to the surface coil. The figures on the right bottom corner shows the SNR value achieved in related position.

passing through the catheter could in theory provide a robust signal, identifying the instrument tip location or shaft position and orientation with high contrast.

Solenoid Coil

Solenoid coil is basic form of loop antenna element in which the wire is coiled in a helical pattern to create a cylindrical shape as shown in Figure 1.5a. Solenoid micro coils are connected to the MR system through the use of coaxial transmission lines which may serve both detuning and signal transduction purposes. Loop antenna signal sensitivity for small-loop receivers falls off very rapidly ($1/r^3$, where r is the radial distance from the loop) [27]. To improve longitudinal coverage, long-loop intravascular antennas were subsequently investigated. For these long, narrow loop receivers (in which the loop length is much greater than its width), sensitivity falls off as $1/r^2$ [28]. Despite improved longitudinal coverage, these receivers produce limited SNR when conductor separation is small as can be seen in Figure 1.5b.

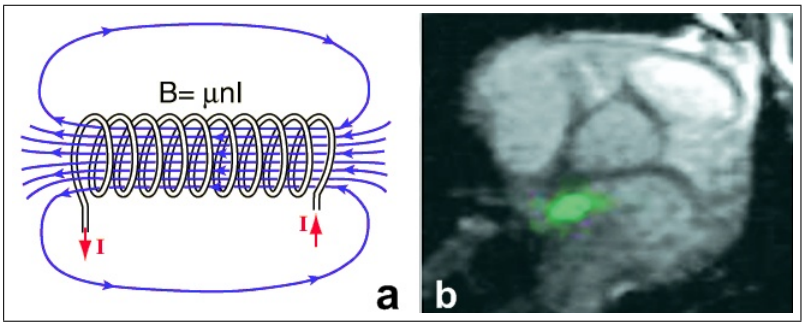

Figure 1.5 (a) Schematic representation of solenoid coil overlaid on field line plot. (b) porcine catheter tip tracking experiment in vivo using loop antenna.

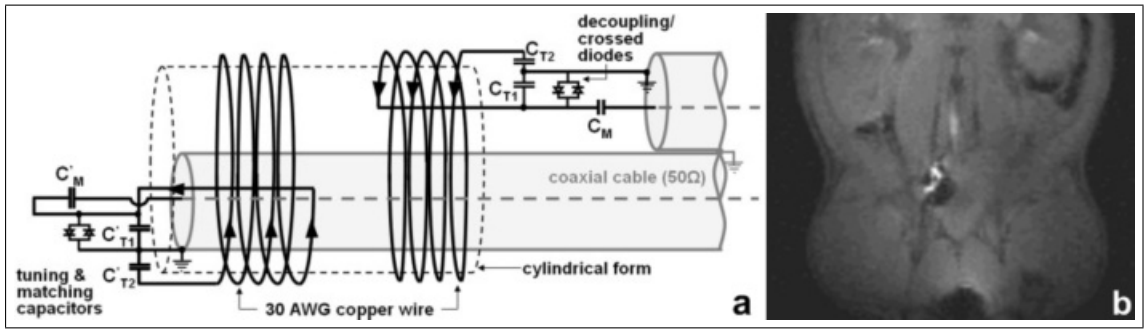

Figure 1.6 (a) Electrical schematic of the opposed solenoid catheter coil. (b) porcine catheter tip tracking experiment in vivo using opposed solenoid coil [29].

Opposed Solenoid

The opposed solenoid loop antenna is based on groups of helical loops separated by a gap region, with current driven in opposite directions in the helical loops on either side of the gap, as shown in the schematic of Figure 1.6. The gap provides the small area of homogenous longitudinal magnetic field that makes it a good candidate for especially using as an imaging coil within and beyond the vessel wall. However, it has a small area of homogenous longitudinal coverage compared with the dipole antenna.

Loopless Antenna

The loopless antenna is a simple coaxial transmission line with extended inner core. The antenna sensitivity falls off as 1/r where r is the radial distance from the antenna longitudional axis. The loopless antenna signal intensity can be improved

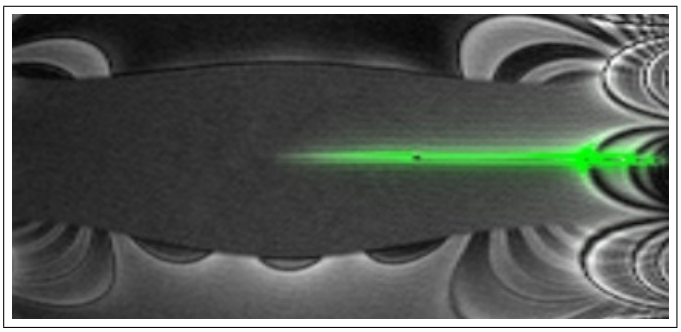

Figure 1.7 The image of a water filled phantom acquired using both body coil and dipole antenna. The signal received from dipole antenna colored using special software.

by increasing insulation layer (insulation broadens the SNR distribution) and helical winding over extended core inductor (winding allows for improved SNR near the tip of the antenna) [30]. The loopless design also suffers in that coil sensitivity falls to zero near the tip, making it unsuitable for interactive navigation through obstructed or tortuous anatomy without further modification Figure 1.7.

Transmission Line

The transmission line connects the RF coil or dipole antenna through the instrument body to external tuning, matching and decoupling electronic circuits. These electronic circuits are usually placed within an RF shielded box that is connected with an interface plug to the surface coil port of the scanner Because the transmitting signal is radio frequency (RF) signal with larmour frequency, the transmissional lines are usually coax cables or twisted pairs [23, 28, 31]. Single active device may have more than one receiver channel by incorporating several loop or dipole antennas together and then each separate receiver channel is attached to scanner for reconstruction. Also each catheter channel can be displayed with different color to impart specificity to catheter-related signal [32, 33].

2. Active Guidewire Design and Production

Interventional guidewires are indispensible for introducing procedure related catheter into a blood vessel. They are remotely operated to establish a path through chamber and tissue spaces and then are used to position additional catheters that deliver information, energy, material and implants. For MR guidance of vascular interventions to be safe, the interventionalist must be able to visualize the tip location and distal shaft of the MRI compatible guidewire relative to the vascular system and surrounding anatomy. A number of instrument visualization approaches under MRI have been developed including both passive and active techniques. However, none of these techniques provides satisfactory result in terms of both instrument tip and shaft visualization at the same time. Visualization of shaft only is not enough to advance guidewire through tortuous vessels due to the risk of puncturing vessel wall and visualization of a single point is not sufficient to steering an active guidewire in complex vessel territory [34]. When high signal amplification along the entire length is desired, traditional active visualization techniques often involve equipping a guidewire with a dipole antenna [26]. Dipole antennas − essentially coaxial transmission lines with extended inner conductors − have spatial coverage along their length and therefore impart visibility to the whole shaft of the active instrument. However, dipole antennas have limited sensitivity near their tips, which makes them unsuitable for interventional procedures which require careful intravascular navigation [35]. Alternatively, miniaturized RF loop coils embedded into the instrument body [36] impart only localized spatial coverage for tracking or visualizing single points. Multiple miniature loops must be incorporated along the length of the device to visualize the whole shaft [37, 38, 39]. The tip and shaft visualization of the 0.035 inch guidewire at the same time requires more than two different embedded antenna designs and it is quite challenging due to the dimensional restrictions. Miniaturized RF loop coil imparts only localized spatial coverage for visualizing single bright point. By contrast, dipole antenna has spatial coverage along its length and therefore imparts visibility to the whole shaft of the active instrument.

2.1 Electrical Design of Active Guidewire

Nitinol material is the best material candidate for designing interventional MRI receiver antenna among other MRI compatible materials such as platinum, titanium and cobalt-chromium due to its superior mechanical properties that help to maintain all the required mechanical characteristics of the clinical grade guidewires. However, because nitinol is not a good conductor, there are several factors that need to be considered carefully to achieve an efficient antenna design on it.

2.1.1 Skin Effect

The resistance of a conductor to alternative current is different than its resistance value for direct current. A consequence of Maxwell's equations is that near-perfect conductors (e.g metals) conduct alternative current only a certain depth that is proportional to wavelength of the signal. As the frequency is increased, an increased magnetic field at the center of the conductor presents an impedance to the charge carriers, thus decreasing the current density at the center. This decreases the effective cross section of the conductor at the high frequencies and thus increases its resistance. The resistance increase is called the skin effect. It becomes significant beginning around 1 MHz (depending on the size of the conductor) and is much more pronounced in high frequencies where practically all the current flows in a very thin layer near the conductor's surface [40]. For this reason, a hollow tube and a solid rod of the same diameter and same metal could have practically the same resistance at high frequencies.

The depth into the conductor at which the charge carrier current density falls to 1/e is knows as the skin depth (δ_s) and it is a function of the frequency (ω) and the permeability (μ) and conductivity (σ) of the medium:

$$\delta_s = \sqrt{\frac{2}{\omega\mu\sigma}} \tag{2.1}$$

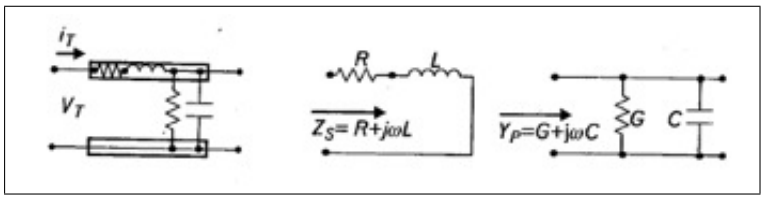

Figure 2.1 Characteristic impedance of a transmission line can be derived from short-circuited series impedance and open-circuited shunt admittance of its incremental segment.

2.1.2 Characteristic Impedance

For all Transverse Electromagnetic Mode (TEM) transmission lines a simplified theoretical analysis may begin with the equivalent circuit in which each incrementally small length of line is modeled as a series of impedance and a shunt admittance that can be seen in Figure 2.1. A wave traveling along the line has voltage, V_T, and current, I_T, related by the characteristic impedance of the line segment, Z_{TL} [41].

$$Z_{TL} = \frac{V_T}{I_T} \tag{2.2}$$

Each inductor in Figure 2.1 represents the inductance of a very short section of one wire and each capacitor represents the capacitance between two such short sections. The inductance and capacitance values per unit of line depend on the size of the conductors and the spacing between them. The smaller the spacing between the two conductors and the greater their diameter, the higher the capacitance and the lower the inductance. Each series inductor acts to limit the rate at which current can charge the following shunt capacitor, and in so doing establishes a very important property of a transmission line: its surge impedance, more commonly known as its characteristic impedance (Z_0):

$$Z_0 = \sqrt{\frac{R + i\omega L}{G + i\omega C}} \tag{2.3}$$

where R is the series resistance, L is series inductance, G is shunt conductance and C

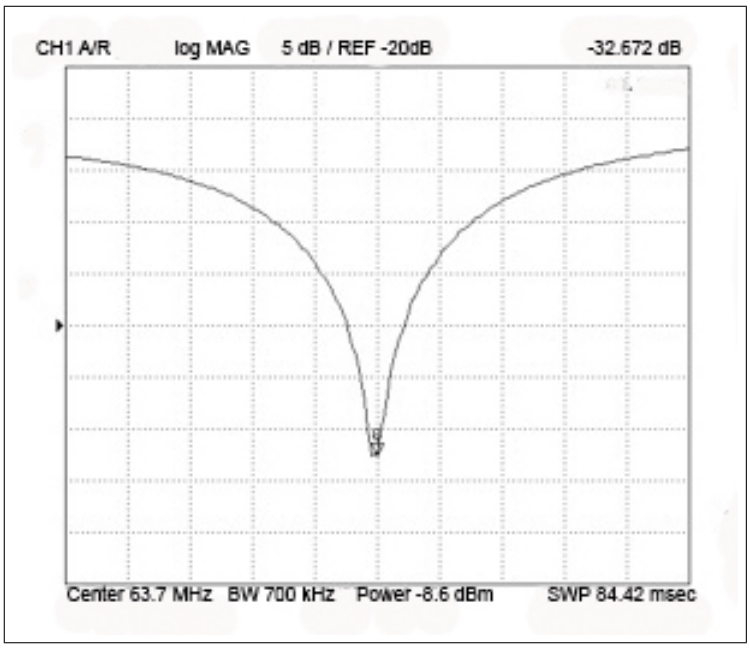

Figure 2.2 The graph represents the reflection loss as log magnitude in dB of a loop antenna design under development.

is shunt capacitance per unit length.

2.1.3 Return Loss

Reflection coefficient, Γ, is defined to show what fraction of an applied signal is reflected when a Z_0 source drives a load of Z_L.

Forward and reflected traveling waves inside a transmission line can be separated and measured by using directional couplers. The reflection coefficient is a ratio of two normalized traveling voltage waves. Its magnitude squared represents the reflected power. Converted to decibels, it is called the return loss (RL_{dB}):

$$RL_{dB} = -10log\left|\Gamma\right|^2 = -20log\left|\Gamma\right| \tag{2.4}$$

The return loss evaluates the difference between the reflected wave and the incident wave in decibels as can be seen in Figure 2.2.

Return loss does not have phase information and it is primarily used in production testing where the goal is to reject assembled parts that do not meet a specified minimum limit. This limit value will be set depending on the phantom test results of the designed antenna [40].

2.1.4 Effect of Insulation Layer

Especially for the loopless antenna, all of the antenna capacitance exists between the two poles of the antenna, with the body and antenna insulation acting as the dielectric. With added insulation, the current profile on the antenna is broadened and thus charge density is decreased. This reduced charge density results in lower electric fields and less power deposition in the body, and hence a reduced contribution to noise resistance. At the same time, however, there is an increase in the amount of tissue wherein "magnetic losses" occur (i.e., the amount of tissue containing eddy currents) [42], because of the broadening of the current distribution. This effect will tend to raise noise resistance, offsetting the decrease due to the distributed capacitance effect. Considering both of these effects, there is little net change in SNR with the addition of antenna insulation. It means that dipole antenna can keep its visibility performance after the required heat shrink insulation layer and hydrophilic coating is added over the guidewire shaft.

2.1.5 Quality Factor "Q"

Quality Factor (Q) of a MRI receiver coil is a measure of the "quality" of the resonant circuit. The resonant circuit should respond to frequencies close to the natural frequency, in this case the Larmor frequency for the targeted MRI application, more strongly than they respond to other frequencies. The characterization of this response is called as the circuit Q. Generally the larger the value of the Q means the lower loss of the resonant circuit. In other words, larger Q value also means increased SNR performance of the antenna [43]. Q factor can be defined in several ways mathematically. First, Q

factor can be defined as the reactance of a circuit divided by the resistance.

$$Q = \frac{\omega_0 L}{R} \tag{2.5}$$

where ω_0 is resonance frequency, L is inductance of the antenna, R is the antenna resistance.

Also, it can be defined as the ratio of the resonant frequency divided by the bandwidth.

$$Q = \frac{f_c}{f_2 - f_1} \tag{2.6}$$

where f_c is center frequency, (f_2-f_1) is bandwidth.

Using the network analyzer with an S-parameter test set, the Q of a resonant circuit can be determined using either S_{11} (reflection type) and/or S_{21} (forward transmission gain-type) measurement methods.

2.1.6 Antenna Impedance Matching

Antenna impedance matching is necessary procedure to provide the maximum possible transfer of power between a source and its load [40]. In active guidewire application, any unnecessary loss in a circuit that is already carrying extremely small signal levels simply cannot be tolerated. Therefore, extreme care is taken during the initial design of such a front end to make sure that each device in the chain is matched to its load. In dealing with ac waveforms, the maximum transfer of power from a source to its load occurs when the load impedance (Z_L) is equal to the complex conjugate of the source impedance [40]. Complex conjugate simply refers to complex impedance having the same real part with an opposite reactance. Thus, if the source impedance is Z_s= R + jX, then its complex conjugate would be Z_s = R - jX. The maximum power is transferred from a source to its load if the load resistance equals the source resistance. So, in this case maximum transfer of power does occur when the load impedance is

the complex conjugate of the source. The source (Z_s) with a series reactive component of +jX (an inductor), is driving its complex conjugate load impedance consisting a -jX reactance (capacitor) in series with R_L. The +jX component of the source and -jX component of the load in series cancel each other, leaving only R_S and R_L. Since R_S and R_L are equal, maximum power transfer is occurred. In general, any source reactance is resonated with an equal and opposite load reactance; thus, leaving only equal resistor values for the source and the load terminations. There is infinite number of possible networks which could be used to achieve the impedance matching.

The internal MRI receiver coils usually are tuned and matched to the larmour frequency at the end of proximal end of the transmission line. This tuning technique uses the impedance transformation characteristics of coaxial transmission line to match the antenna to the characteristic impedance of interest. The coil impedance is transformed by the transmission line.

$$Z_s = R_c \frac{1 + |\Gamma| e^{i\phi}}{1 - |\Gamma| e^{i\phi}} \tag{2.7}$$

where Z_s is the transformed impedance, R_c is the characteristic impedance of the transmission line and $|\Gamma|$ is the magnitude of the reflection coefficient. The angle ϕ that represents the total phase shift to the signal can be calculated by

$$\phi = \Psi - 2\beta s \tag{2.8}$$

where β is the phase shift per unit length of the transmission line, s is the line length, and Ψ is the phase shift due to reflection at the load. So required transmission line length can be determined from ϕ.

2.1.7 Smith Chart

To determine the correct circuit elements types and values during impedance matching, Smith chart is used as an indispensable tool. The Smith chart shown in Figure 2.3 has a center value of 50 ohms for the use of impedance bridges that measure

directly in impedances. The Smith chart consists of a family of circles and a family of arcs which intersect each other at right angles. The circles are tangent at a common point at the right of the chart. Points along any of these circles represent the same value of resistance R. Larger circles correspond to lower values of R, down to zero for a circle equal to the chart diameter. Smaller circles represent higher values of resistance, approaching infinity as the circle becomes smaller. The family of arcs represents constant values of the reactance +jX and -jX. These arcs all pass through the point at the right of the chart, and have their radii along a vertical line passing through that point. jX equals to zero at the left of the Smith chart and increases in both directions, inductive reactance +jX clockwise and capacitive reactance -jX counterclockwise. As the right of the chart is approached, both +jX and -jX increase to infinity, with the largest labeled being 2500 ohms.

2.1.8 Antenna Detuning during RF Transmission

In all MRI experiments in which embedded antennas are used for signal reception, antenna detuning is necessary during RF transmission to prevent high voltages from being induced in the receiving antenna and other circuit elements. The potentially high voltages and the induced electrical fields pose patient safety hazard and disrupt the desired uniform excitation filed generation required for excitation; this may lead to particular localized effects in interventional MR imaging. Detuning is often achieved by applying a voltage to a special portion of the electronics of the receiver coil and causes the receiver coil's resonant frequency to change.

2.2 Mechanical Design of Active Guidewire

A guidewire has an elongated solid body about which a catheter may be threaded for guidance to a target location in a vasculature passageway of a body. During the procedure, the guidewire might be advanced through small multi branched vessel paths with high curvature sections. And also it should support to required catheter that is

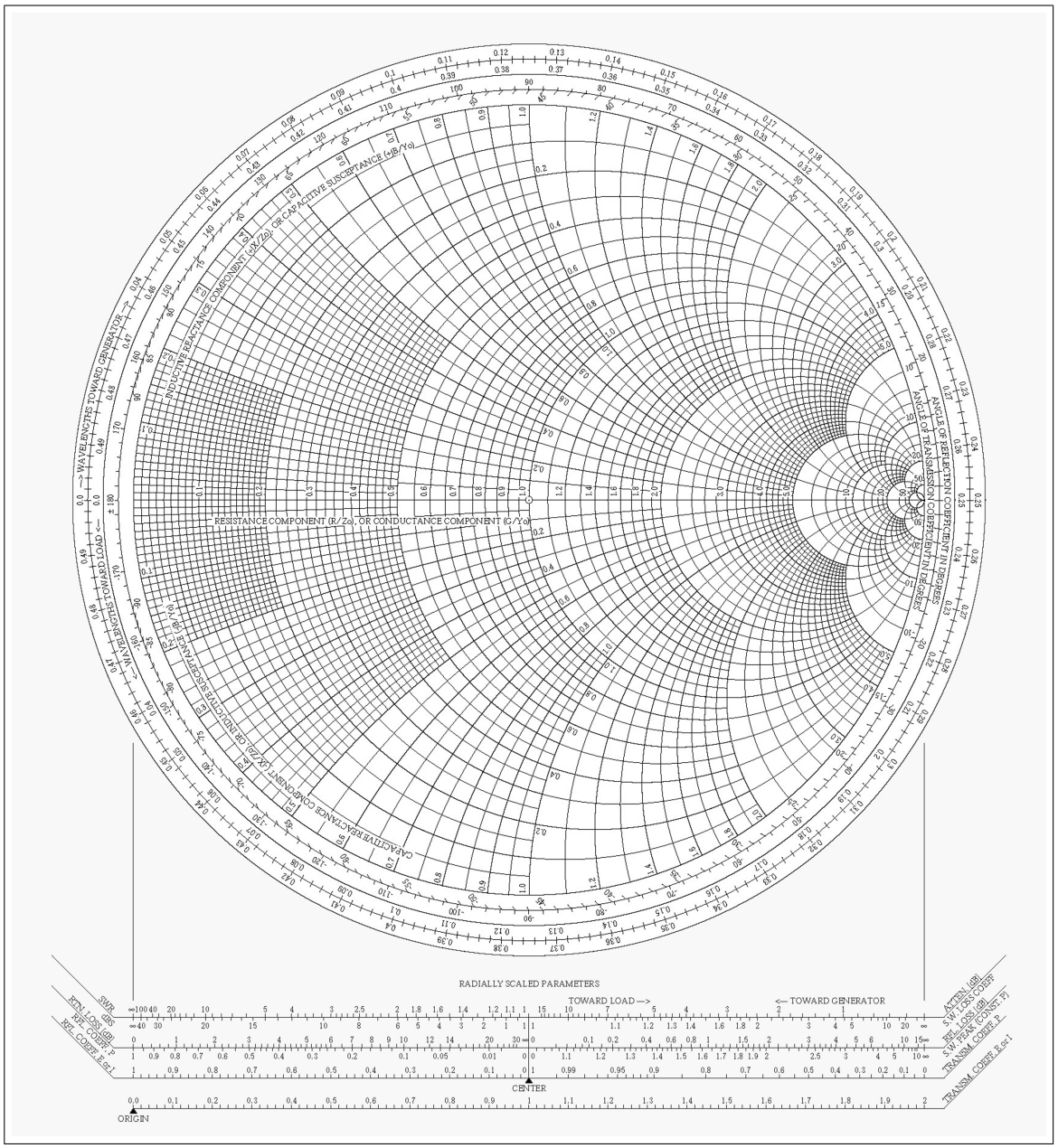

Figure 2.3 The representation of Smith Chart.

advanced over depending on the application. So guidewires in general should have sufficient axial rigidity along its shaft for advancing purposes and high torsional rigidity to provide a controlled torque response for proper manipulation. In addition, the distal part of the guidewire should possess lower flexural rigidity to move in the tortuous sections of the vessel anatomy without complications. Because a general purpose guidewire composes of several coaxial elements, each component should be chosen carefully to obtain desired mechanical properties. A standard multipurpose guidewire has a core wire with variable diameter proximal, intermediate and distal sections and a flexible tip coil on distal tip and metal hypotube that extends over intermediate and proximal sections and provides required flexural rigidity and high torsional rigidity without disturbing flexibility of distal tip section.

2.3 Methods

2.3.1 Antenna Design

The active guidewire was designed as 0.035-inch diameter and 1 meter long with two separate fixed receiver channels (Figure 2.4).

All prototypes were constructed in an ISO class 7 cleanroom using only medical-grade components. A tightly wound solenoid coil was used for the loop antenna design at the distal tip to provide guidewire tip visibility under MRI. The solenoid coil was formed by using 0.004 inch magnet wire. The final outer diameter of the solenoid coil was 0.026 inches. The optimum length of the solenoid was determined experimentally by measuring inductance of different length solenoids inductance until it dominates the transmission line inductance. The coil was attached to a 0.009-inch 50 ohm non-magnetic coaxial cable (Precision Interconnect Inc, Wilsonville, OR) placed over the entire length of the guidewire and used as a tranmission line.

A 0.010 inch diameter nitinol rod (Nitinol Devices and Components Inc., CA) was used for both the inner core of the guidewire and core conductor of the loopless

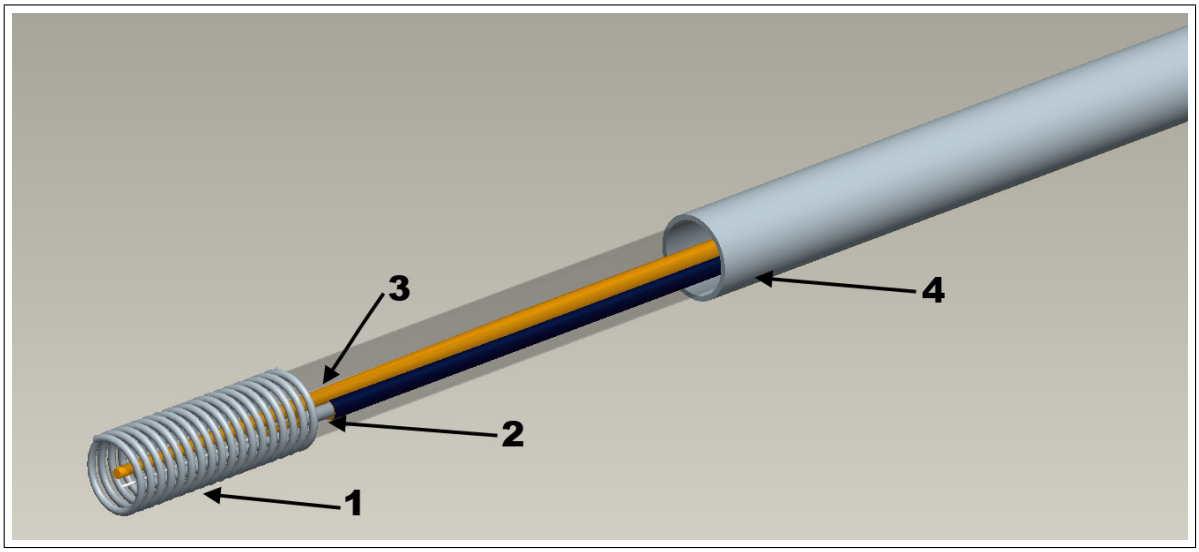

Figure 2.4 The schematic representation of the guidewire design: (1) solenoid coil, (2) micro coax cable, (3) nitinol rod, (4) nitinol hypotube.

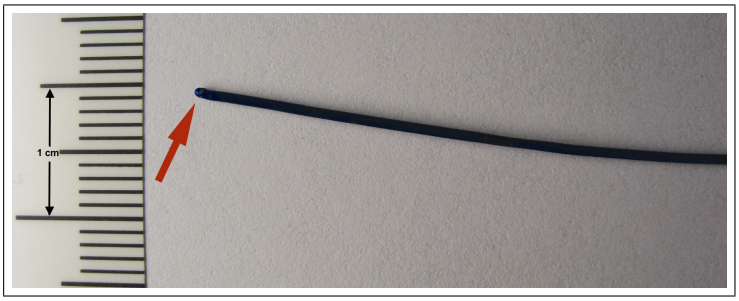

Figure 2.5 Photograph of the distal tip of the active guidewire. The arrow shows the dome-shaped round tip of the guidewire formed using custom-designed glass mold. Vertical stage shows millimeter increments.

antenna design. The distal 3 inches of the nitinol rod was grinded to create a lower profile to improve guidewire tip flexibility. The nitinol rod was coated with gold to improve its electrical conductivity thanks to the skin effect. The coaxial cable and nitinol rod were both covered with thermoplastic elastomer tubing (Pebax, Medical Extrusion Technologies Inc, CA) to improve guidewire stability and columnar strength. The distal 10 cm, including the distal coil, were coated with a lower durometer (less rigid) Pebax tubing to improve tip flexibility. The distal tip was sealed with a dome shape using a custom-designed glass mold to produce an atraumatic tip (Figure 2.5).

The polyimide tubing was jacketed over the pebax layer to increase the dielectric

properties of the insulation layer. The whole assembly is then inserted through a nitinol hypotube (Nitinol Devices and Components Inc, CA, US). A tightly wound, 10 cm long nickel-cobalt alloy (MP35N) coil was welded by Nd:YAG laser to distal end of the nitinol hypotube to create gradual stiffness transitions over the shaft. The loopless antenna channel was formed using the inner gold-coated nitinol corewire and outer nitinol hypotube to provide whole guidewire shaft visibility. To increase loopless antenna efficiency, the inner corewire-coaxial cable assembly was extended beyond the distal end of the nitinol hypotube by a quarter-wavelength (approximately 10 cm under loaded conditions in the body) [30]. The exact extension amount was determined by using network analyzer. Because SNR performance is optimum when the antenna input resistance is minimum [26]. The diameter ratio of the inner diameter of outer hypotube and diameter of inner corewire also was optimized to have a characteristic impedance that is close to the electrical load of the human body for the loopless antenna ($\sim$32 Ω) [44]. The whole shaft was coated with high durometer (stiff) plastic Pebax tubing for insulation.

2.3.2 Matching/Detuning Circuitry

The loop and loopless channels were tuned to 50 ohm at 63.86 Mhz (for proton MRI at 1.5 T) using separate matching/detuning circuitry at the proximal end of the guidewire with a network analyzer (HP 4195A, Agilent Technologies, Palto Alto, CA). The loop antenna channel of the guidewire was not matched at the solenoid coil and micro coaxial cable interface because of dimensional constraints (Figure 2.6).

A positive-intrinsic-negative (PIN) diode was used for both circuits to detune the guidewire receiving channels during scanner RF transmission, during which the diode is switched on by a DC voltage through the scanner connector port. A custom probe was designed by using 50 ohm coax cable and calibrated by using network analyzer. The each antenna channel was connected to its dedicated matching/detuning circuit box. Custom probe was welded to the both end of the solenoid coil and the junction point of loopless antenna design where the inner core extends out from the nitinol hypotube

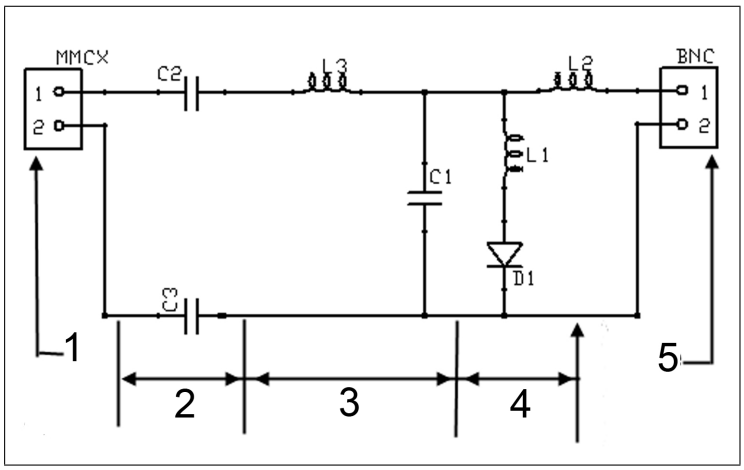

Figure 2.6 Schematic of the loop antenna matching/tuning and decoupling circuit 1) MMCX (micro BNC) connector 2) DC block section 3) matching/tuning section 4) decoupling section 5) BNC connector.

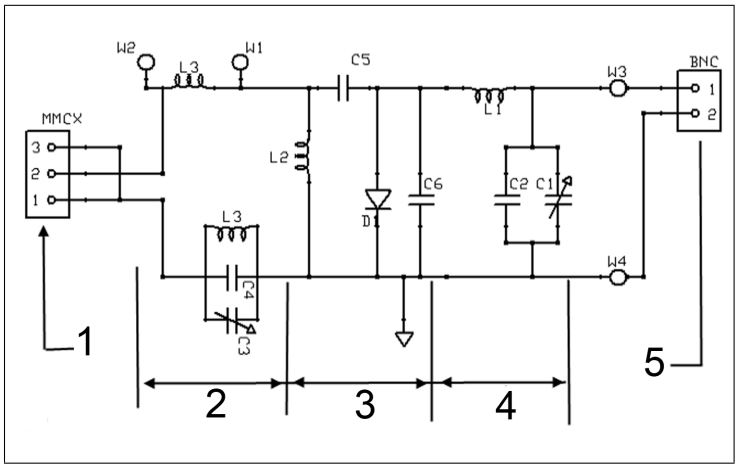

Figure 2.7 Schematic of the loopless antenna matching/tuning and decoupling circuit 1) MMCX connector 2) DC block section 3) matching/tuning section 4) decoupling section 5) BNC connector.

respectively. The appropriate values for the capacitor and inductor of detuning circuit that moves the measured characteristic impedance close to the open circuit point on the smith chart were determined for each antenna channel when the PIN diode is activated. Because a loopless antenna is unbalanced, the loopless antenna channel was connected to the balanced matching circuit via balun to block the unwanted generated current on the outer surface of the shield during RF transmission (Figure 2.7).

2.3.3 Mechanical Design

The guidewire was designed so that the loop channel would not compromise instrument size and handling compared with common X-ray devices. The 0.002 inch soft copper magnet wire was used to manufacture the 0.027 inch solenoid coil. To retain flexibility, materials were selected for the dipole antenna to compensate for the additional conductor and insulation required by the loop channel. The inner conducting rod was downsized to a 0.006 inch wire from a 0.010 inch wire and a 55 D durometer (less stiff) polymer insulated the wire from the transmission line of the neighboring loop channel. The distal 5 cm of nitinol hypotube was annealed by fluidized bath (Techne Inc., Burlington, NJ) to reduce the stiffness. Also 10 cm long nickel-cobalt alloy (MP35N) coil was welded by Nd:YAG laser to distal end of the nitinol hypotube to create gradual stiffness transitions over the shaft. A conformal coating, created by heating extruded Pebax (thermoplastic elastomer) tube over both channels, increased circuit stability for each antenna while providing the medium for good torque transmission. A custom connector enclosure was mounted over the junction where the both conductors of the loopless antenna channel were connected to the 0.012 inch microcoax cable. This polycarbonate enclosure not only prevents junction detachment accidentially but also it functions as a torquer when needed. Proximal end of the each channel connector was strengthened with heat shrink FEP tubing (Zeus Inc., Orangeburg, SC) and matching-detuning circuit for both channels were placed in RF shielded circuit enclosures (Figure 2.8).

Loaded Q measurements were obtained for each coil using a reflection-type measurement from S11 polar plots [45]. S_{11} measurements were performed by an Network analyzer with S parameter test set. Measurements were performed in a 0.35 % saline solution filled phantom.

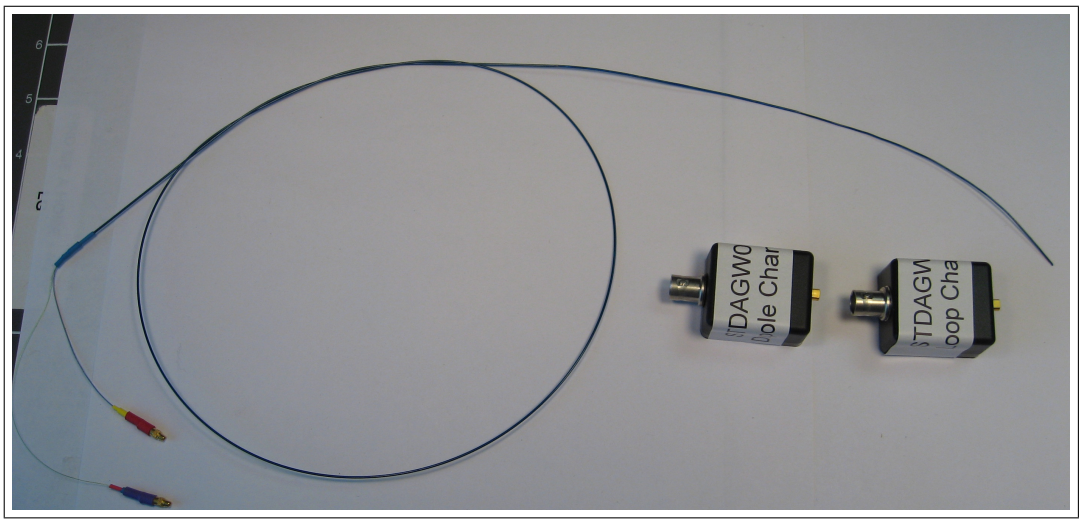

Figure 2.8 The two channel 0.035 inch active guidewire prototype (1 meter long) with dedicated tuning/decoupling circuit box for each channel.

2.3.4 Visibility Performance Testing under MRI

All imaging was performed on a 1.5T Siemens Espree MR scanner (Siemens Medical Solutions USA, Inc., Malvern, PA). The guidewire was attached to the scanner coil port using a custom-designed 4-channel pre-amplifier interface adaptor (Stark Contrast MRI Coils Research, Erlangen, Germany). The active guidewire was used only as a receiving antenna.

2.3.4.1 Two-channel Visibility In Vitro. A silicon aortic arch model (Shelley Medical Imaging Technologies, Ontario, Canada) was used to evaluate the visibility of two separate channels during guidewire advancement under MRI. The aortic arch model was filled with saline solution (0.35 % NaCl) solution to get similar loading conditions ($\epsilon_r = 77$,$\sigma = 0.6$ S/m) of an active guidewire inserted into a human body (Figure 2.9). Real time MR imaging was performed using a Steady State Free Precession (SSFP) sequence with Slice thickness 6 mm, 3.72/1.86 msec TR/TE, matrix = 192 X 108 and bandwidth = 797 Hz/px. The loop channel of guidewire was colored red and loopless channel colored green using a customized interactive rtMRI interface [13, 32].

Figure 2.9 The silicon aortic arch model filled with saline solution. The guidewire was placed inside the model for in vitro visibility test under MRI.

2.3.4.2 Tip Position Accuracy In Vitro. The loop channel functional performance was tested in terms of position accuracy of the guidewire tip and determination of guidewire tip orientation during in vitro tests. A custom polyacrylic platform was prepared to compare the actual tip location and received signal position. The platform was machined to hold the guidewire straight and level during phantom scans. Side horizontal grooves were also machined at 0.5 inch intervals between the centers of each marker. When the phantom is filled with 0.35 % NaCl solution, solution fills the grooves and they appear bright in relation to the block itself. This serves as a convenient reference for distance in the reconstructed image. The acrylic block was positioned level on the bottom of a polyethylene container and distal tip of the guidewire was placed level with the 1.5-inch mark (3rd groove down from top) (Figure 2.10). The guidewire was fixed inside its channel. A 2-D turbo spin echo sequence with the following parameters: TE = 556 ms, TR = 16 ms, Slice Thickness = 2 mm, matrix 156 X 192, Bandwidth = 130 Hz/px. The difference between the physical tip and the maximum signal intensity pixel was calculated using Matlab (MathWorks Inc, Natick, MA).

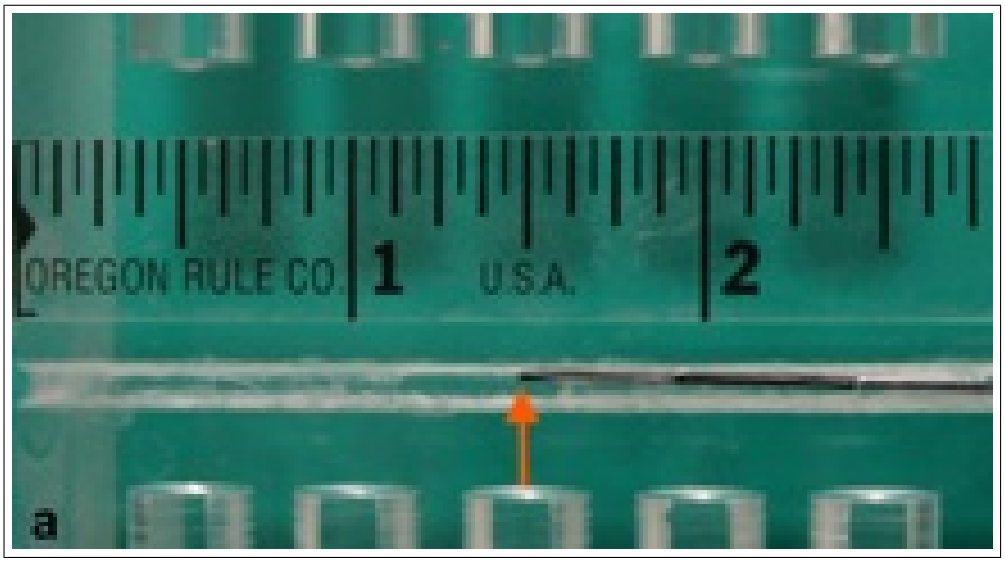

Figure 2.10 The acrylic block with a central groove running lengthwise to hold the guidewire in-plane during MR scan. Active guidewire was placed level with the 3rd groove down from the top of the acrylic platform to perform tip accuracy measurement. The arrow locates the guidewire tip position.

2.3.4.3 In vivo Evaluation. In vivo experiments were conducted on fully anesthetized pigs in protocols approved by the National Heart, Lung and Blood Institute Animal Care and Use Committee. A balanced SSFP sequence was used with the following parameters: TR = 3.72 ms, TE = 1.86 ms, flip angle = 60^0 , slice thickness = 6.0 mm, field of view (FOV) = 340 mm, matrix = 192 X 128, bandwidth = 797 Hz/pixel. The images were reconstructed with device channels colored independently using the same custom rtMRI interface described above. From a transfemoral approach, the active guidewire was advanced retrograde along the aorta under rtMRI guidance.

2.3.5 Mechanical Performance Testing

Representative 0.035-inch commercial guidewires were selected for comparative mechanical testing. The InqWire (Merit Medical, Salt Lake City, UT) is an inexpensive commodity J-tipped guidewire for routine introduction of catheters into relatively normal peripheral arteries. The Radiofocus Glidewire (Terumo Medical, Somerset, NJ) is a hydrophilic-coated nitinol guidewire that is highly torquable but soft-shafted and used to navigate tortuous or diseased peripheral arteries. The Wholey Hi Torque J-tip

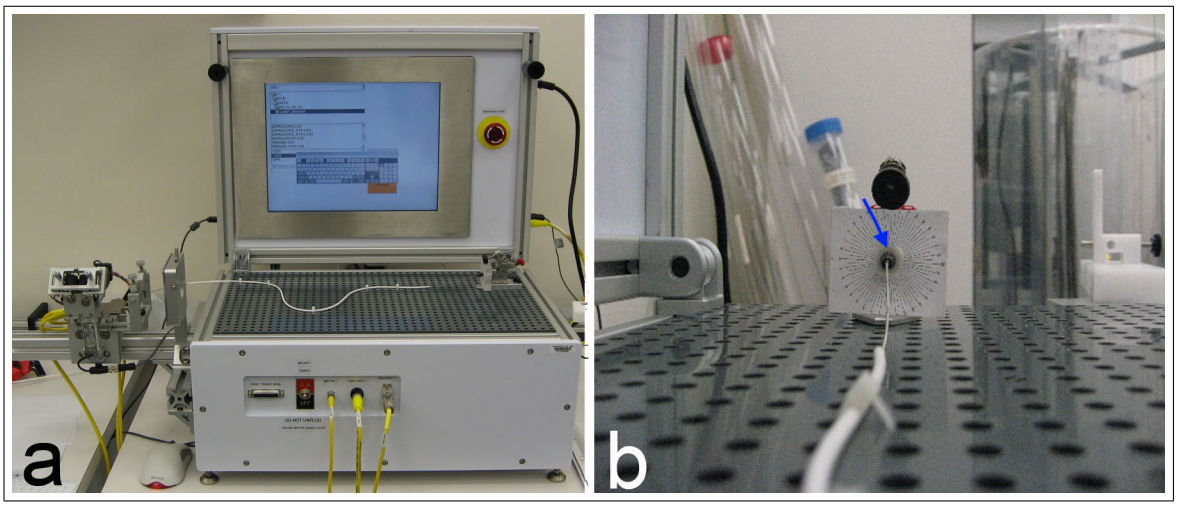

Figure 2.11 (a) Torquabillity test fixture setup. Each guidewire sample was advanced into tortuous fixed curvature tube that represents relevant vasculature to measure required torque value to rotate the guidewire tip 90 degree. (b) Distal tip of the guidewire was fixed into collet that is free to rotate around its axis. Degree of rotation can be measured relative rotation of the marker to the angular scale. The arrow shows the marker on the collet.

(Mallinckrodt Medical, St. Louis, MO) is highly torquable and soft-shafted steel alternative. The Hi-Torque 35 Supracore (Guidant, Santa Clara, CA) is a highly torquable soft-tip but rigid-shaft guidewire for navigating peripheral arteries and introducing bulky or rigid devices into them. The final two-channel active guidewire design was compared mechanically as recommended by guidance by the US Food and Drug Administration [26].

2.3.5.1 Torqueability Test. A simulated tortuous vessel anatomy was designed using silicon tubes over the Machine Solution IDTE testing device platform (Machine Solutions, AZ US) (Figure 2.11a). The distal tip of the guidewire was attached to a fixed collet that is free to rotate axially. The distal tip of the collet was marked and rotation angle was measured relative to a fixed platform (Figure2.11b). The guidewire proximal end was mounted to a digital torque meter (IMADA Inc., HTG-2, Northbrook, IL, US) and then peak torque values required to rotate the distal tip in increments of 90 degrees and number of turns were recorded. Although each brand guidewire comes in different lengths, same testing was performed over all sample wires by attaching the torquemeter from 90 cm away from the distal tip.

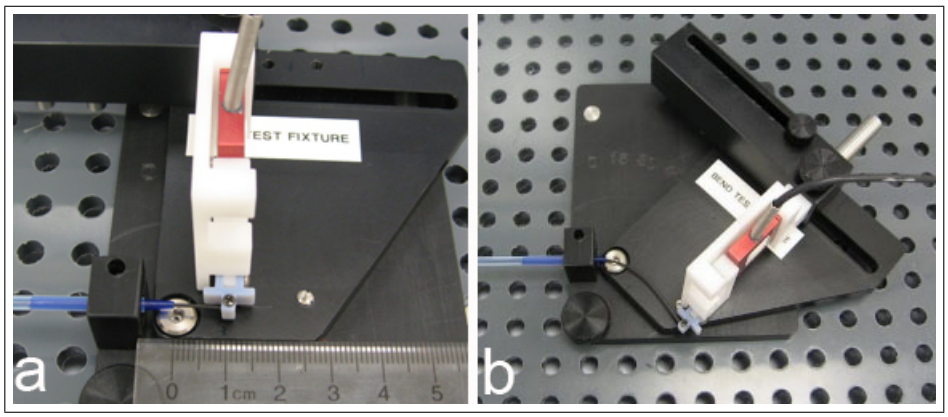

Figure 2.12 (a) The distal tip flexibility test fixture. The guidewire tip is fixed into load cell tip probe. The sample guidewire was also fixed 1 cm away from the distal tip. Then guidewire was bent at 15 degree increments. (b) Distal tip flexibility test setup with the wire fixed 3 cm away from the distal tip and deflected 45 degrees.

2.3.5.2 Tip Flexibility Test. The aim is to demonstrate the force required to deflect the distal tip of the guidewire 15, 30, 45 and 60 degrees when the wire is fixed at 1, 3, 5 and 10 cm away from the distal tip. The polycarbonate platform was formed with a rotating part around the fixed pin. The rotation angle can be determined using angle marks on the platform base. A 100 gram-force load cell was fixed onto the rotating part. The test guidewire was placed onto the polycarbonate platform and the distal tip point was contacted with the load cell tip and the guidewire was fixed at 1, 3, 5 and 10 cm away from distal tip using a rigid tube respectively (Figure 2.12a). The rotating part was rotated until it made angles of 15, 30, 45 and 60 degrees with the platform base and the load cell values recorded for each specific angle (Figure 2.12b).

2.3.5.3 Pushability Test. Each guidewire was tested in two different vessel geometries: (1) from femoral access to the subclavian vein (longer trajectory that ends with significant curvature) and (2) from left femoral vein to right femoral vein (short trajectory with sharp curvature). Each trajectory was formed by placing flexible Pebax tubing (outer diameter 4 mm, inner diameter 3 mm) into a Venous Anatomical training model (Lake Forest Anatomicals Inc, Lake Forest, IL,US) (Figure 2.13). Each guidewire was automatically advanced into the vasculature setup by a servo motor. Resistance force to the passage of the guidewire during its insertion was recorded by a load cell placed under the rollers that advance the wire.

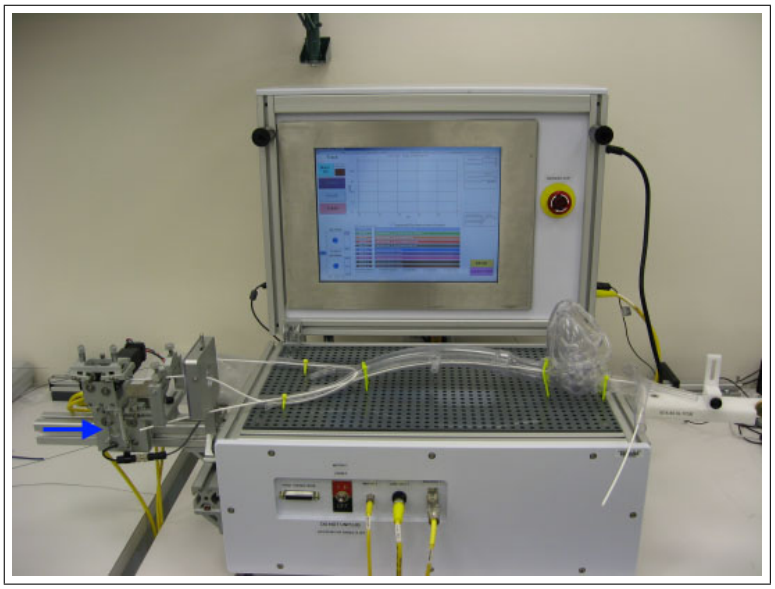

Figure 2.13 Pushability test setup. Arrow shows the position of the load cell that measures the resistance force during automatic guidewire insertion through servo motors.

2.4 Results

2.4.1 Antenna Measurements

The optimum solenoid length was determined that dominates the inductance of the transmission line as 25 mm long. Both receiver channels were tuned to 50 ohm at Larmour frequency (Figure 2.14 and 2.15).

The quality factor, Q, of the guidewire antenna channels loaded in 0.035 % NaCl solution after tuning and matching process were determined to be 70 for the loop channel and 52 for the loopless channel.

2.4.2 In Vitro Visualization

During guidewire advancement inside the aortic arch model in vitro tests, the loop channel showed good axial signal homogeneity over two ends of the solenoid coil. The longitudinal signal distribution was homogenous over almost the entire length of

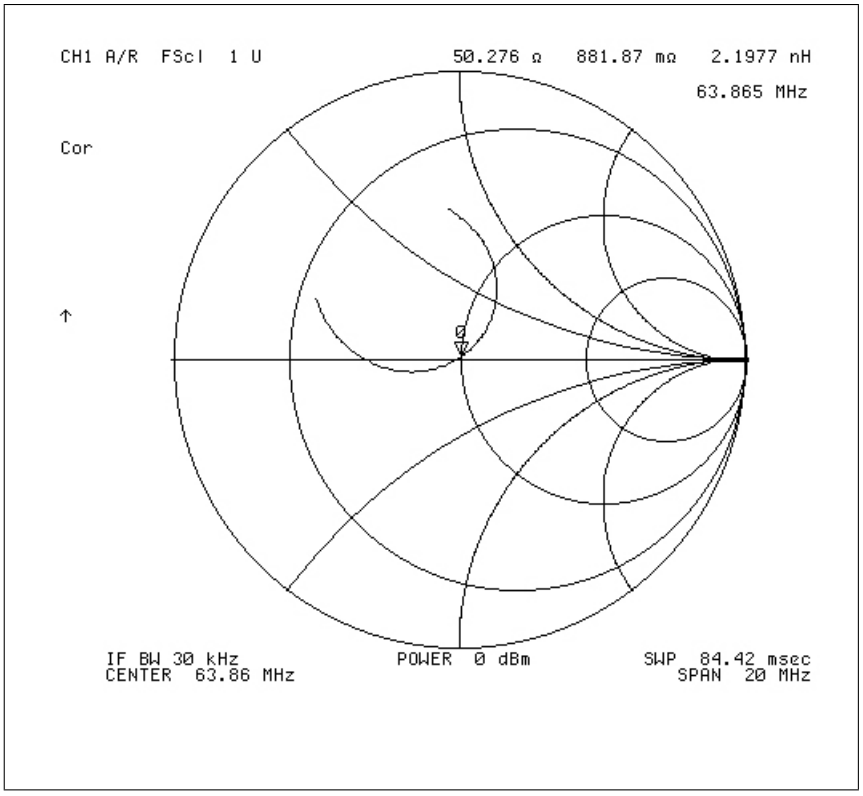

Figure 2.14 Smith chart representation after the loop channel was tuned to 50 ohm at Larmour frequency.

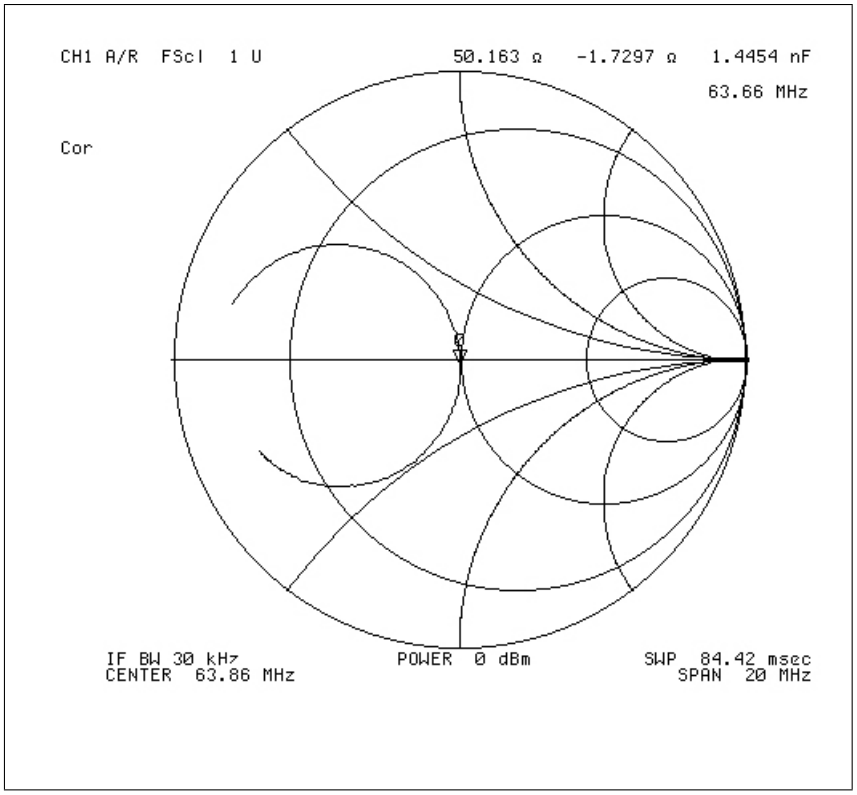

Figure 2.15 Smith chart representation after the loopless channel was tuned to 50 ohm at Larmour frequency.

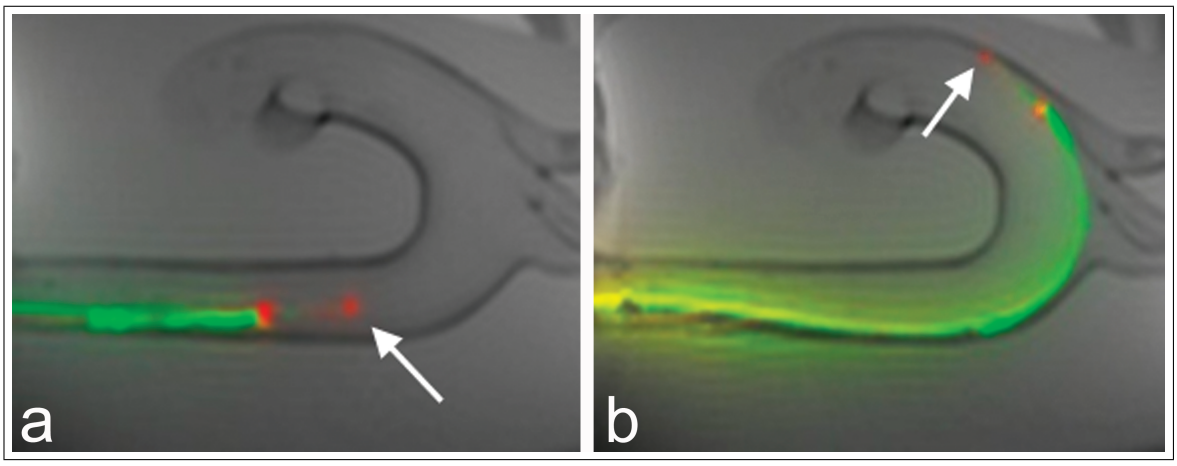

Figure 2.16 Phantom MR image acquired with two channel guidewire. (a) Tip (red color) and distal shaft (green color) of the guidewire could be seen easily during advancement. (b) The guidewire manipulated to advanced over the aortic arch. It was observed that there was no disruption on both received signals due to bending the distal shaft. The arrow shows the guidewire tip in both pictures.

the loopless antenna channel (Figure 2.16).

The distance between the center line and maximum signal intensity pixel was measured between the guidewire actual position on the acrylic platform and the distal tip coil maximum signal location apparent in each MR image. The average distance value between center line and maximum signal intensity pixel was 0.97 mm $\pm$ 0.42 mm (Figure 2.17).

2.4.3 In Vivo Visualization

The two-channel active guidewire was visualized well along the entire shaft during the in vivo experiments. The loop antenna signal at the distal tip facilitated the navigation in terms of tip visualization and tip orientation. Catheter tip position and shaft could easily be seen relative to background anatomy during advancement. The proximal bright signal received through loop channel is helpful to determine distal tip deflection. Figure 2.18 shows the guidewire in the aorta of an animal.

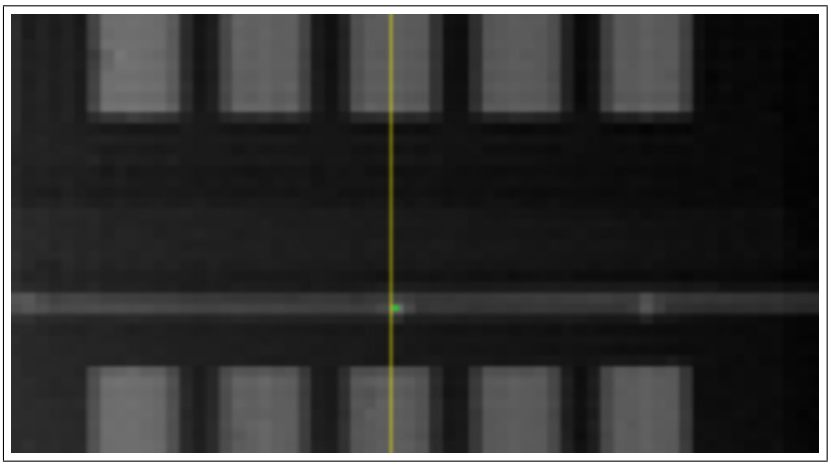

Figure 2.17 The MRI of active guidewire was placed level with the 3rd groove down from the top of the acrylic platform to measure imaging accuracy of tip position. The center line of the groove (yellow color) and maximum signal intensity pixel (green color) are marked.

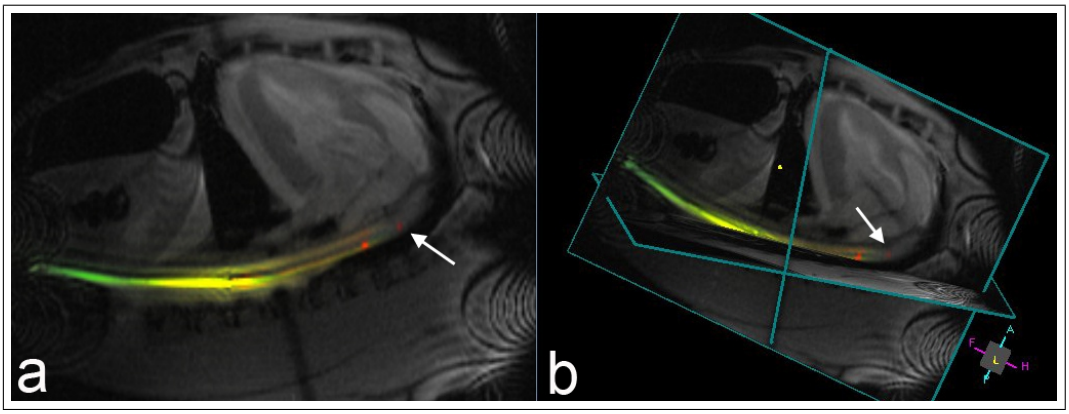

Figure 2.18 (a)The guidewire was inserted through femoral access up to the aortic arch. (b) Both guidewire tip (arrow, red) and shaft (green) were reconstructed in different colors during 3-D real time MRI.

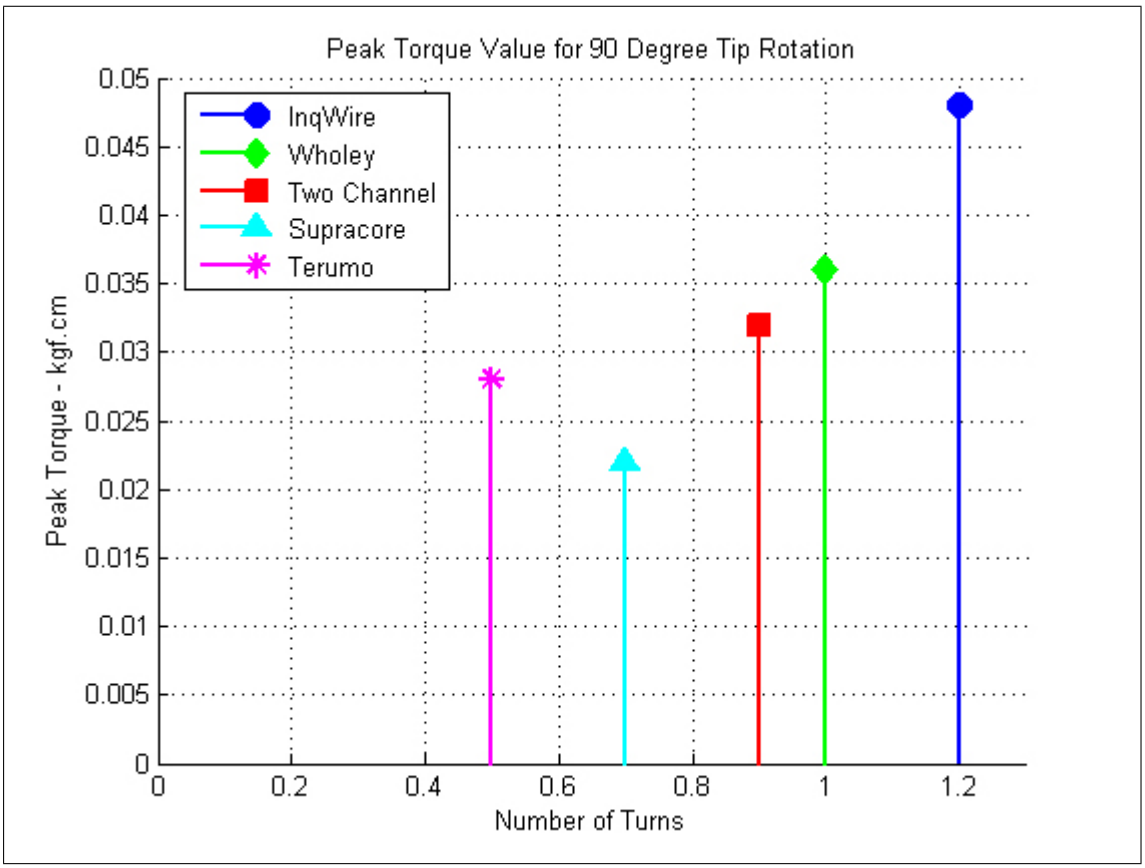

Figure 2.19 Comparative torquability of the active guidewire and commercial X-ray alternatives. Higher peak torque values and number of turns indicate less torquability.

2.4.4 Torquability Test

The active prototype guidewire showed much less resistance than Wholey and Inqwire to rotate the distal tip during the torque test. However, it is not as torqueable as the Glidewire or Supracore wires (Figure 2.19).

2.4.5 Flexibility Test

Because the prototype guidewire is designed to recanalize chronic total occlusion, the first 3 cm of the distal end is stiffer than comparator wires especially in higher bending angles. However, measured with the fixation point more proximally along the shaft, the prototype guidewire shaft was more flexible than the others, especially at higher bending angles (Figure 2.20).

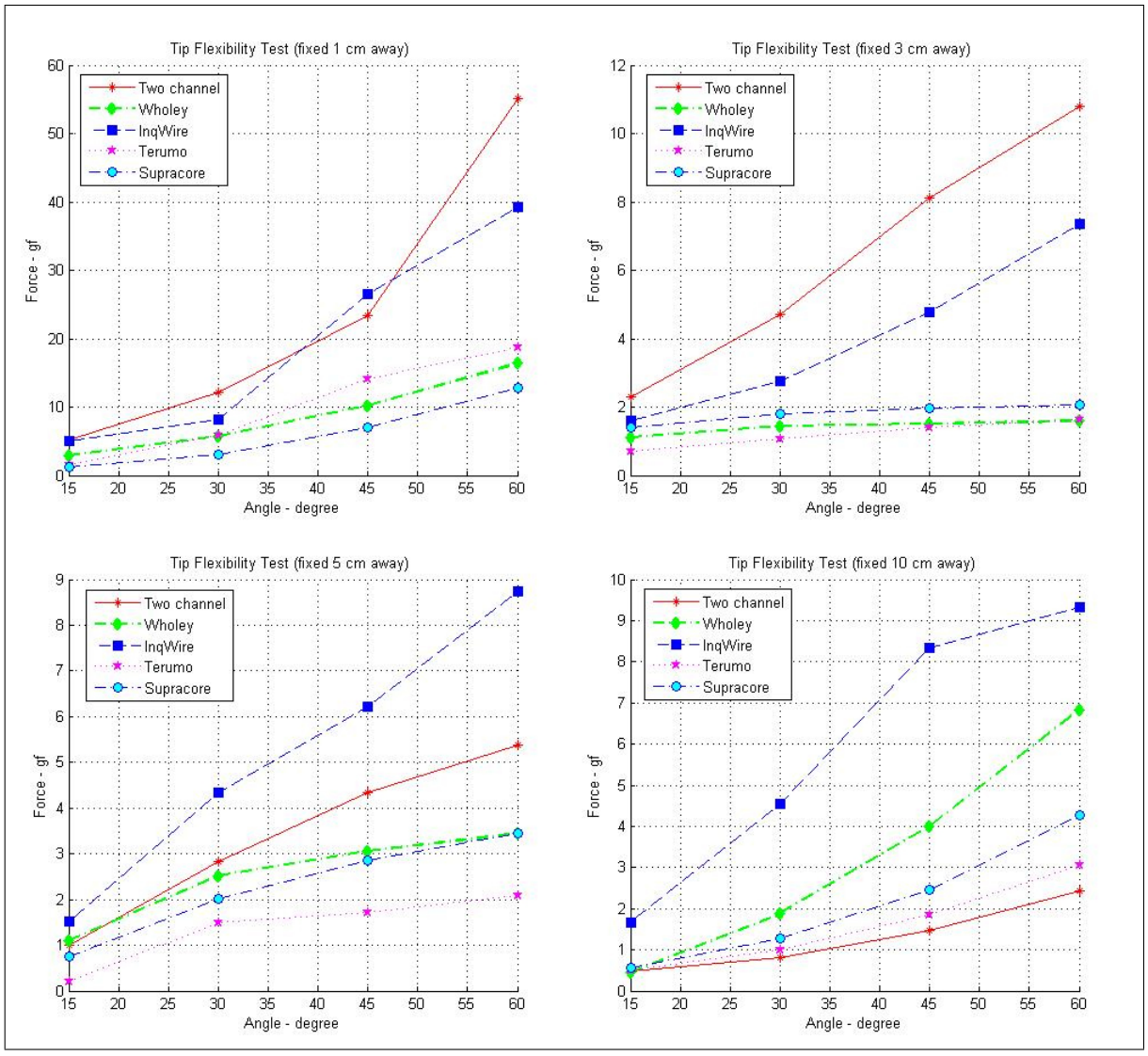

Figure 2.20 The graphs show the measured resistance force at the guidewire distal tip while bending from a) 1 cm away b) 3 cm c) 5 cm d) 10 cm away from the distal tip. The guidewire was attached to load cell at the very distal tip as shown in Figure 2.12.

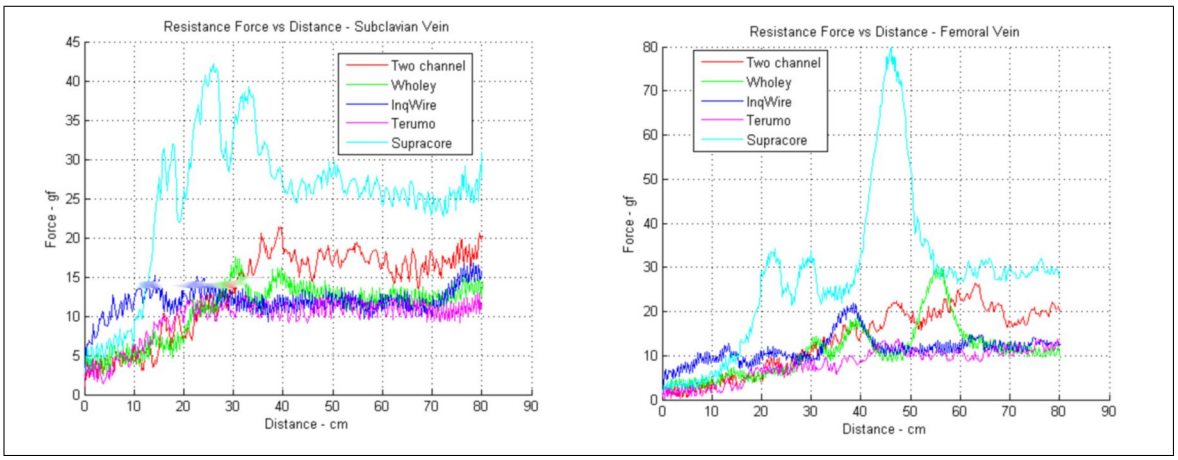

Figure 2.21 The graphs show the measured resistance force during servo-motorized guidewire advancement inside the vessel phantoms.

2.4.6 Pushability Test

It was observed that the prototype guidewire has shaft stiffness similar to most of the wires that were compared. The resistance force values were comparable for the first 30 cm for all wires except much stiffer Supracore. The proximal shaft stiffness of the active guidewire prototype, however, is slightly greater than the most of the wires tested but still remains well below that of Supracore. Peaks in the force-distance curves indicate junctions where cores of different rigidity "jump" along the phantom or vessel (Figure 2.21).

2.5 Discussion

Simultaneous visualization of the distal tip and shaft in a 0.035 inch active guidewire that employs two independent RF channels has been demonstrated. When high signal amplification along the entire length is desired, traditional active visualization techniques often involve equipping a guidewire with a dipole antenna [26, 30]. A relevant drawback of this method is in the lack of signal profile near the distal tip, which creates uncertainty about tip position during procedures. The proposed guidewire design incorporates an additional channel, a loop antenna, to provide a robust tip signal.

Unambiguous tip visibility reduces the risk of injuring, disrupting or perforating a vessel during guidewire advancement through a tortuous vessel and eases instrument handling during interventions. Although several experimental designs have been proposed in the past, we develop for the first time a clinical grade two channel active MR compatible guidewire with adequate mechanical properties and visibility during imaging.

Guidewires are operated remotely to establish a path through chamber and tissue spaces and then are used to position additional catheters that deliver information, energy, materials, or implants. Guidewire mechanical design parameters vary according to the specific medical application. Length and diameter are driven by anatomic distances and bulk of devices to be delivered. The tip and shaft usually have differential flexibility requirements. Soft tips are less likely to injure tissue but may be less able to enter, cross, and navigate lesion or tissue targets because of reduced torquability or pushability. Soft shafts may be able to navigate curves but are less able to deliver bulky catheters. Transitions or junctions between tips and shafts, if too abrupt, lead to guidewire prolapse during navigation. The primary guidewire mechanical design elements are an inner core and outer cover. Cores may taper according to requirements for force transmission, torque responsiveness, flexibility, and ability to track around complex trajectories without prolapse. Core tips may be shapable to meet geometric requirements of the target. Distal coils and polymer covers impart passive conspicuity, maintain a constant diameter and balance tactile feedback against traversability, and can be exploited as MRI antennas. Covers and coatings balance trackability with tactile feedback and can impart further stiffness and torquability. Guidewire handling properties include torquability, flexibility and pushability. Torquability relates rotation of the proximal end of the guidewire to rotation of the distal end. Our active guidewire prototype had intermediate torquability comparable to a commercial Wholey interventional guidewire (Figure 2.19). The tip flexibility test evaluates the resistance force of the guidewire tip when it bends during guidewire advancement. The higher the resistance force means stiffer the guidewire tip. Our two channel active guidewire prototype is designed to be more rigid in its distal 1 inch, having a tightly wound solenoid coil with Pebax insulation. More proximally, shaft rigidity imposed only by the inner core

and microcoaxial transmission line was comparable to other commercial devices (Figure 2.21). Pushability is the ability to deliver distal tip force despite complex geometry imposed by anatomy and pathology, encompasses differential stiffness and lubricity, and is difficult to model. Friction forces increase with insertion distance; pushability force can vary abruptly as core junctions are advanced, as seen in (Figure 2.21). Other design considerations include tensile (failure) strength, torque (failure) strength, and biocompatibility, which are not tested here.

Most of the active instrument visualization designs based on device profiling in MRI employ conductive transmission lines to bring the received RF signal to the MR scanner. External tuning, matching and decoupling circuitry within an RF-shielded box is used, connecting the active instrument and a preamplifier box [26, 28, 46, 47]. In the presence of long conductors greater than approximately 60 cm (an eighth wavelength in air) for 1.5 T MRI systems, there is an increased risk of tissue heating due to amplification of the electric field around the wire [48]. Detuning elements like PIN diodes are integrated into the tuning and matching circuitry for each channel of our guidewire to reduce this heating risk. These are activated during RF transmission and reduce the tissue specific absorption rate (SAR) around the guidewire's length. Preliminary RF safety tests were presented in Chapter 5. Further heating tests are needed and in progress to confirm clinical suitability of this particular circuitry.

2.6 Summary

In conclusion, a new two channel 0.035-inch clinical-grade active guidewire was developed for interventional cardiovascular MRI procedures. Because it includes two independent antenna - one loop antenna for the tip and one loopless antenna for the shaft -this guidewire provides superior tip visibility compared with other previously reported active designs. Each channel can also be color-coded and displayed separately in the real-time MRI display. Device conspicuity and precision of MRI guidewire tip location were confirmed both in vitro and in vivo in pigs. Mechanically, the properties of new guidewire were comparable to commonly used X-ray interventional guidewires.

Despite more complex construction, the distal tip stiffness is increased only slightly as required by our first target application, recanalization of chronically occluded peripheral arteries.

3. Signal to Noise Ratio Optimization

3.1 Introduction

MRI images are reconstructed from data that are intrinsically two or three dimensional arrays of complex numbers. In other words, MRI images can be presented as a pair of images representing the real and imaginary components. It is more appropriate to combine these images onto a single image as the magnitude of the complex array for clinical interpretation. These amplitude images are being used in practice because they are not susceptible to artifacts generated from phase shifts such as those from field inhomogeneities, chemical shifts, or RF penetration artifacts [49]. There are two main approaches: combining all of the image information into the real component image or taking the magnitude of the each complex image. The first approach requires a simple rotation of the phase of the quadrature detector. However, eddy currents induced by gradient coils or phase shifts of the radio-frequency wave as it penetrates through the body arises phase aberrations. This requires sophisticated correction methods to convert the information across the whole image into the real component. Second approach is to take the magnitude of each complex number. Because the second approach avoids the problems of phase artifacts by discarding the phase information, it is more attractive [50].

The signal-to-noise ratio (SNR) is an important index of image quality in magnitude MR images . A common method for measuring SNR values compares the mean signal to the standard deviation of noise. Although it is possible to measure the signal as the ensemble average of the pixel intensities over a region of interest (ROI), the noise cannot be measured directly from the same region because possible signal variation in that ROI may bias the noise estimate. There are several different methods to calculate the SNR for MR images with the primary distinction being the methods and acquisitions used to determine noise. In order to evaluate the signal performance of active interventional instrument channels, it was aimed to develop a protocol that per-

forms SNR map of the active device. To perform this analysis, two appropriate SNR techniques - Signal Magnitude Image Method and Double Acquisition Method-that can be implemented with the standard imaging rather than having to employ special acquisitions or noise only scans. The analysis result will help to predict device profiling functionality in catheter-based and percutaneous procedures conducted under MRI guidance. Device signal profiles will be better visualized and quantified pixel by pixel after device construction to decide which coil designs could provide better visualization performance, thereby improving signal intensity seen under MRI.

3.1.1 Signal Magnitude Image Method

A simple way to determine SNR from a single magnitude image is to take the average of the signal intensity from a uniform region of interest (ROI) containing the object of interest and divide it by the standard deviation (SD) of the noise from an area containing no signal (noise only). The area of no signal should be in "air" only, taken from an area in field of view (FOV) that does not contain the phantom or other signal source. The accuracy of the SD is also dependent on the number of receiving coils. A magnitude image is typically the form that one sees with standard anatomic MR images. While actual image information from the Fourier transform is in a complex data set containing real and imaginary components, the magnitude image discards phase information and simply represents the data as the magnitude, pixel by pixel, of the complex data set. This approach can avoid artifacts due to phase shifts but it can also impact the signal measurements between the real image and the magnitude representation. The white noise impacting the real and imaginary images of the acquired complex data has a Gaussian distribution (equation 3.1) centered around zero:

$$\varphi_{\mu,\sigma^2}(x) = \frac{1}{\sigma\sqrt{2}\pi} exp(-\frac{(x-\mu)^2}{2\sigma^2}) \tag{3.1}$$

However, calculation of the magnitude value from this real image is a non-linear operator and the rectified noise in the magnitude image is no longer centered around

zero. The signal now has a Rician distribution (equation 3.2) which at higher SNR values, approximates the Gaussian distribution:

$$f(x|v,\sigma) = \frac{x}{\sigma^2} exp(-\frac{x^2+v^2}{2\sigma^2}) I_0(\frac{xv}{\sigma^2}) \tag{3.2}$$

When signal approaches zero, in noise-only regions, it approaches the Rayleigh distribution.

$$f(x;\sigma) = \frac{x}{\sigma^2} exp(-\frac{x^2+v^2}{2\sigma^2}) \tag{3.3}$$

The measurement of the standard deviation of the background noise in magnitude images can be artificially decreased leading to an overestimation of the true SNR [49, 51, 52, 53, 54, 55]. Therefore, if the standard deviation or mean of the Rayleigh distributed noise is calculated, a correction factor must be used to determine the true standard deviation of the Gaussian distribution. The correction factors for 1-channel receiver systems were calculated by both Henkelman and Edelstein, et al [49], [53]. This correction was then extended to multiple receiver channels, such as those in phased array, by Constantinides, et al [52]. The calculated correction factors for channels up to 32 in an area of no signal are shown in Table 3.1.

3.1.2 Double Acquisition Magnitude Image Method

The single magnitude image technique requires manual selection of noise ROI which can be tainted with remnant signal and the number of points involved in the noise calculation is limited, increasing the error in the standard deviation calculation. An alternate method using two sequentially acquired magnitude images allows the entire image to be used to calculate the noise, thus possibly reducing the error in the noise calculation as compared to the limited ROI in the single magnitude image [56]. This technique, however, does require multiple acquisitions and assumes no changes

Table 3.1
Correction Factors for Multiple Receiver Channels (1-32) in Image ROI with Noise Only [52].

Number of Coils	Correction Factor	Number of Coils	Correction Factor
1	0.6551	17	0.7045
2	0.6824	18	0.7046
3	0.6911	19	0.7047
4	0.6953	20	0.7049
5	0.6978	21	0.705
6	0.6994	22	0.7051
7	0.7005	23	0.7052
8	0.7014	24	0.7052
9	0.702	25	0.7053
10	0.7026	26	0.7054
11	0.703	27	0.7055
12	0.7033	28	0.7055
13	0.7036	29	0.7056
14	0.7039	30	0.7056
15	0.7041	19	0.7057
16	0.7043	20	0.7057

between images due to object movement or other factors. Subtracting the two images pixel-by-pixel eliminates the consistent signal, resulting in a noise-only image given the assumptions previously stated. This standard deviation of this noise image can then be calculated and used to determine the image SNR. Since the calculated standard deviation used an image generated from a difference operation, the calculated noise deviation must be corrected by $\sqrt{2}$:

$$Image_{noise} = \frac{SD_{noise}}{\sqrt{2}} \tag{3.4}$$

where Image_{noise} is corrected noise deviation of acquired image, SD_{noise} is standard deviation of the substracted image noise.

3.2 Methods

The two channel guidewire was placed on a custom design platform to make sure that the device position is fixed relative to the phantom during the scan. The phantom was filled with 0.35 % NaCl solution to mimic the body loading conditions. A SSFP sequence was used for both methods during MRI scans with following parameters: TR = 836.8 ms, TE = 1.8 ms , flip angle = 57 ^{0} , slice thickness = 5.0 mm, matrix = 256 X 128, bandwidth = 700 Hz/pixel. Each guidewire channel was scanned seperately. A graphical user interface (GUI) imaging module was created to perform signal to noise ratio (SNR) maps with Matlab (Mathworks, Natwick, MA) for both methods. SNR calculations were performed in line with the NEMA standard [51]. It was aimed to cater signal evaluation of active two channel guidewire prototypes.

3.2.1 Single Magnitude Image Method

SNR was computed according to a single magnitude image for each channel separetely. A region of interest (ROI) representing noise was selected from four corners of the image. It provided a considerable distance from the device and phantom to make sure that noise calculations are unaffected by signal artifacts (Figure 3.1). Subsequently, the standard deviation (SD) of the noise magnitudes in the ROI was calculated. Since error of noise estimates (E_n) is inversely proportional to the square root of sample number (Eq. 3.5), a minimum of 1000 points were included in the each noise ROI to attain consistency in SNR measurements.

$$E_n = \frac{1}{\sqrt{N}} \tag{3.5}$$

where N is number of points.

During image acquisition, all surface and body coils were deactivated such that

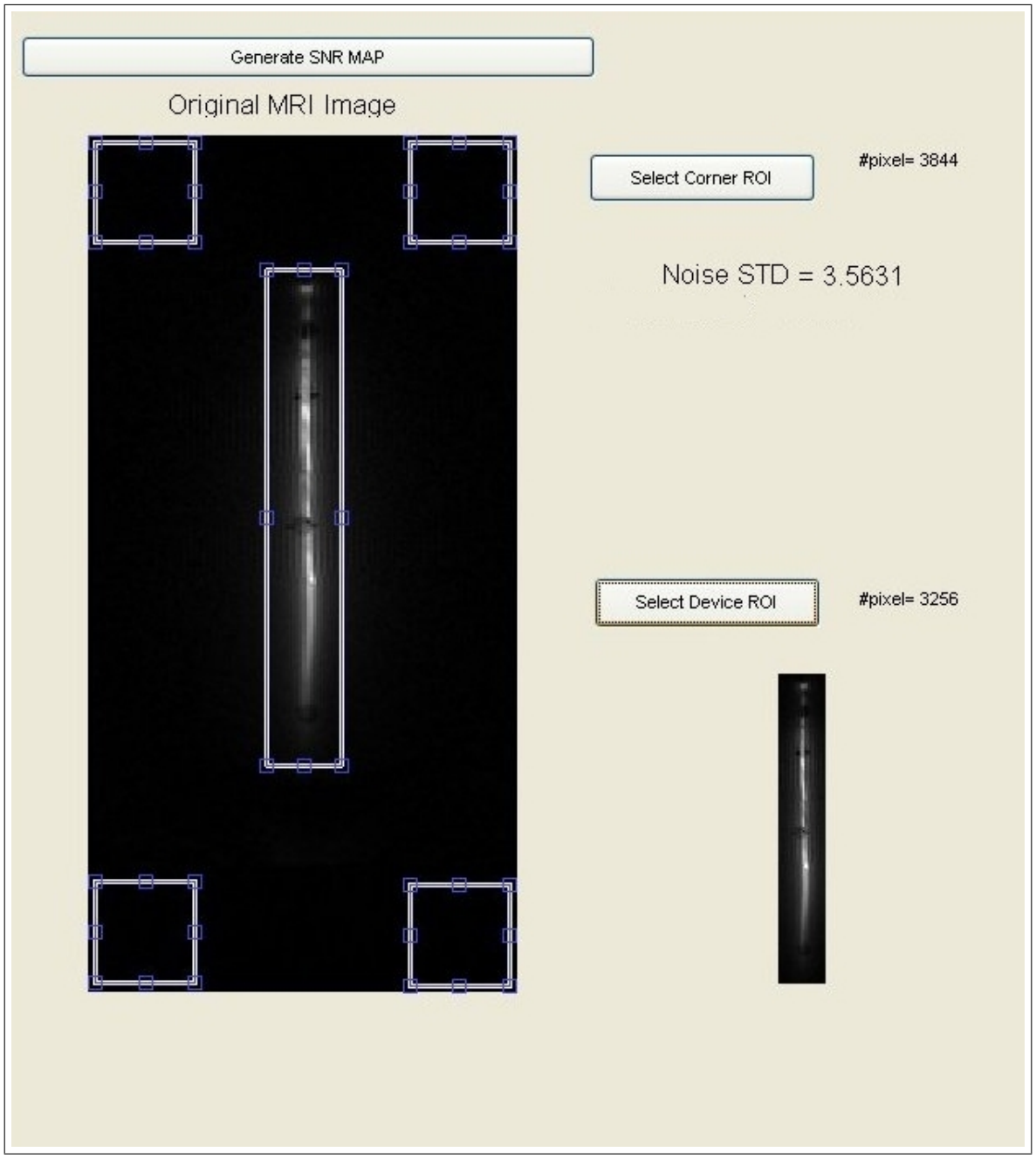

Figure 3.1 The Matlab GUI window that shows the selected region of interest (ROI) for active guidewire device signal and the selected ROI from four corners for noise signals.

phantom signals were eliminated, leaving only device signals to maximize the area for noise ROI selection. Once noise standard deviation was computed, the value was corrected based on the number of device channel and then the following definition is used to generate the device SNR map on a pixel by pixel basis:

$$SNR = \frac{Signal}{Noise} \tag{3.6}$$

3.2.2 Double Acquisition Magnitude Image Method

This method was based on the subtraction algorithm of two scans of the same device and same system configuration (Image 1 and Image 2). The image matrices of these two scans were subtracted from each other to produce a pixel by pixel difference image (Image 3) (Figure 3.2) that should theoretically embody just the noise data :

$$[Image3] = [Image1] - [Image2] \tag{3.7}$$

Two phantom scans were performed on the same slice selection as well as back to back without any system configuration adjustment in between scans. Once the difference noise matrix was attained, the same calculation procedure was used in single magnitude image method was applied. The noise standard deviation was corrected by division of $\sqrt{2}$.

3.3 Results

3.3.1 Single Magnitude Image Method

The max SNR values for loopless and loop guidewire antenna channel were calculated by using Matlab program (Table 3.2) as 422.16 and 236.28 respectively. Figure 3.3 and Figure 3.4 shows the acquired MRI image and SNR map of the loop and loopless channel of the active guidewire respectively.

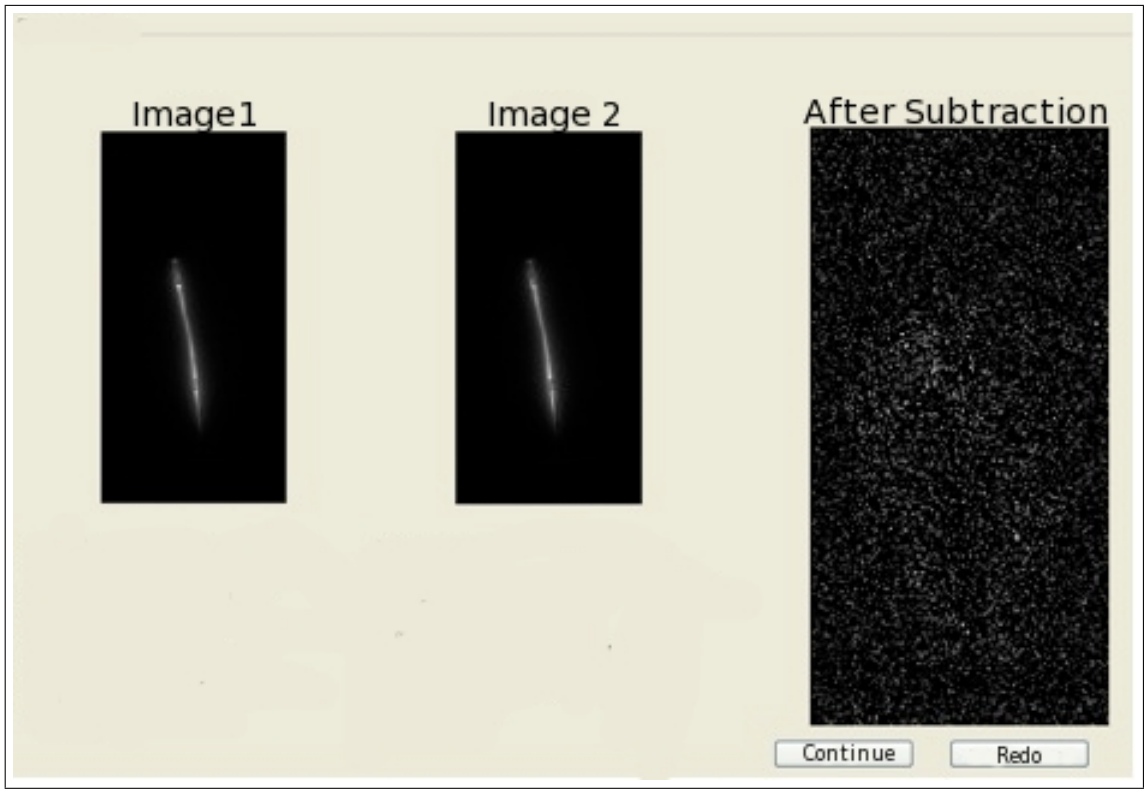

Figure 3.2 Image selections of the two channel active guide wire scans for the subtraction method (left) and noise subtraction image (right).

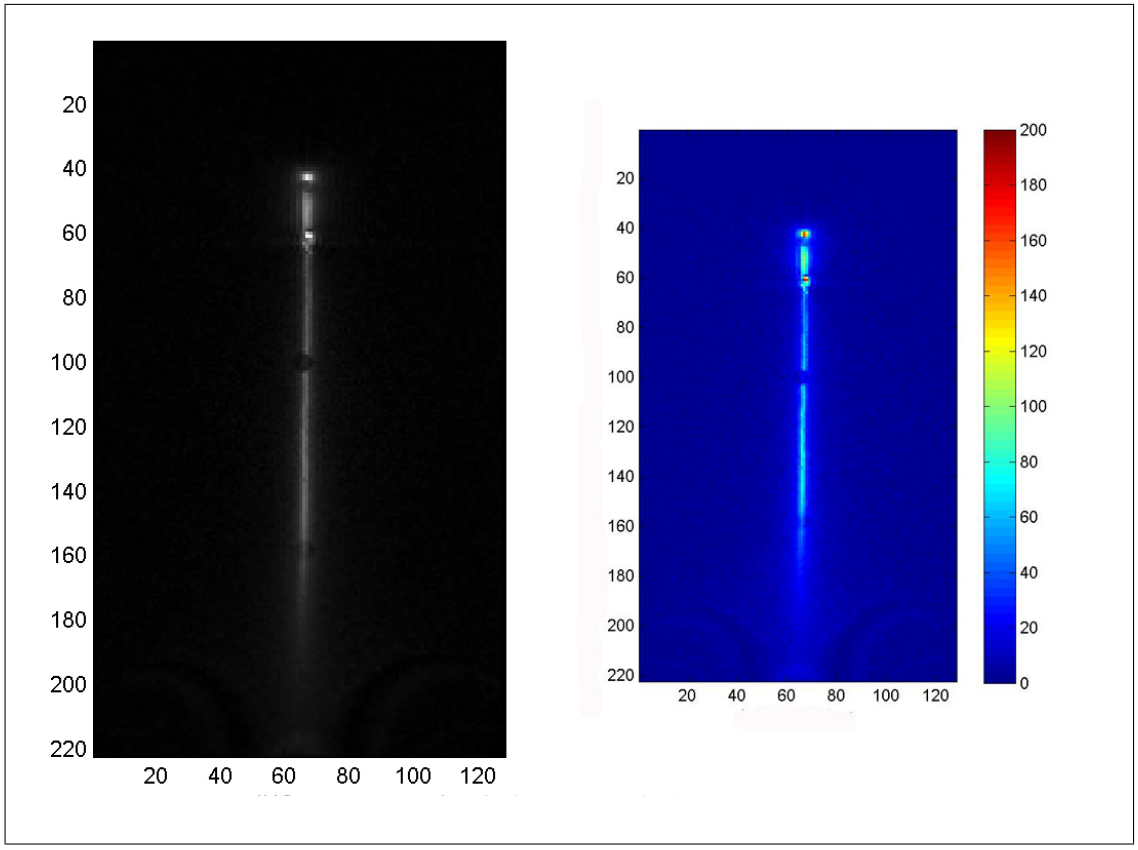

Figure 3.3 The active guidewire loop channel MRI image and the SNR map using signal magnitude image method.

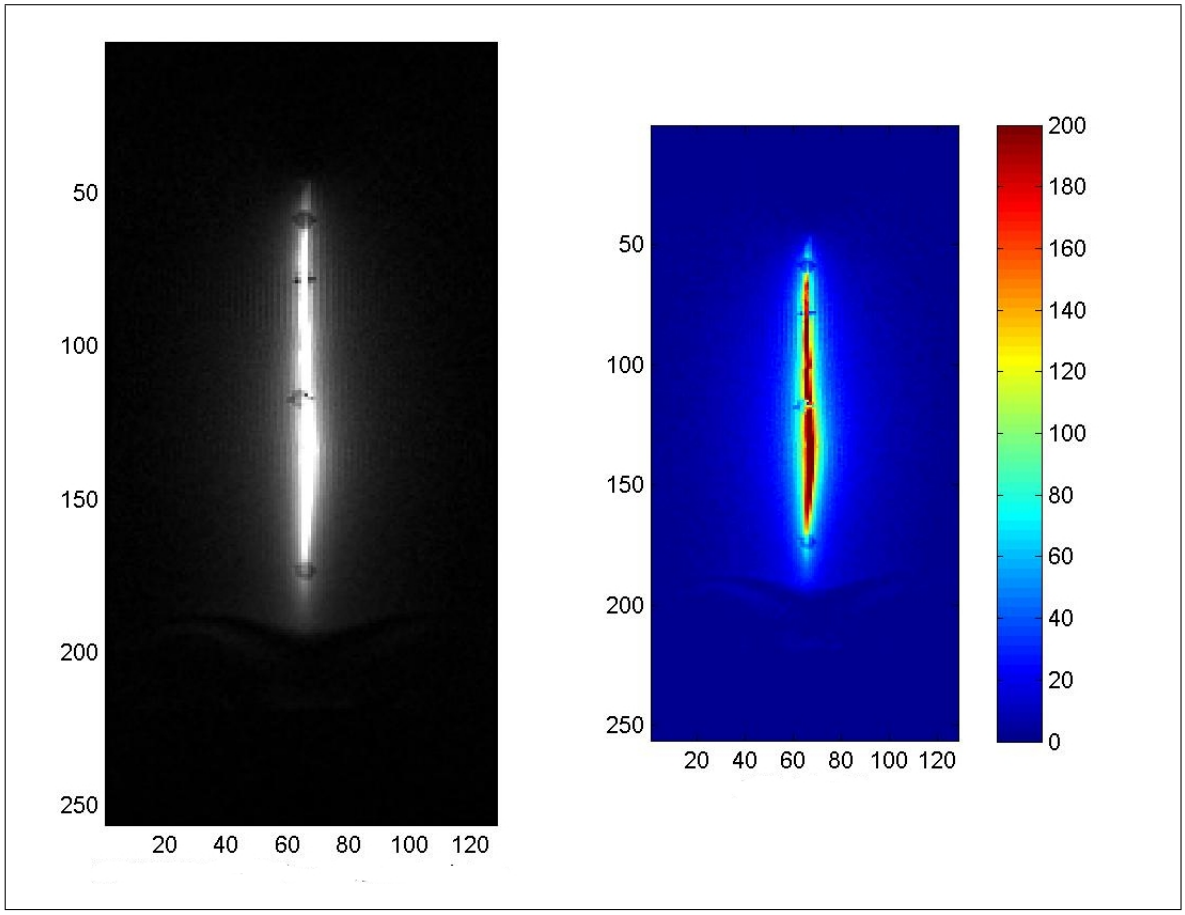

Figure 3.4 The active guidewire loopless channel MRI image and the SNR map using signal magnitude image.

Table 3.2
SNR values of guidewire antenna channels by signal magnitude image method.

	Loopless Antenna Channel	Loop Antenna Channel
Noise ROI Size	1600	1600
Noise SD	4.6848	3.8676
Correction Factor	0.6551	0.6551
Corrected Noise SD	7.1512	5.9039
Max Signal	3019	1395
Max SNR	422.16	236.28

3.3.2 Double Acquisition Magnitude Image Method

The same acquired images were used to calculate the SNR values for both channels. The calculated SNR values for loopless and loop antenna channels were 442.74 and 246.55 respectively Table 3.3.

Table 3.3
SNR values of guidewire antenna channels by double acquisition method.

	Loopless Antenna Channel	Loop Antenna Channel
Noise ROI Size	28416	28416
Correction Factor	0.6551	0.6551
Corrected Noise SD	6.8189	5.658
Max Signal	3019	1395
Max SNR	442.74	246.55

The original two scans of the both loop and loopless active guidewire channel and the subtraction image were displayed in Figure 3.5.

As demonstrated in Figure 3.6, the noise ROI was enlarged to include more pixels to reduce statistical error.

Noise values generated with the double acquisition technique were considerably less than those values from the individual magnitude image calculations alone as can

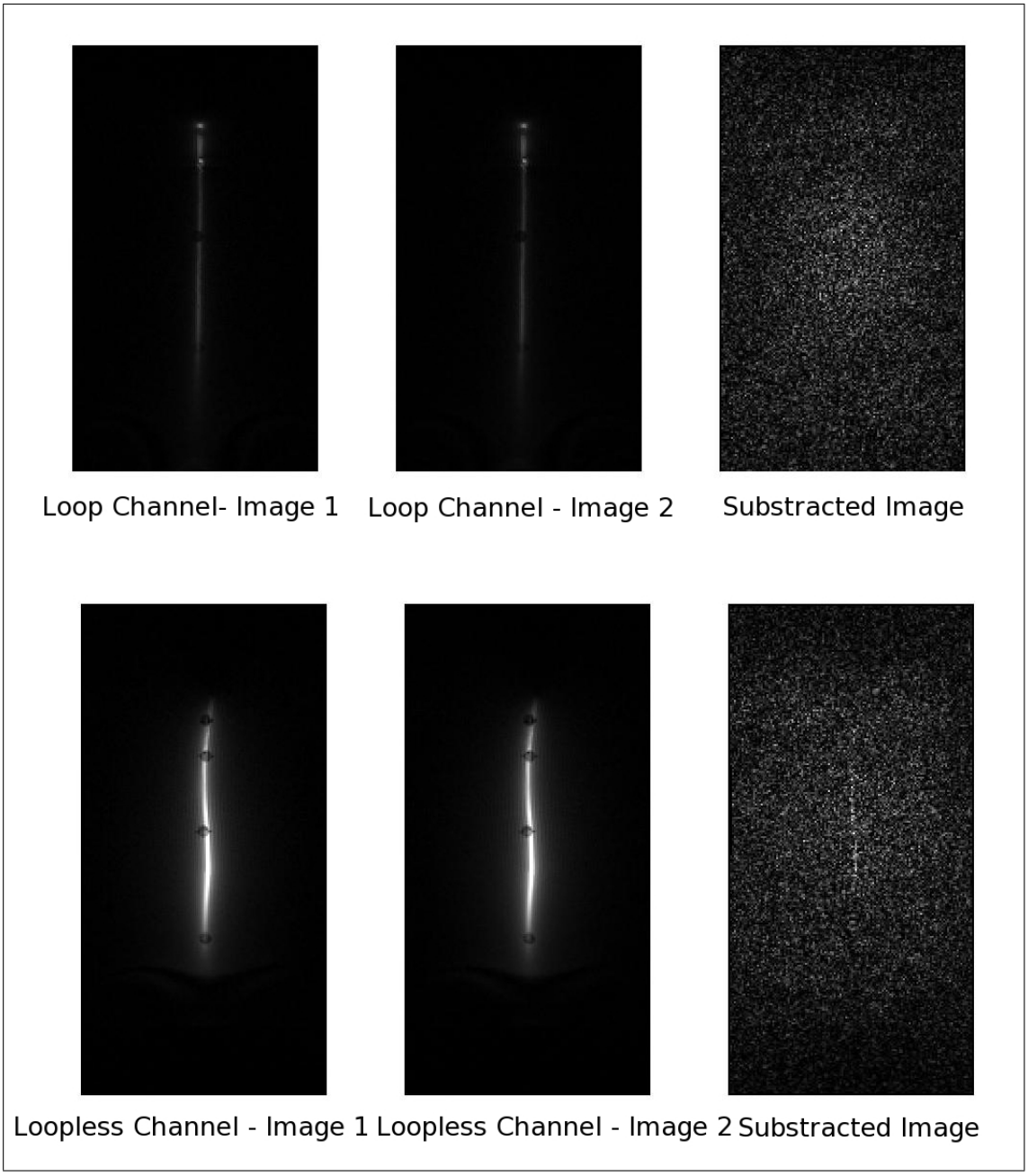

Figure 3.5 Two sequential magnitude images were acquired for both loop and loopless channel. Images were substracted and the entire substracted image was used as noise ROI. (right bottom) The active guidewire device region selected as device signal.

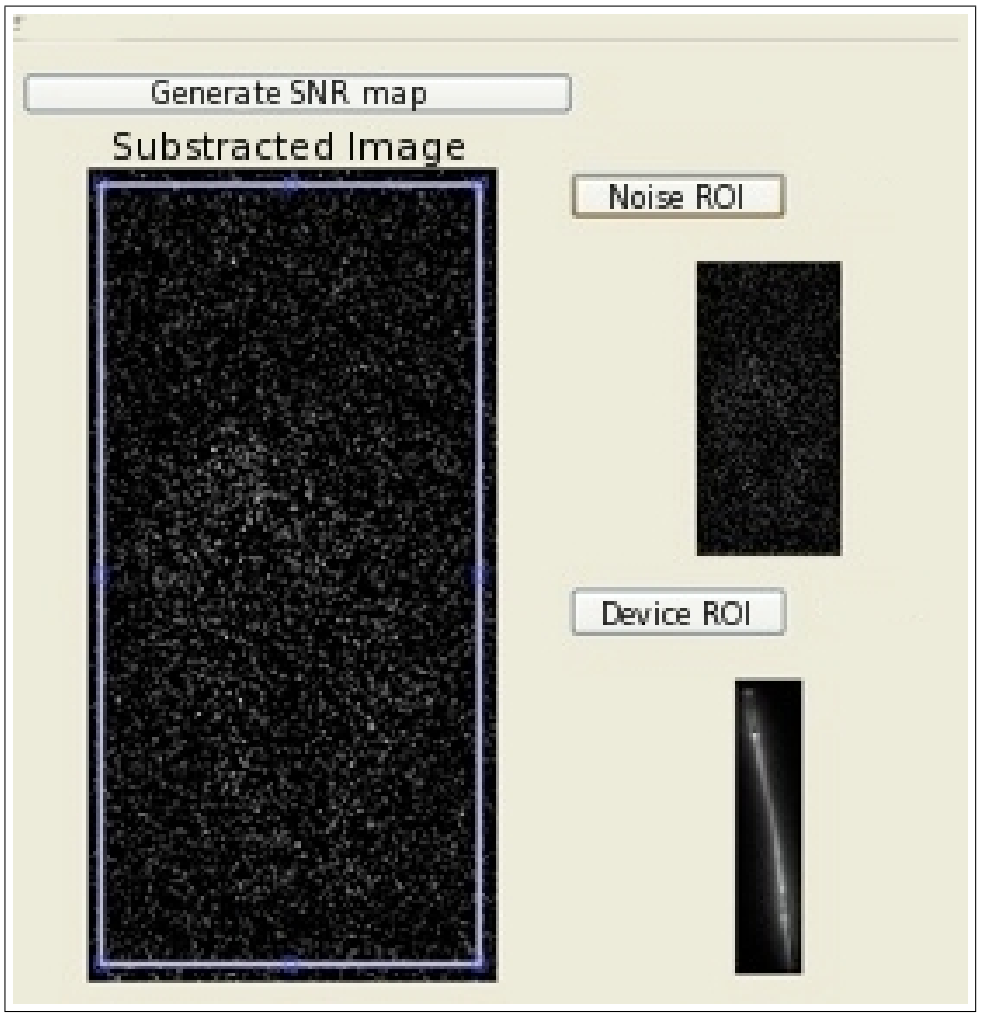

Figure 3.6 (left) The entire substracted image was used as noise ROI. (right bottom) The active guidewire device region selected as device signal.

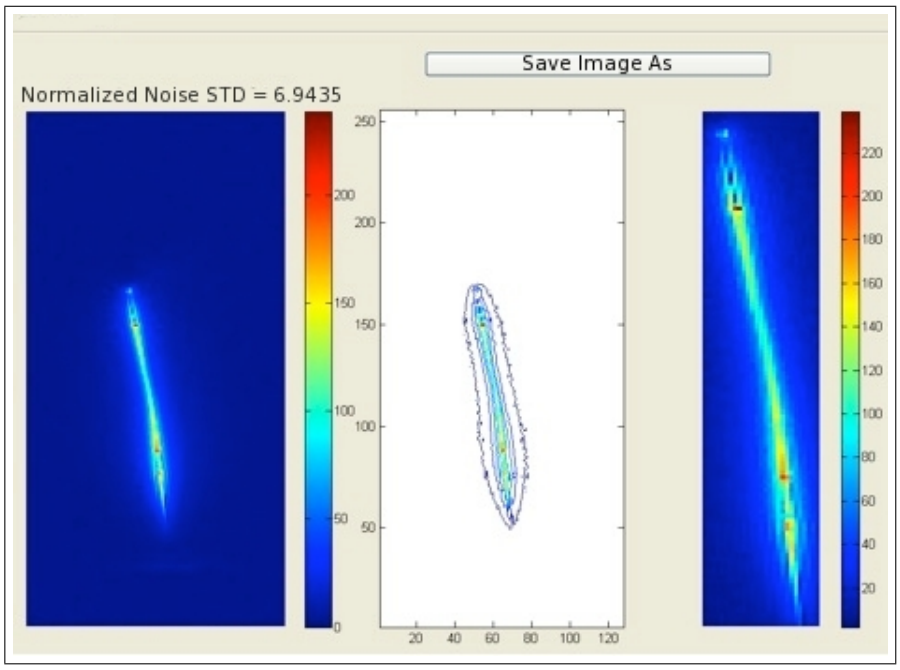

Figure 3.7 The active guide wire SNR map using subtraction method. Left: SNR map of the whole image. Center: Contour representation of the SNR map. Right: SNR map of the selected device ROI. Normalized noise STD = 6.94.

be seen in Table 3.3.

3.4 Discussion

One of the chief concerns of active device design is to have good signal "signature" relative to anatomical background. The described SNR map construction algorithm is not limited to guide wires and catheters, it is applicable to any active device designed for interventional MR procedure, further assisting operators in quantifiable assessments of device profiling functionality. The active device visualization can be a direct result of the amount of MR signal sensible to coil designs and resonant circuitry, both of which may be tuned to optimize SNR. A device with noticeable signal intensity in a phantom setting may not exhibit the same signal profile in vivo due to possible SNR distortion caused by surrounding tissue. Therefore, an SNR map is helpful in quantifying device performances and better evaluate whether or not visibility can be improved and consequently attained in live procedures. From a computation standpoint, SNR map

construction of MR images primarily depends on noise estimates. Both Single Magnitude Image Method and Double Acquisition Magnitude Image Method adopted from the NEMA standard [51] can be utilized. Since any traces of phantom or device signal inside the noise ROI will compromise the accuracy of the noise estimate, methods are implemented according to the size of regions without said traces. Single magnitude image method will be appropriate for images that contain large "air" only regions in their FOV. Alternatively, an image with very little "air" only regions can utilize the double acquisition magnitude image method to stamp out phantom and device signals, resulting in a larger area for noise ROI selection. Based on SNR computations comparing the two methods, there is no appreciable difference between the two noise estimates. The noise standard deviation from double acquisition magnitude image method was lower, resulting in higher SNR values, and the noise standard deviation error is lower as many more pixels are used in the calculation. Moreover, another option to circumvent issues concerning scans with small "air" only regions is to divide the noise ROI into selections of the four corners of a single magnitude image. One drawback for this method is the number of pixels in the noise ROI will be considerably fewer compared to the double acquisition magnitude image method, where almost the entire FOV is used for noise computation. However, the single image method is not affected by system drift artifacts that apply to the double acquisition method. If SNR maps are to be used as a dependable standard for device profile functionality comparisons, scanning conditions need to be controlled to ensure computational consistency. However there are elements that cause variations between images. First of all, the double acquisition method requires two subsequent scans (conducted under as little time elapsed as possible) with identical system parameters. Nonetheless imperfect cancellation of low frequency phantom/device signals can arise from a free floating device situated inside a water phantom. The device will experience motion on a microscale level that causes discrepancy between two supposed identical scans.

Summary, SNR maps of active multi channel devices were performed with the developed Matlab graphic user interface using two main magnitude image techniques. This Matlab GUI facilitated the comparison of active guidewire prototypes and objecive evaluation of any design modifications.

4. Whole Shaft Visibility for Active MRI Catheters Using Copper Nitinol Braided Polymer Tubes

4.1 Background

Image-guided catheter intervention using MRI remains tantalizing. Real-time imaging [11, 57, 58, 59, 60] and patient-handling [35] capabilities have been demonstrated. Nevertheless, few animal demonstrations [61, 62, 63, 64] have been demonstrated in human subjects [65, 66, 67, 68]. Clinical-grade interventional catheter devices for use during MRI, such as catheters and guidewires, remain the most significant obstacle to wider clinical translation. Reported non-clinical implementations tend to offer reduced visibility under MRI or reduced mechanical performance [69, 70].

Cardiovascular catheter devices used under X-ray guidance are visible based on their simple attenuation of incident X-ray photons, regardless of configuration or orientation. Comparable devices for operation under MRI are more complex. First of all, they must be safe for use in the high magnetic field. They must not distort the surrounding magnetic field, which distorts imaging of surrounding anatomy. They must preserve the device mechanical properties as expected by the interventional operator accustomed to X-ray operation. Finally, they must be conspicuous, from the tip throughout the length inserted in the body, for safe procedure conduct during uncomplicated and complicated procedures. Approaches to make MRI catheter devices conspicuous vary widely. Passive devices rely on intrinsic materials characteristics for visibility. Passive devices have used polymer catheters with ferromagnetic [34] or paramagnetic coatings or rings [71] to produce negative or positive contrast, respectively. Other catheters with CO_2 balloons [19] or filled with more unique contrast agents and multispectral detection such as 19-F [72] and hyperpolarized 13-C [73] have also been explored. The length of these passive devices can be made visible by coating the entire device but these may occupy a large portion of the catheter volume otherwise required for therapeutic purposes, or which may have the potential to leach into the surround-

ing blood. Off-resonance imaging techniques [74, 75] may improve the visibility of such devices, at the expense of MRI visibility of target anatomy.

Active devices, which embed antennae, and semi-active devices, which incorporate other electronics, may be more conspicuous than passive devices but have other problems. Often these have reduced visibility at the distal tip. They incorporate conductive hypotubes to provide whole-shaft visibility, at the expense of reduced flexibility or other important mechanical characteristics. Inductively-coupled markers, one semi-active approach, can be incorporated on the distal end of catheters [22, 76] and do not require long transmission lines to connect to the scanner. The catheter appearance is then limited to the distal end and may require further optical tuning [77, 78] or signal separation [79] to firmly distinguish them from background tissue. Active tip "tracking" (using special non-imaging pulse sequences) or "profiling" (using ordinary imaging) are good for robust device visualization, but traditionally track either the tip or the shaft but not both.

The original tip tracking principle [23] has been adapted to allow tip tracking along with tip orientation [37, 80] but the rest of the device location and alignment remains unknown unless it is visualized by an alternate means. Tip profiling could be accomplished with multiple or elongated coils along the length of the device [37], [81]. Although the loopless antenna design first described for guidewire design [26] is typically used for whole-shaft visibility. The loopless antenna usually is a flexible coaxial line whose inner conductor is extended by approximately a quarter wavelength (λ_m / 4, where λ_m is the wavelength in the body). This antenna design has been used in conjunction with a guide catheter [82] in addition to being modified to create active intramyocardial injection catheters and intravascular needles [36], [83]. Coaxial MRI compatible metal hypotube and wire configuration must often be used to create the antenna design. This can significantly increase the stiffness of the device, particularly as the catheter size increases.

Mechanical properties of intravascular devices play a critical role to perform successful interventional treatment. Vessel wall damage, perforation, thrombosis and

emboli are main complications that could result from improper catheter properties. The catheter should be designed according to the vessel being catheterized and target treatment [84]. The most critical mechanical properties of catheters are flexibility (bending stiffness) and torque response (torsional stiffness) [85]. The catheter flexibility determines the amount of force the catheter applies to the vessel wall as it traverses the tortous vessel path and the catheter torque response determines the amount of torsional twisting along catheter during rotational movement. The flexibility and torque response of a catheter made of monolithic biocompatible material strictly depend on the catheter dimension because elastic modulus and moment of inertia are constant for a specific material. However, for braided catheters, both elastic modulus and moment of inertia are variable. The elastic modulus is strongly dependent on the braiding material and braiding angle, the angle the braiding wires make with the longitudinal axis of the catheter. Also braiding wires inside the polymer wall increase the torque response of the catheter shaft because they impede the twisting of the structure [86].

X-ray interventional catheters incorporate a composite polymer-metal design to optimize handling and mechanical performance. Embedding metal braiding within a polymer scaffold provides pushability and torquability to advance and manipulate the device yet retains flexibility required to navigate tortuous paths [87]. This approach needs to be abandoned or modified significantly in iMRI devices because of concerns over metal susceptibility artifacts and heating. While widely-used stainless steel braiding may be inappropriate for MRI, this composite principle can be used to design antennas that are embedded into the catheter to impart whole-shaft visibility as well as favourable mechanical properties. As part of this dissertation work, a 3-channel multi-purpose catheter prototype was developed using a novel copper and nitinol wire-braided polymer hypotube design. Loop coils provide 3 individual locations on the distal end for tip location and orientation while the loopless antenna with the wire braided polymer tubing provides shaft visibility. A custom pre-amplifier box and real-time interactive system was used to allow display of these features as separate channels in different colors on the real-time imaging display. The device was tested in in vitro and in vivo animal MRI-guided experiments.

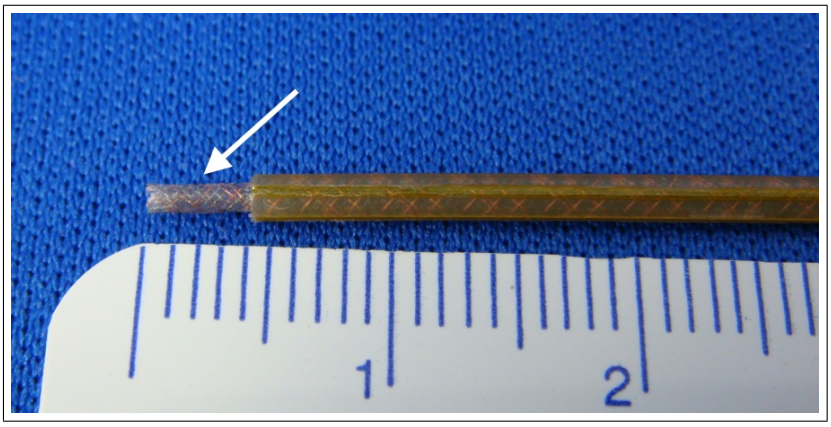

Figure 4.1 Photograph of the braiding setup and catheter shaft structure. The copper and nitinol braiding layer (arrow) exposed after outer Pebax layer is removed.

4.2 Methods

Catheter prototypes were constructed in an ISO class 7 cleanroom by using only certified biocompatible materials.

4.2.1 Loopless antenna design using braiding layers

The design of the loopless antenna was based on coaxial braiding layers that are separated by medical grade thermoplastic elastomer tubing (Pebax, Medical Extrusion Technologies Inc, Murrieta, CA) and polyimide tubing (Microlumen Inc, Tampa, FL, US). Flat (0.003 inch width, 0.001 inch wall thickness) and bare copper and nitinol wires were used for each braiding layer (Figure 4.1).

To achieve optimal design, diameter of the each braiding layer and space between two centric braiding layers was adjusted with polymer insulator material ($\epsilon_r = 3.45$) to have characteristic impedance close to the electrical load of the human body for the loopless antenna. The whip length of the dipole antenna was adjusted to have minimum resistance whip length when immersed in the 0.35 % saline solution whose measured RF electrical properties approximate within the body by using network analyzer (Agilent Technologies Model 4395A, Santa Clara, CA).

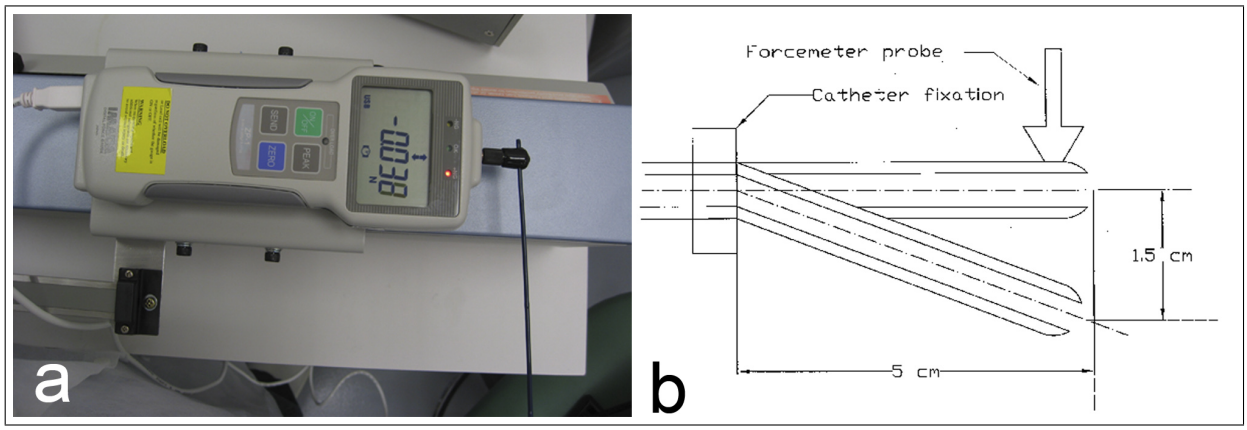

Figure 4.2 (a) The catheter distal tip was fixed perpendicular to forcemeter that was mount onto motorized stage. (b) The schematic representation of tip flexibility measurement setup.

4.2.2 Mechanical evaluation of braiding configurations

Different braiding configurations were prepared in terms of different nitinol:copper wire ratio in the braiding and each braiding configuration was tested in terms of flexibility and torque response.

4.2.2.1 Flexibility Test. The aim is to compare the force required to deflect the distal tip of the catheter same amount for different nitinol:copper wire ratio braiding configurations. The catheter distal tip was connected to the force meter in a way that the tip is perpendicular to forcemeter Figure 4.2a. The forcemeter was mounted onto motorized linear stage that moves at a constant speed. The catheter was fixed 5 cm away from the distal tip to prevent any damage on two solenoid coils at the tip. The force was measured that was required to bend the catheter by 1.5 cm using digital forcemeter as schematic representation shown in Figure 4.2b.

4.2.2.2 Torquability Test. The aim is to demonstrate torque transmission ability from proximal end to the distal end of the catheter shaft. The distal tip of the catheter was attached to a fixed collet that is free to rotate axially. The distal tip of the collet was marked and rotation angle was measured relative to a fixed plat-

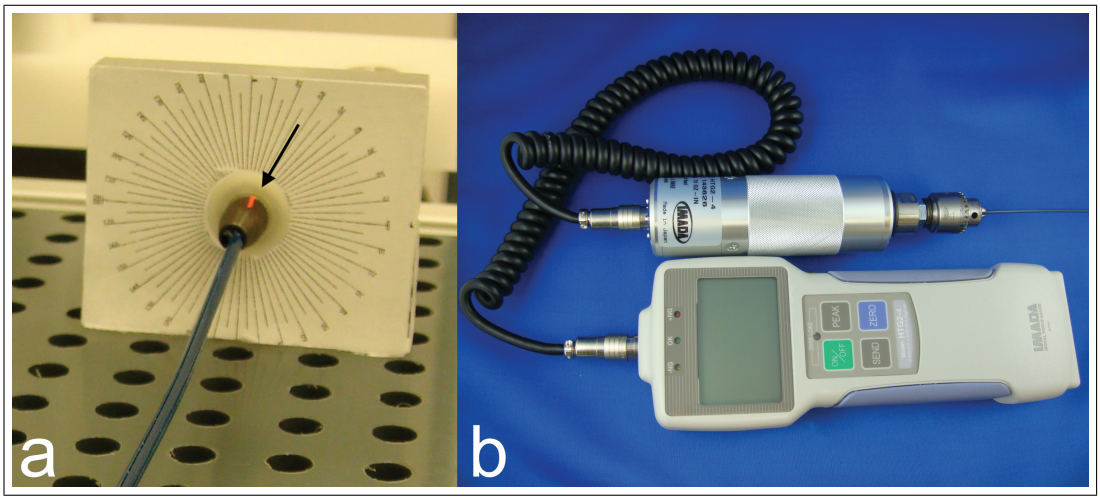

Figure 4.3 (a) Torque transmission test fixture setup. Distal tip of the shaft was fixed into a freely-rotating collet (arrow) that indicates the angular response to torque. Degree of rotation can be measured relative rotation of the marker to the angular scale. The arrow shows the marker on the collet. (b) A torque meter on the proximal shaft recorded transmitted torque after 90-270^0 tip rotation.

form (Figure 4.3a). The catheter proximal hub was mounted to a digital torque meter (IMADA Inc., HTG-2, Northbrook, IL, US) and then peak torque values were recorded when the distal tip rotated 90, 180 and 270 degrees respectively (Figure 4.3b).

4.2.3 Catheter Construction

The 7 Fr active catheter was designed to have three distal loop coils and two coaxial braiding layers used as a loopless antenna (Figure 4.4).

Pebax (thermoplastic elastomer) custom design extruded tubing was used as the core layer to construct the active catheter. The core tubing design has four grooves also to provide enough space for micro coax cables that used as transmission lines for distal loop coils. The braiding layer of the core tubing lies under the grooves and forms the core conductor layer of the dipole antenna (Figure 4.5).

The three loop coils were formed at the distal tip of the inner polymer shaft tubing and first and third coil were shared same micro coax cable as a transmission line and second coil was connected to separate micro coax cable that has 0.012 inch

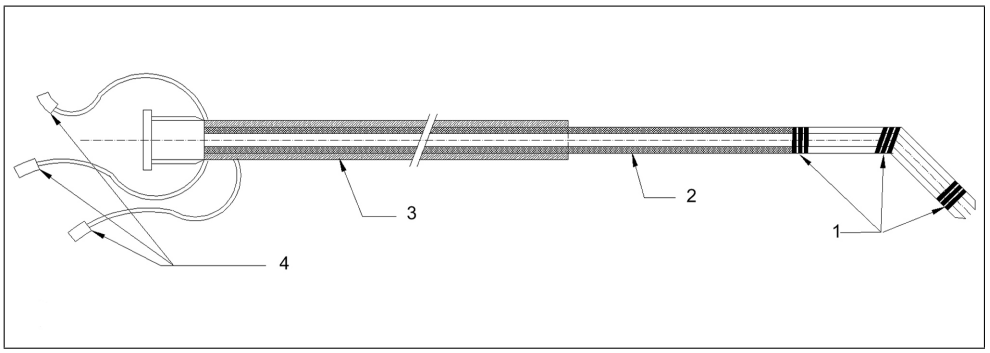

Figure 4.4 Schematic of a finished 7 Fr guide catheter with a 0.035 inch guidewire compatible lumen. (1) Three solenoid coils incorporated in the distal shaft for tip profiling (2) Inner nitinol-copper braiding layer used as a core conductor of the loopless antenna (3) Outer braiding layer used as a shield for the loopless antenna (4) micro-miniature connectors (MMCX).

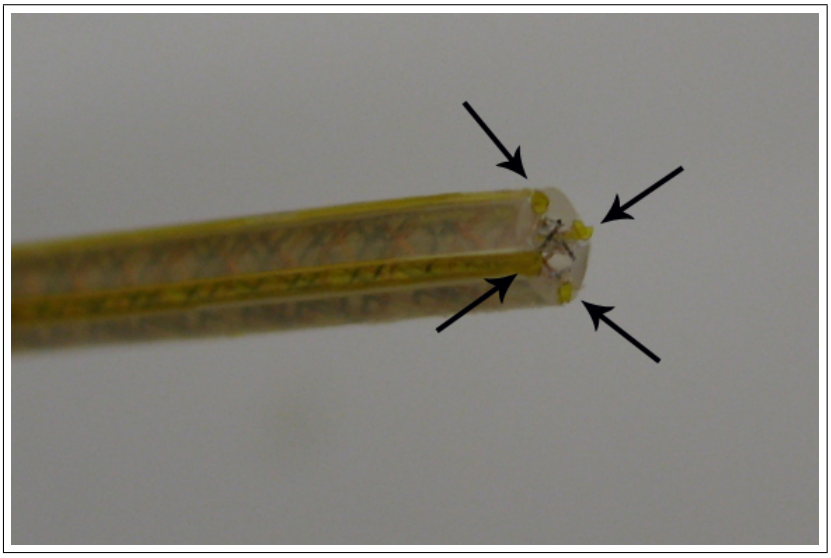

Figure 4.5 The inner polymer shaft that has copper and nitinol wire braiding under four grooves (arrows) that provides housing for distal loop coils transmission lines.

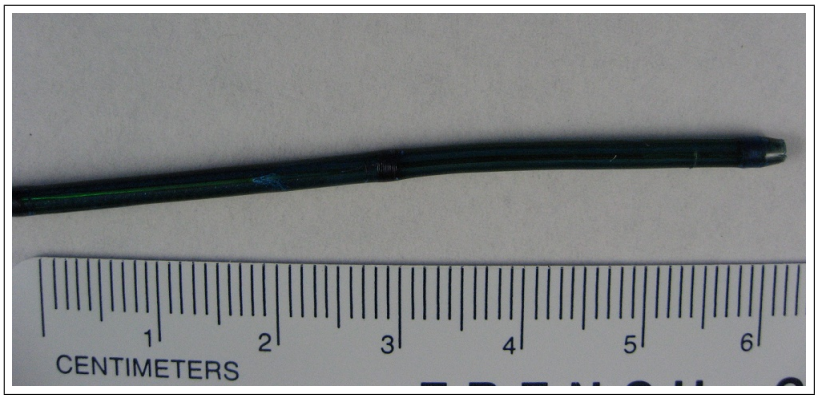

Figure 4.6 The distal tip of the catheter was shaped to have atraumatic tip.

outer diameter. Coils were placed 1 inch apart form each other. The three coils were embedded into distal catheter body to determine catheter tip orientation in addition to distal tip location. The braided second layer was placed over the first one after all coils and micro coax transmission lines were positioned over the shaft. The braiding portion was positioned in such a way that whip length is equal to minimum resistance whip length. Both layers were fused together by heating up to 380 F. Then the distal tip of the catheter was rounded and reduced radial profile to have atraumatic tip Figure 4.6.

The proximal end of each antenna is connected to the dedicated the matching and decoupling circuits. All loop coils and loopless antenna channel were matched to 50 Ω in a saline bath (0.35 % NaCl, $\epsilon_r = 77$, $\sigma = 0.6$ S/m) by using dedicated matching/detuning circuit boxes at the Larmour frequency of 1.5 T MR scanner. Figure 4.7 shows the complete form of active catheter that has three separate receiving antenna channels.

4.2.4 Visibility Performance Testing under MRI

All MRI scans were performed at 1.5 T (Espree, Siemens Medical Solutions USA, Inc., Malvern, PA) scanner. The active catheter was connected to the MR scanner by using a custom 4-channel pre-amplifier interface (Stark Contrast MRI Coils Research, Erlangen, Germany). During all scans, active catheter channels were used

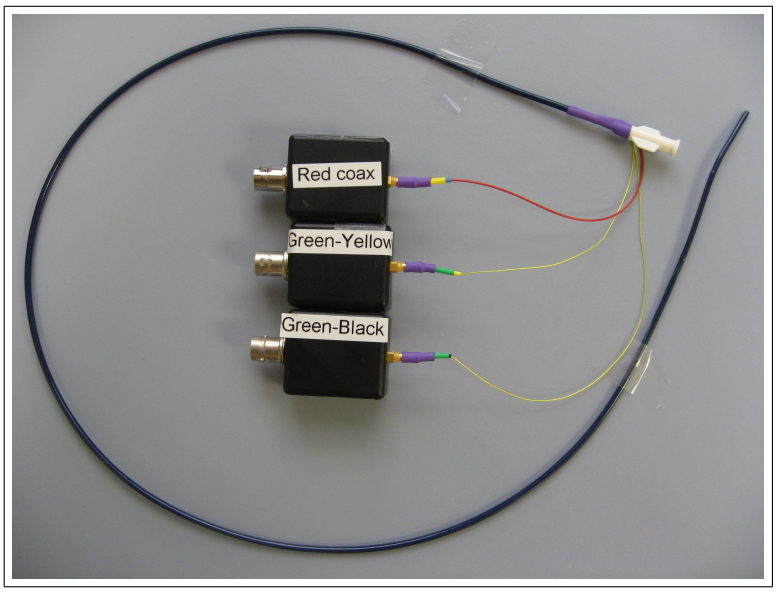

Figure 4.7 The picture of 7 Fr guiding catheter with matching-detuning circuit boxes.

in receive-only mode.

4.2.4.1 Visibility In Vitro. 0.35 % NaCl solution filled phantom was used to simulate loading conditions ($\epsilon_r = 77$, $\sigma = 0.6$ S/m) of an active catheter inserted into a human body. Real time MR imaging was performed using a steady state free precession (SSFP) sequence with slice thickness 5 mm, repetition time (TR) 3.68 ms, echo time (TE) 1.84 ms, matrix = 192 X 108 and bandwidth = 700 Hz/pixel. The first and third loop channels of catheter were colored green and second loop channel colored red and loopless antenna channel was colored blue using a customized interactive real-time MRI interface. The in vitro signal-to-noise ratio (SNR) profile of the active catheter was mapped in normalized SNR units from a single magnitude image [88] using Matlab (Mathworks Inc., Natick, MA). A reproducible noise region of interest was selected, and corrected for the number of active catheter receiving channels [89].

4.2.4.2 Visibility In Vivo. In vivo experiments were conducted on anesthetized pigs in protocols approved by the National Heart Lung and Blood Institute Animal Care and Use Committee. A balanced SSFP sequence used the following parameters:

TR/TE, 3.72/1.86; flip angle, 60^0; slice thickness, 6.0 mm; matrix, 192 X 108; bandwidth, 797 Hz/pixel. The same custom real time MRI interface was used to colorize each catheter channel separately. From a transfemoral approach, the active catheter was advanced retrograde through the aorta under real-time MRI guidance [58].

4.3 Results

4.3.1 Flexibility Test Result

Shaft stiffness was directly related to braiding composition stiffness. When the number of nitinol wires is reduced in the composite, the flexibility increases dramatically (Figure 4.8). The commercial braided (stainless steel) 7 Fr Cook Shuttle introducer sheath stiffness was comparatively greater than all tested braiding configurations.

4.3.2 Torquability Test Result

Shaft torque transmission also is related to the stiffness of the braiding layer. As the cooper wire ratio increases in the braiding layer, shaft torque transmission decreases (Figure 4.9). The 7 Fr steel Shuttle introducer sheath showed better torque response. Flexibility and torquability of the catheter shaft that has a 12:4 (NiTi:Cu) braiding wire ratio were similar to the catheter shaft that has an 8:8 (NiTi:Cu) ratio. Therefore, because copper has superior conductivity, we chose the 8:8 (NiTi:Cu) ratio for all subsequent experiments.

4.3.3 Visibility Performance Results

The distal loop channels and the entire catheter shaft were conspicuous relative to background during in vitro experiments (Figure 4.10). It was shown also that the

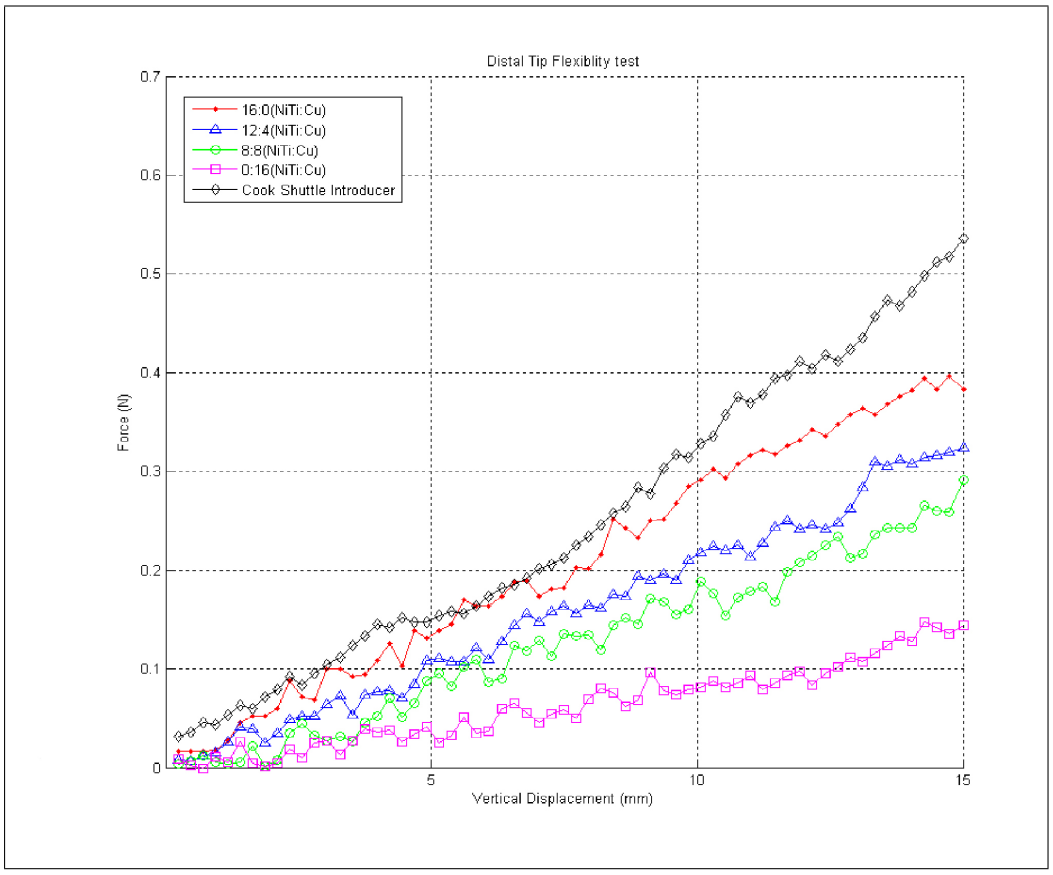

Figure 4.8 Distal tip flexibility for different braiding layer configurations. Resistance force at the catheter distal tip was measured while the shaft was bent from 5 cm away until the tip reaches 1.5 cm vertical displacement.

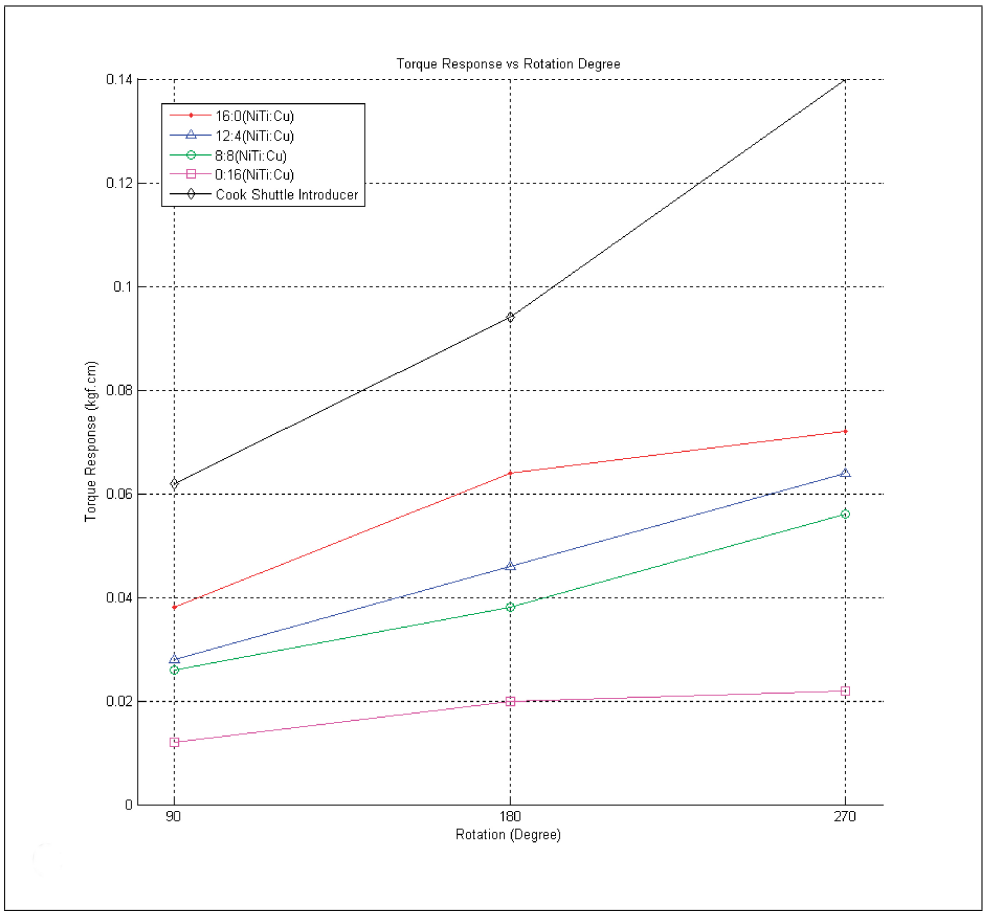

Figure 4.9 Comparative torquability values for different braiding layer configurations. Higher torque response values indicate greater torquability.

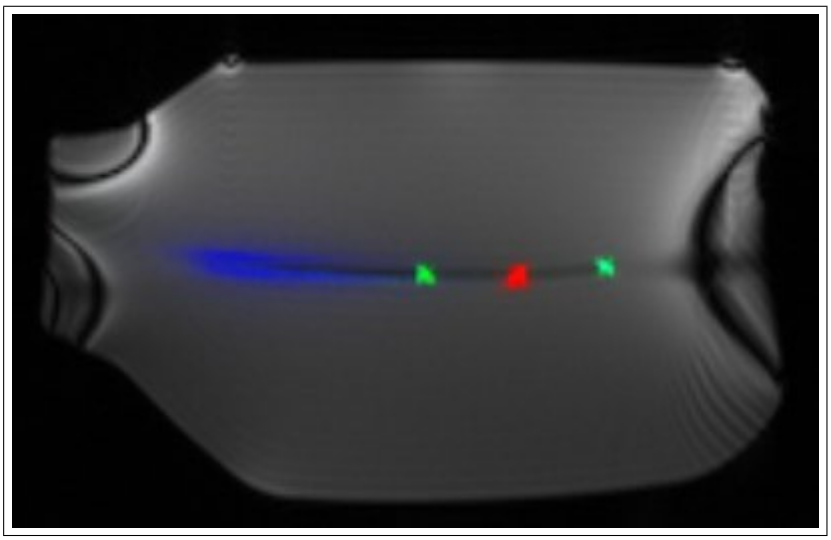

Figure 4.10 Phantom MR image acquired with three channel catheter. Independent catheter receiver channels allow colorized reconstruction of the tip and third coil, green; middle coil, red; catheter shaft, blue.

catheter shaft has good longitudinal signal homogeneity and all loop coils are visible while it was advanced through the body (Figure 4.11).

The SNR profile map of the entire system (Figure 4.12) shows that the sensitivities of the loopless (shaft) antenna and distal (loop) antennas are similar, and sufficient to distinguish distal shaft from background.

4.4 Discussion

The design and testing of a clinical grade multi channel active catheter was reported for interventional MRI. It was showed that it combines suitable mechanical performance with MRI visibility. Specifically, the braiding and polymer materials were manipulated to serve both mechanically and electrically as a loopless antenna, to address the clinical requirement for whole-shaft visibility. In addition, the catheter shaft was engineered to accommodate multiple transmission lines without increasing the catheter profile. These transmission lines were used for distal microcoils to indicate distal catheter position and orientation.

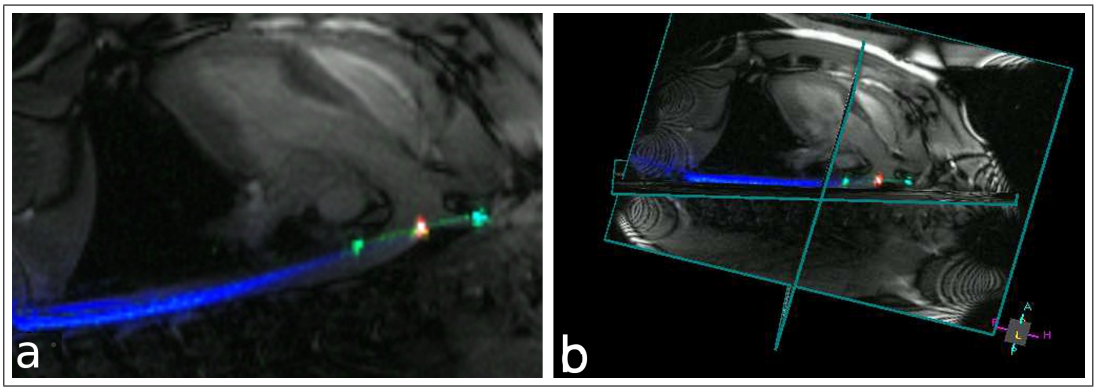

Figure 4.11 (a)The active catheter was inserted percutaneously from the femoral artery, through the aorta, and into the left subclavian artery. (b) Multi-slice volume-rendered real-time MRI of procedure described in panel (a) depicting the anatomic context. Device-related signal is evident in all slices. Independent catheter receiver channels allow colorized reconstruction of the tip and third coil, green; middle coil, red; catheter shaft, blue.

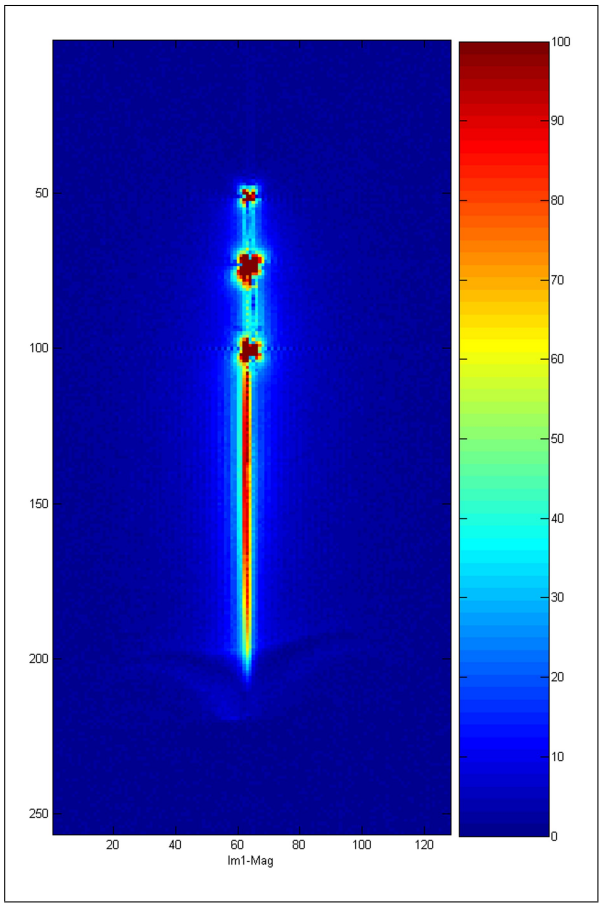

Figure 4.12 Signal-to-noise ratio profile of the active laser catheter is mapped in normalized SNR units.

Loopless antennae are attractive candidates for whole-shaft MRI catheter visibility because of relatively homogeneous signal profile and high near-field sensitivity. The braided wires were used as conductors and polymers as insulators because of their mechanical properties. However the spacing between braided wires attenuates antenna signal. To address this, the whip length was tuned to minimize the antenna input resistance and optimize SNR [26].

Interventional catheters commonly incorporate steel braiding which is incompatible with MRI. Nitinol has low electrical conductivity, σ (1 x 10^6 S/m) but great flexibility and kink resistance. Copper, which has higher electrical conductivity (σ = 5.8 X 10^7 S/m) but lower strength and torque response. These two wires were combined in composite braids and empirically determined an optimum braiding configuration of nitinol:copper 8:8. The resulting design is less stiff than a bigger size commercial steel introducer sheath system as expected, but highly conspicuous for interventional MRI. Alternatively, nitinol braids could have been plated with highly conductive metal, such as silver, σ = 6.28 X 107 S/m, or gold, σ = 4.26 X 107 S/m) to exploit the skin effect of RF transmission and retain the mechanical properties of nitinol. We currently was postponed this approach because of its complexity.

In order to provide the desired mechanical properties within the noted dimensional constraints, some catheters incorporate dual inner- and outer-braided wires. Each is typically embedded in a polymer to impart desired mechanical properties. The inner braided wire system is typically the primary source of compression resistance. Compression resistance allows the catheter to advance through the vessel against friction without undue axial compression ("accordion damage") of the shaft. Compression resistance also affords tactile feedback to the operator. By contrast, the outer braiding typically imparts torque transmission because of its larger moment-arm relative to the shaft axis. During catheter navigation, friction may store undesired torque energy that may release in spring-like fashion with unintended consequences. Our catheter shaft was assembled to form a tapered transition between the catheter whip and double-braided shaft to provide smooth and strong transitions between distal and proximal part of the device.

Long conductive transmission lines may subject to heat during MRI [90]. We used a positive-intrinsic-negative (PIN) diode in decoupling circuits to reduce heating due to amplification of the electric field around the catheter conductors during RF transmission. The PIN diode shorts out the connector end of the antenna during MRI excitation when a positive direct current voltage is supplied by the scanner. The short circuit is transformed to high impedance at the antenna junction, thereby minimizing current and heating. During reception, the diode is biased off, and the MRI signal is conducted from the catheter antenna channels to the scanner. Heating tests will be performed as we incorporate this catheter design into specific devices with particular decoupling circuitry.

As a summary, 7 Fr active three channel multi purpose catheter was developed whose whole shaft can be visible under real time MRI by designing a loopless antenna by using current braiding layers embedded into catheter shaft. Additional two channels provided tip visibility and distal tip orientation determination. Each channel can be color coded and displayed separately in the real time MRI display.The mechanical performance of device and visibilitity under real time MRI were confirmed both in vitro and in vivo in animal experiments. Mechanically, optimum braiding configuration (8 copper wires and 8 nitinol wires) was selected after confirming that when the copper wire ratio in the braiding increases, the flexibility of the shaft also increase and shaft toruqability decreases. Because identifying and tracking the whole length of the catheter relative to background anatomy during real time MRI improves the procedure safety, such active catheter devices may enable a wide range of MRI guided cardiovascular procedures.

5. RF Safety Test

5.1 Introduction

Because metallic guidewires or catheters are essential part of interventional MRI, the security aspects of such devices are of great importance. Both loop and loopless antenna design are made of metallic parts and also required metallic transmission lines such as coaxial cables. During RF excitation under MRI, in addition to the magnetic field B_1, an electric field E induces currents called eddy current (at the same frequency) in the metallic wire placed in the MR scanner. Furthermore, the metallic wire concentrates the RF electric field, and may lead to a significant temperature increase [91, 92]. Heating may emerge if conductors of sufficient length are present in the RF field resonates with RF waves along the conductor. If such a resonance occurs, the incident RF wave is bounced back and forth along the conductor in such a way that standing RF waves are formed. It causes the storage of electrical energy along the device [93, 94]. The measure of RF power delivered to the patient is called Specific Absorption Rate (SAR), typically in W/kg, calculated as (Eq. 5.2)

$$SAR = \frac{\sigma |E|^2}{\rho_m} \tag{5.1}$$

where σ is electrical conductivity, E is the rms electric field strength in and ρ_m is the mass density. SAR also can be calculated from its heat effects as

$$SAR = \frac{C_h \Delta T}{\Delta t} \tag{5.2}$$

where ΔT is the temperature rise, Δt is the exposure time, and $C_H = 4180$ J/kg.^{0}C is the specific heat capacity [95].

The Food and Drug Administration (FDA) of the United States Department of Health and Human Services has safety guideline dealing with physiologic effects of MRI [96]. The whole body RF exposure limitation indicated in this guideline was

summarized in Table 5.1.

Table 5.1
FDA Guideline recommended limits for SAR.

Site	Dose	Time (min)	SAR (W/kg)	Localized Temperature (^{0}C)
whole body	averaged over	15	4	38
head	averaged over	10	3	38
torso	per gram of tissue	5	8	39
extremities	per gram of tissue	5	12	40

The whole body SAR can be calculated by calorimetry method described in NEMA standard [97]. Two different size phantoms are needed during calculations. A physically small filler phantom that is filled with a NaCl solution whose conductivity is less than 0.003 siemens/meter is used for calibration of tip angles. Another test object phantom is used with the calorimetric method of SAR measurement. This phantom is filled with aqueous NaCl solution whose concentration is equivalent to body conductivity. The test object phantom is placed in the MR scanner at isocenter and smaller phantom is placed centrally within it. After the tip angle calibration, the phantom is scanned with enough acquisitions to ensure the final and initial temperature difference is greater than 4 ^{0}C. The energy absorbed by the phantom can be calculated as

$$E = Mc(T_f - T_i) \tag{5.3}$$

where M is the mass of filler phantom, c is the specific heat constant and T_f and T_i are final and initial temperature of the filler phantom respectively.

The average power during the scan is calculated in watts from the scan time

$$P = \frac{E}{\tau} \tag{5.4}$$

where τ is the total scan time in seconds.

Then the apparent SAR can be calculated as

$$SAR_{app} = \frac{P}{M_{body}} \tag{5.5}$$

where M_{body} is mass of the test object phantom that is equivalent to average body mass.

Many recent studies have shown that the specific absorption rate (SAR) measured in the presence of a metallic interventional device can overcome the SAR limitation [94, 98]. This SAR elevation induces an increase of temperature in the vicinity of the guidewire. The heating close to the guidewire follows the tissue bio-heat law established by Pennes in 1948 [99]. According to this law, local heating can be defined as the algebraic sum of the following energies: 1) the metabolic activity of the cells forming the surrounding tissues, 2) the energy evacuated by the blood flow irrigating the tissues, and 3) the energy concentrated locally by the SAR. Without RF transmission, the first two terms equilibrate the temperature of the region at a steady level equal to the Body temperature. During a clinical MRI examination, the third term adds local heating by SAR. Indeed, since the metallic wire concentrates the RF E-field and presents an RF-induced current, the third term is emphasized in the close vicinity of the interventional device that has metal components longer than the quarter wavelength [100].

The current MRI device RF heating tests are performed according to American Society for Testing and Materials (ASTM) standard [101]. This standard outlines phantom shapes and fill material compositions to simulate physiological tissue conditions for evaluating heating. An acrylic rectangular box (with optional head/neck shape on top) filled with a gelled material is recommended to simulate body shape and tissue properties. Either polyacrylic acid (PAA) [0.8g/L NaCl and 5.85 g/L] or Hydroxy Ethyl Cellulose (HEC) can be used as a gelling agent in the distilled water solution to reduce bulk transport and convective heat transfer. Device location to generate maximal heating should be determined with either simulations or multiple experiments and then temperature probes and an RF-intensive sequence should be

used for evaluating device heating. While this standard provides some guidelines for device heating evaluation, variations can be made as long as they are well outlined and justified.

Preliminary studies performed by several groups have shown that local RF heating occurs primarily at the wire tip for partially inserted long conductor devices [91, 102]. However, there may be other locations on the guidewire that have local peaks of heating, but the guidewire tips are the main concern for clinically relevant situations regarding patient safety. Attempts to characterize the RF heating have tended to set up experiments that represent worst-case conditions and have typically found that these conditions routinely exceed established safety thresholds, making these long conductive guidewires unsafe for use in the scanner. It was aimed instead to examine the variables such as inserted guidewire length, scanning parameters, guidewire position in the phantom that affect wire tip heating and from heating experiment analysis find the range of operating conditions in which the prototype guidewire can be used in a safer manner in the MRI environment.

5.2 Methods

Heating tests were performed to evaluate the RF induced temperature increase characteristics in an in vitro phantom of a 0.035 inch two channel guidewire and 7 Fr three channel guiding catheter designs under MRI.

5.2.1 Phantom Preparation

An acrylic (an electrical insulator and non-magnetic) rectangular phantom was prepared to simulate the RF loading condition that would occur with a patient in an MR scanner. The phantom was formed based on the ASTM standard [101] with modifications to represent the groin and femoral artery anatomy. A femoral artery plastic model (Angiogram Sam, Lake Forest Anatomical, Lake Forest, IL) was utilized within

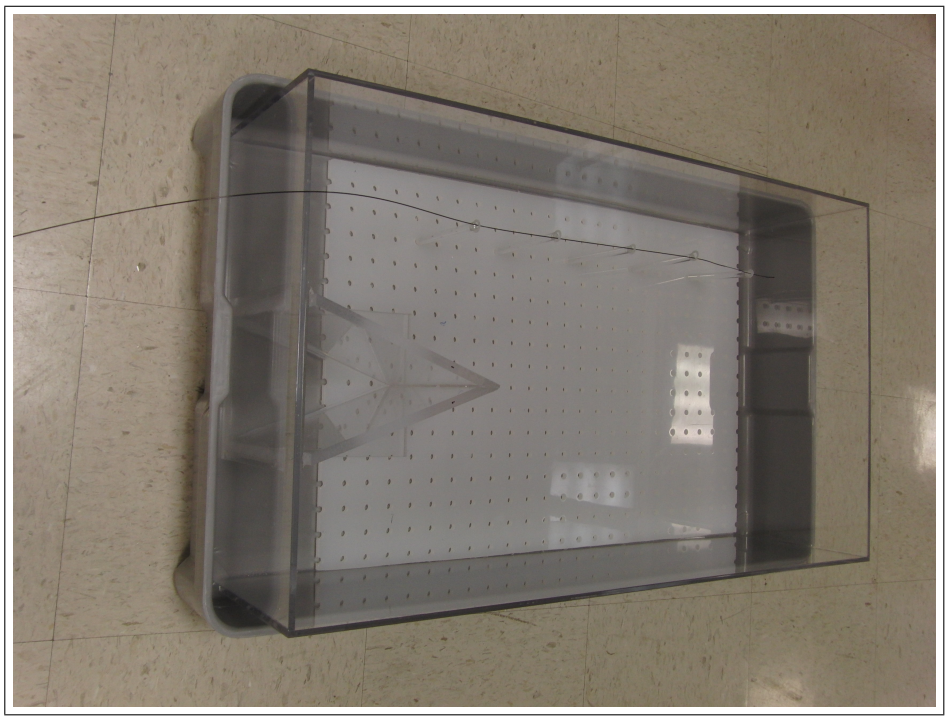

Figure 5.1 The pictures shows that guidewire was offset to the side and its position was fixed by acrylic posts.

the phantom to provide a realistic track for both the active guidewire and catheter. This plastic model is based on hundreds of angiograms to represent healthy vessel sizes and contours of an average sized person. To determine the vessel placement and other dimensions, MR angiographic data on a series of subjects was used to calculate the other anatomic distances. The vessel structure was supported in the middle of the phantom with acrylic posts (Figure 5.2). Also an appropriate size non metalic peg board that has 1 inch interval between holes was prepared to change the guidewire position horizontally relative to the center of the phantom during experiments. Acrylic posts were used to stabilize the guidewire position for each configuration (Figure 5.1). The phantom was filled with a polyacrylic acid gel (Polyacrylic acid 5.85 g/L, 1.32 g/L NaCl, deionized water with conductivity less than 1 mS/m, 0.3 % bisacrylamide, 0.05 % TEMED, 0.08 % ammonium persulfate doped with 0.45 % sodium chloride). The gel's permittivity (75) and conductivity (0.65 S/m) were measured with a network analyzer (HP 4195A, Hewlett Packard, Palo Alto, CA) using a custom-built parallel-plate capacitance testing probe. The measured values are representative values for human soft tissues at 64 MHz [103].

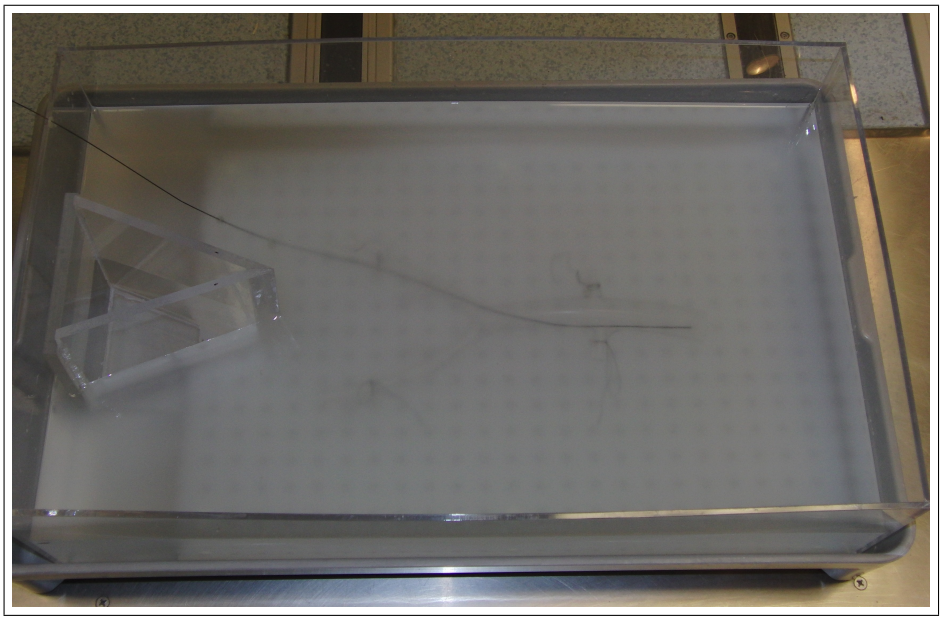

Figure 5.2 The final phantom picture with the active guidewire test sample was placed in place. The femoral artery vessel model was placed inside the phantom based on the average measurement taken from clinical MR angiographic data.

The phantom was placed at the top end of the spine array and centered on the table. The entire container was placed in a secondary base on top of the scanner table to protect the scanner in the case or any leaks from aqueous phantom. The isocenter landmark was placed six inches below the bifurcation of model iliac arteries which represents the typical landmark position for femoral artery imaging.

5.2.2 Probe Placement

Fiber optic temperature probes (FISO Technologies, Quebec, Canada) were placed at locations where the induced heating is expected to be greatest. These locations for the guidewire are guidewire tip, the proximal end of the distal tip solenoid coil, junction point of the loopless antenna channel. Another temperature probe was placed on a quarter wavelength back from the junction point during initial experiment to check if additional probes are necessary or not. For the guiding catheter, the three probes were placed next to distal loop coils and another one was placed over the junction point of the catheter loopless channel. Another reference probe was inserted inside the gel phantom away from the guidewire. The temperature sensors have a resolution

Figure 5.3 The Final RF heating test setup.

of 0.1 ^{0}C and their sensitivity volume do not exceed 1 mm in radius. The temperature recording rate was determined as 60 times per minute. The phantom was placed in an MR system. The patient comfort fan was turned off inside the MR system bore and the hole between the MR scanner room and control room that allows to extend fiber optic temperature probes to outside the room was also blocked to prevent movement of air inside the MR system bore while performing the temperature measurements. Also the phantom was covered with a lid after the guidewire and probes were in place to minimize the effect of air flow on the temperature measurements (Figure 5.3).

Before starting to each experiment, the phantom temperature was monitored for at least two minutes to make sure that the temperature fluctuation of the phantom material is not more than 0.2 ^{0}C. The scanner room temperature should be 23 $\pm$ 3 ^{0}C [101]. Also temperature recording was begun at least 1 minute prior to the start of the MRI scan and stopped at least two minutes after MRI scan. The scanner bore and room temperature was measured for 15 minutes before scanning and for 5 minutes after scanning.

An RF field with SAR of at least 2 W/kg averaged over the volume of the

phantom is applied. The temperature rise on or near the implant was measured using fiber-optic thermometry probes during the approximately 15 min of RF application, or other appropriate period, depending on the mass and thermal conductivity of critical parts of the device. Temperature measurements at one or more fixed locations away from the device serve as the control for RF field comparison between tests.

5.2.3 Phantom Calibration

The local temperature rises at the secured fiber optic temperature probe locations was determined without the active guidewire present by using the same MR scan parameters. The whole body averaged-SAR was determined using calorimetry [97]. The gel was stirred well to ensure proper mixing and then the average baseline temperature of the phantom was measured. The real time MRI sequence was run and the average temperature was recorded to determine the whole body averaged SAR. Also, the result was compared with the local temperature rise at the reference probe location in guidewire heating testing.

5.2.4 Test Protocol

The insertion length, horizontal offset from isocenter and isocenter landmark position were determined as main parameters to determine safety region for both devices. All required MRI scans were performed on the 1.5 T Espree MR scanner (Siemens, Erlangen, Germany). The phantom weight was inserted as 90 kg to mimic average patient weight. The real-time IRT sequence was used with the following parameters: TR/TE, 3.67/1.84 ms; Slice Thickness, 6mm; Flip Angle, 45^0; FOV, 330 x 248 mm; Matrix, 192 x 144, bandwidth 700 Hz/px. Scout images were taken for proper slice positioning. The guidewire and catheter was first placed into the anatomical femoral artery model. The phantom was centered on the table and isocenter landmark was aligned just the middle of the phantom. The temperature increase values were recorded for different insertion lengths. Then the vessel model was replaced with non metalic

pegboard and pins that hold the guidewire stable to determine the limits for horizontal offset and isocenter landmark position relative to device tip for each device. The femoral artery access point was designed on the phantom to mimic realistic guidewire geometry through heating experiments. The isocenter landmark position was changed relative to phantom center and device tip respectively to cover more possible temperature change characteristics. The sample device was placed maximum allowed horizontal offset determined by previous experiments,from the center and inserted until critical insertion length was inside the phantom. Because the phantom length was only 60 cm, the isocenter landmark was first centered to the device tip and then 20 cm offset from the center both ways. Then the landmark was positioned to the center of the phantom and again 20 cm offset from center both ways to cover larger region. Each set of experiment was repeated three times with different guidewire and catheter samples sequentially.

5.3 Results

The whole body SAR was calculated as 2.42 W/kg. This value was close to the whole body SAR value indicated in the scanner's log file (2.36 W/kg). To simplify the presentation of the large volume of temperature rise vs. time data obtained for all various conditions, crucial figures that summarizes many experiments were shown in the following sections.

5.3.1 Effect of Coaxial Cable Length on RF Heating

During the initial experiments, it was observed that the coaxial cable length that connects the matching-detuning circuit box of each active device channel to the scanner has a significant impact on heating results. Figure 5.4 shows the temperature rise graph when the guidewire was placed 5 inch away from the center of the scanner bore horizontally. The guidewire channels were connected to the scanner with 4 ft long coax cable and the insertion length was 35 cm. Figure 5.5 shows the temperature rise

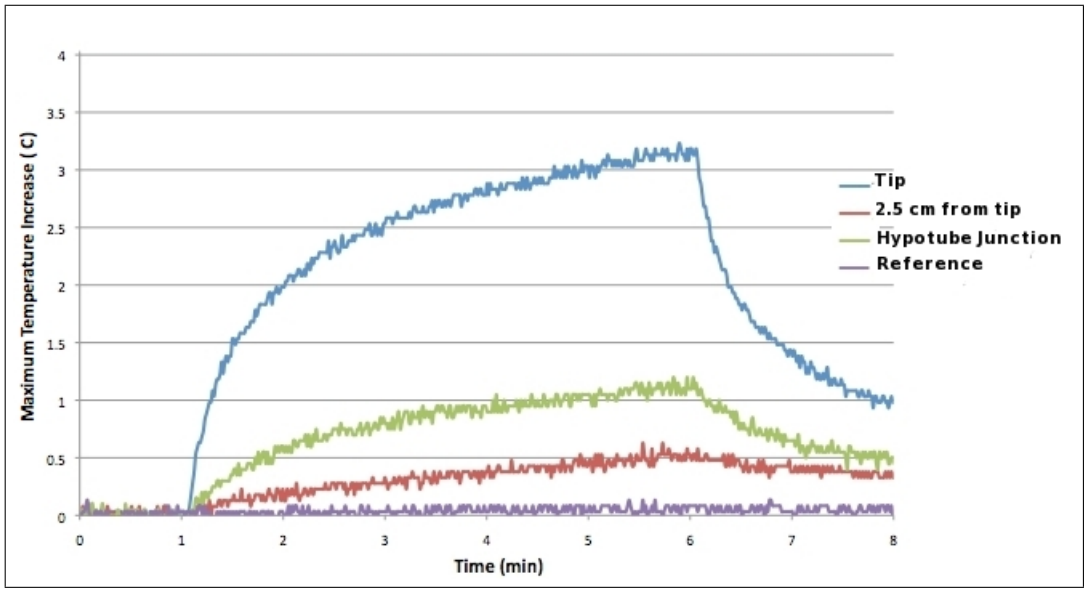

Figure 5.4 Measured temperature rise in the phantom during MR scan. The guidewire sample was placed 5 inch away from isocenter horizontally and the insertion length was 35 cm. The guidewire was connected to the scanner with 4 ft long coax cable.

graph of the same setup with the 6 ft long coaxial cable. The longer coax cable provided almost 0.9 ^{0}C decrease in temperature rise. The similar results were observed with different offset and insertion length configurations. So all experiments were performed by using only 6 ft long 50 Ω coaxial cable.

5.3.2 The RF Heating Test of the Active Guidewire within Vessel Phantom

The maximum temperature increase was observed when the insertion length was reached to 50 cm inside the vessel phantom. However, all measurement values were below than the critical temperature increase value that is 2 ^{0}C (Figure 5.6). The greatest temperature increase was 0.58 ^{0}C for 50 cm insertion length.

5.3.3 Effects of Horizontal Offset of the Guidewire Position on RF Heating

Figure 5.7 shows that the temperature rise depends on the insertion length when the guidewire was placed in the center of the phantom. The maximum amount

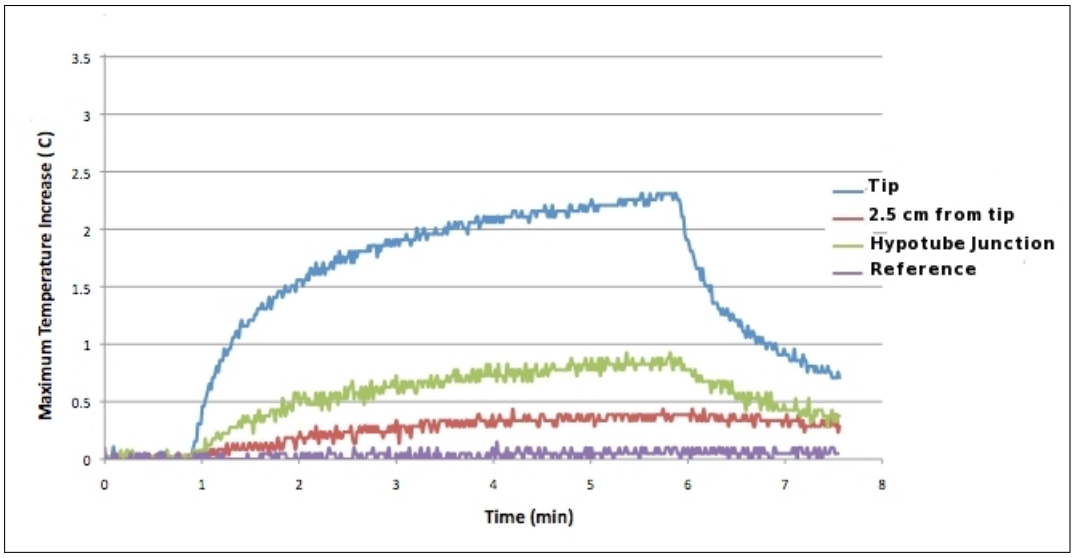

Figure 5.5 Measured temperature rise in the phantom during RF exposure. The guidewire sample was placed 5 inch away from isocenter horizontally and the insertion length was 35 cm. The guidewire was connected to the scanner with 6 ft long coax cable.

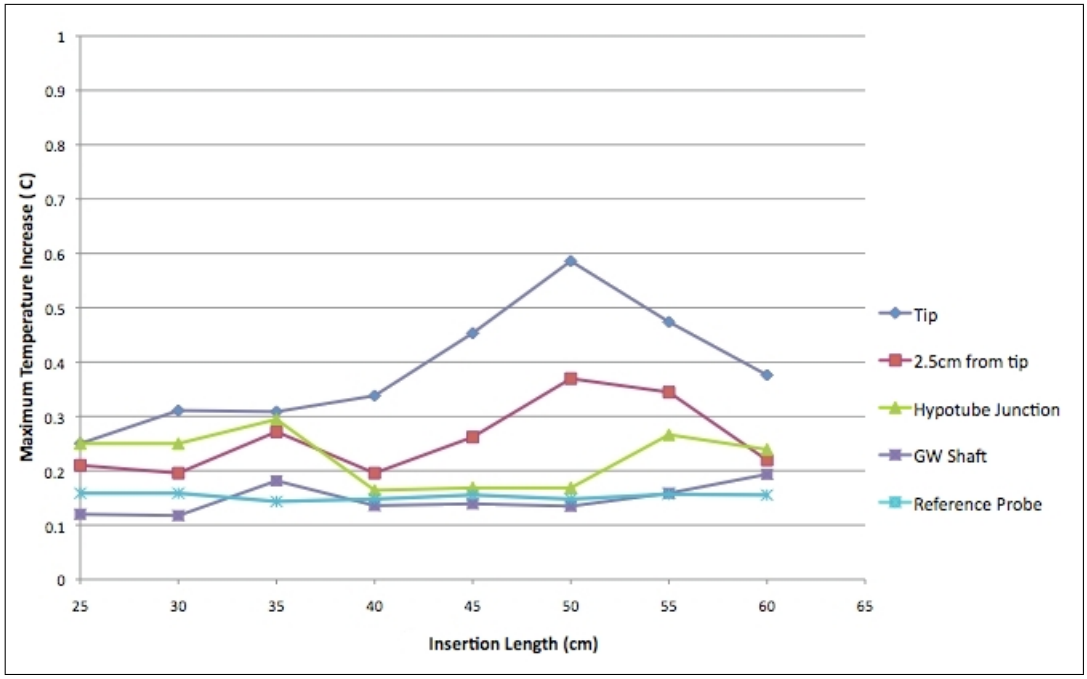

Figure 5.6 Measured temperature rise in the phantom relative to the guidewire insertion length within the vessel model.

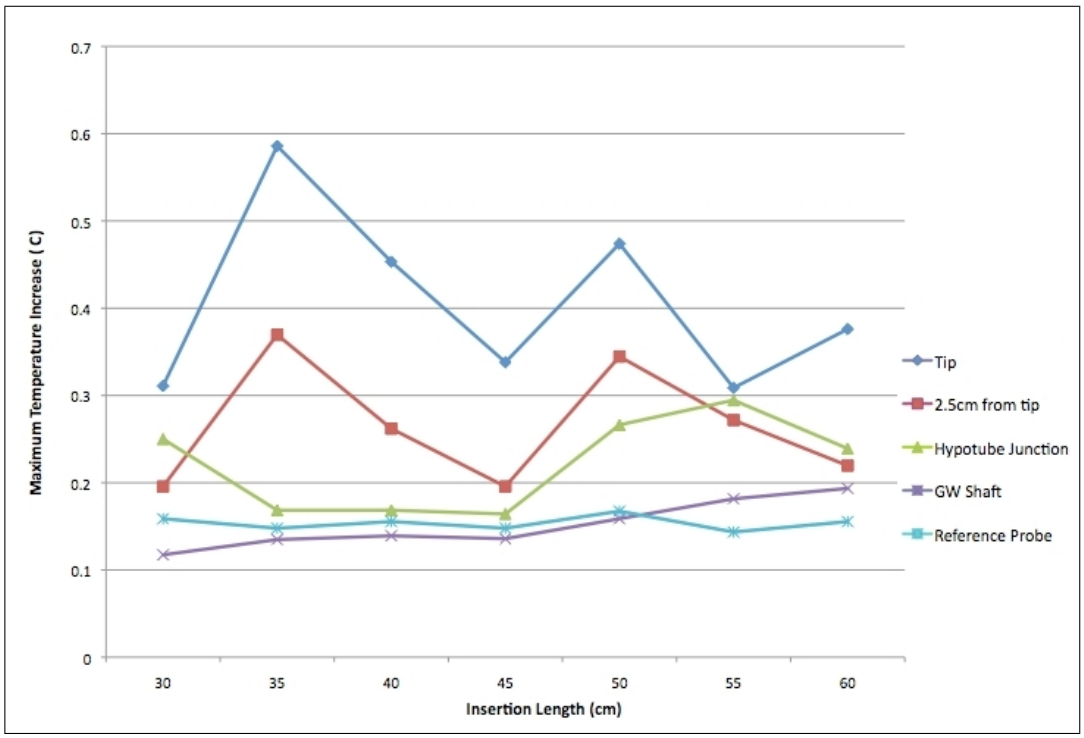

Figure 5.7 Measured temperature rise in the phantom relative to the guidewire insertion length. The guidewire was placed straight in the center of the phantom.

of temperature increase was observed when the insertion length reached to 35 cm. The 35 cm insertion length was used for each horizontal offset position during the experiments. Shown in Figure 5.8 is the increase in temperature, the maximum of which is approximately 2.6 ^{0}C, measured during RF exposure for different guidewire position. It was observed that temperature increase values were within the safe region until the guidewire was placed 5 inch away from the isocenter horizontally.

5.3.4 Effects of Insertion Length of the Guidewire placed at Maximum Allowed Horizontal Offset

The guidewire was placed 4 inch away from the center and the Figure 5.9 shows that the temperature rises for all insertion length configuration were below than the 2 ^{0}C. The maximum temperature increase was observed at 35 cm insertion length as expected.

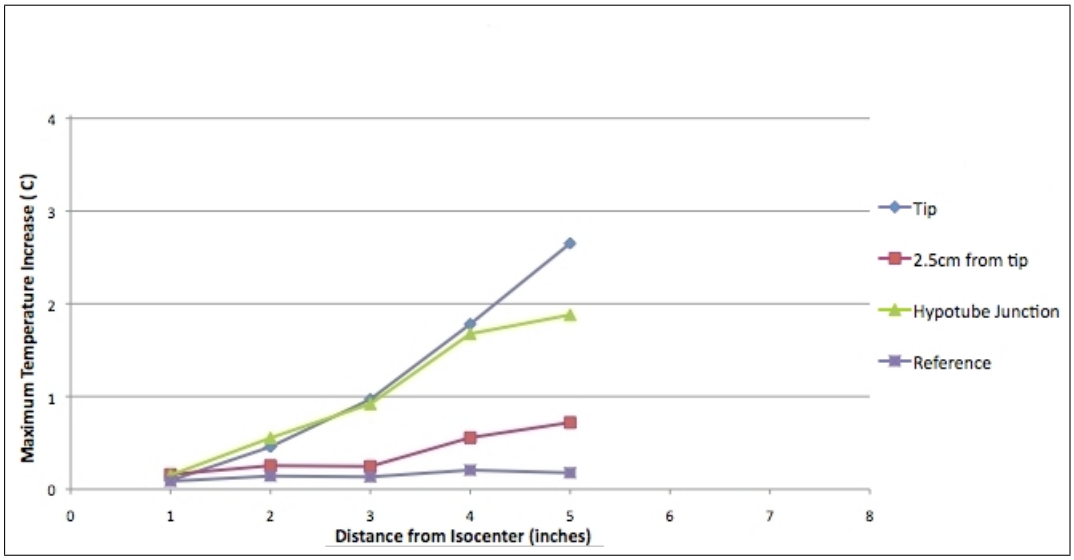

Figure 5.8 Temperature rise measured in the phantom for each horizontal offset position during RF exposure. The guidewire insertion length was 35 cm for each position.

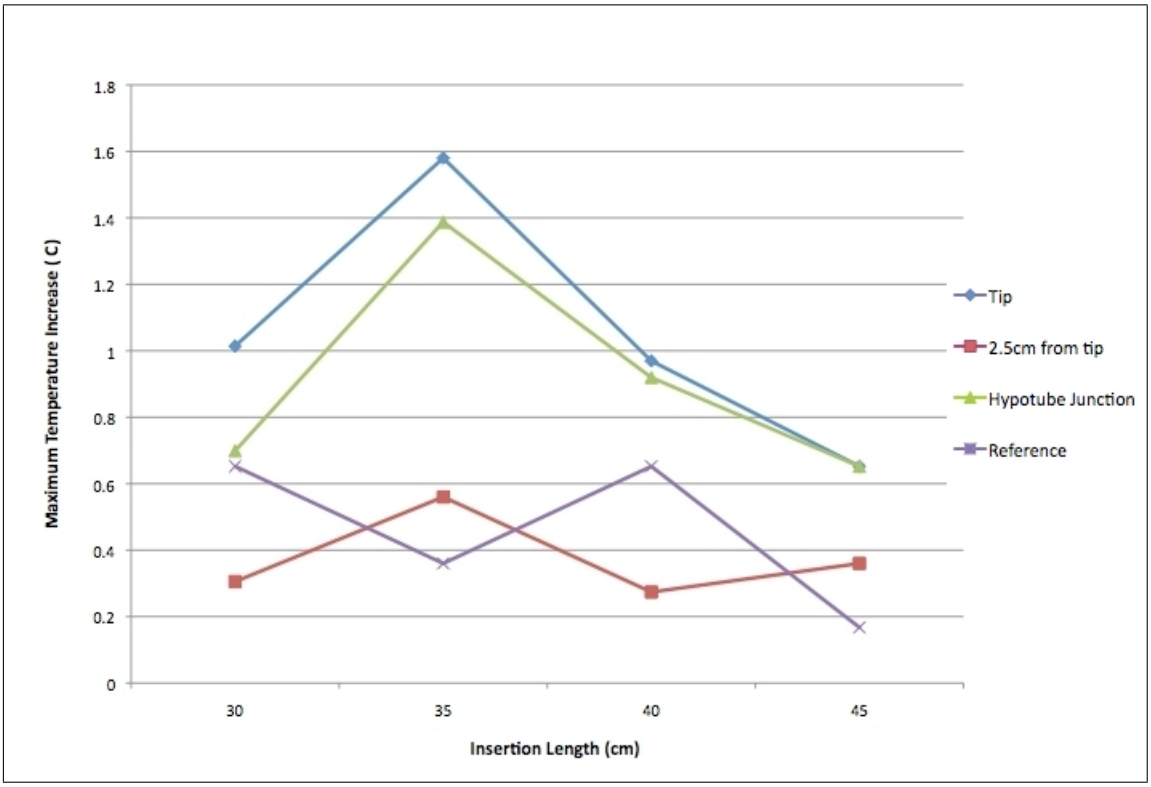

Figure 5.9 Temperature rise measured in the phantom for each insertion length during RF exposure. The guidewire was placed 4 inch away from the isocenter horizontally.

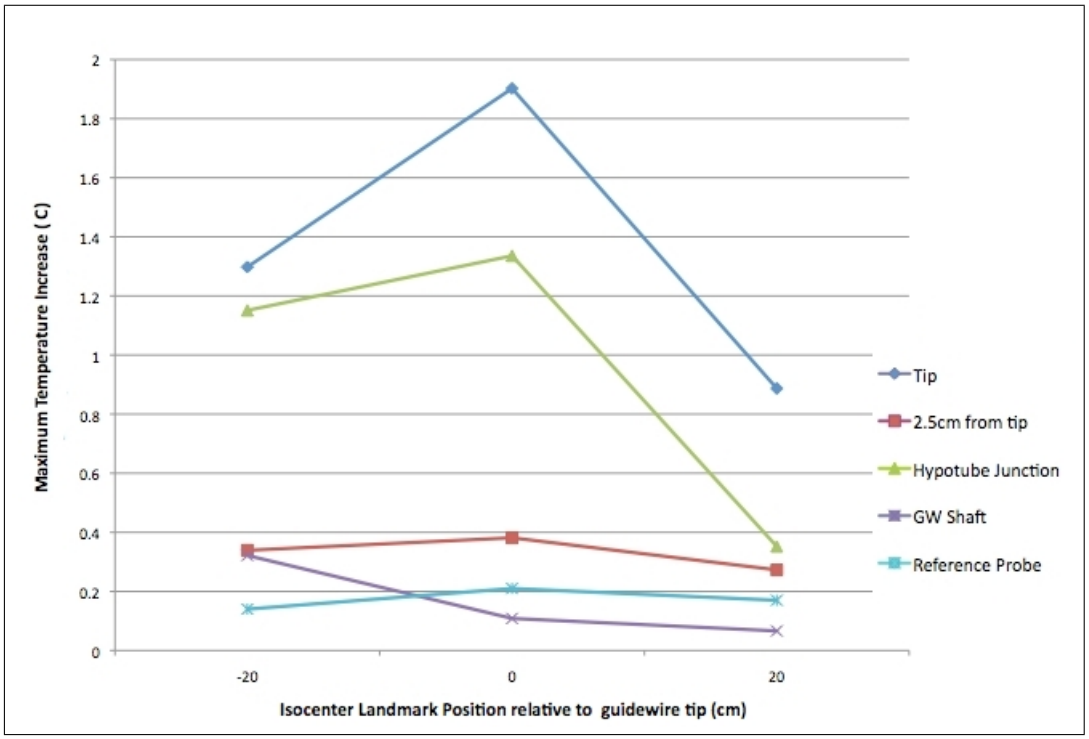

Figure 5.10 Temperature rise measured in the phantom for each isocenter landmark position relative to guidewire tip. Negative values represent the landmark offset towards to feet. The guidewire was placed 4 inch away from the isocenter horizontally and the insertion length was 35 cm.

5.3.5 Effects of Landmark Position for Active Guidewire Placed at the Maximum Allowed Horizontal Offset

Figure 5.10 represents the temperature rise graph for different landmark positions relative to the guidewire tip. The highest temperature increase was observed when the isocenter landmark was positioned to the guidewire tip. The temperature rise values were 1.9 ^{0}C and 1.3 ^{0}C for guidewire tip and loopless antenna junction point respectively. The overal temperature readings for the landmark position was offset towards feet were higher than the other offset side. Figure 5.11 shows the temperature increase values for the landmark position changed relative to the phantom center. In this setup, guidewire tip and junction point showed different temperature increase characteristics. While the reading at the tip was highest (1.58 ^{0}C) when the isocenter was landmarked 20 cm away from center towards to feet, the junction point reached the maximum temperature increase (1.18 ^{0}C) when the isocenter landmarked was positioned at the center of the phantom.

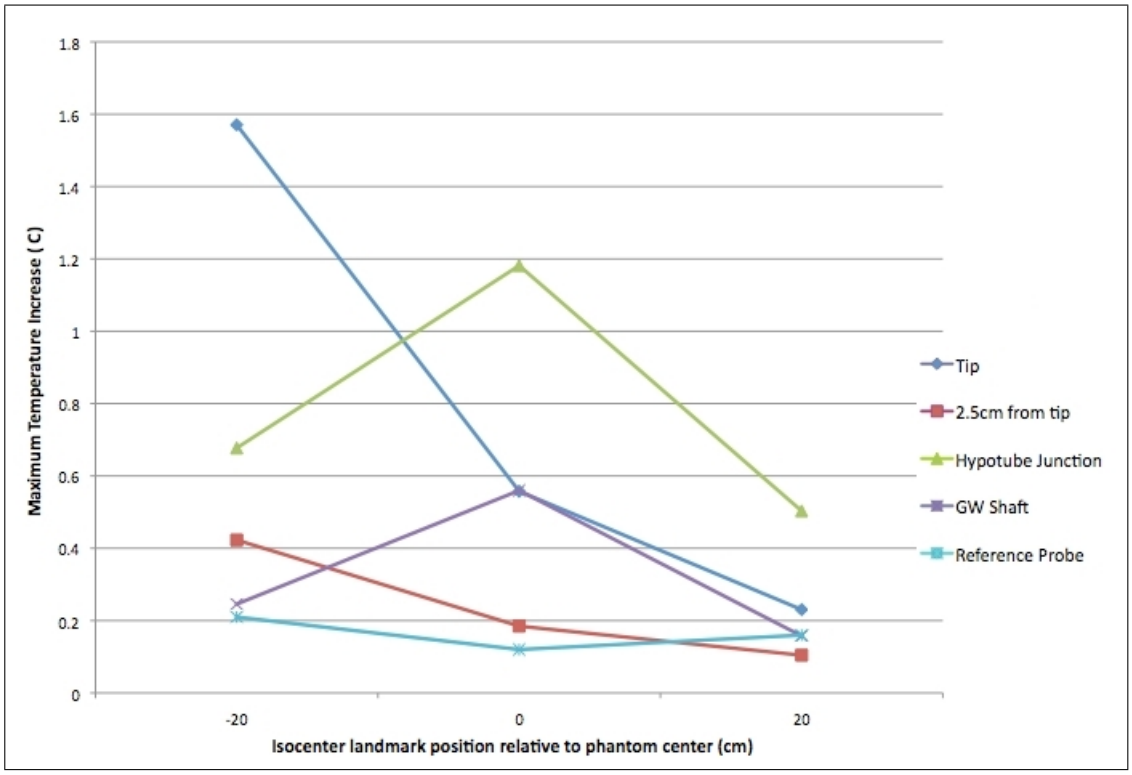

Figure 5.11 Temperature rise measurements for each isocenter landmark position relative to center of the phantom. Negative values represent the landmark offset towards to feet. The guidewire was placed 4 inch away from the isocenter horizontally and the insertion length was 35 cm.

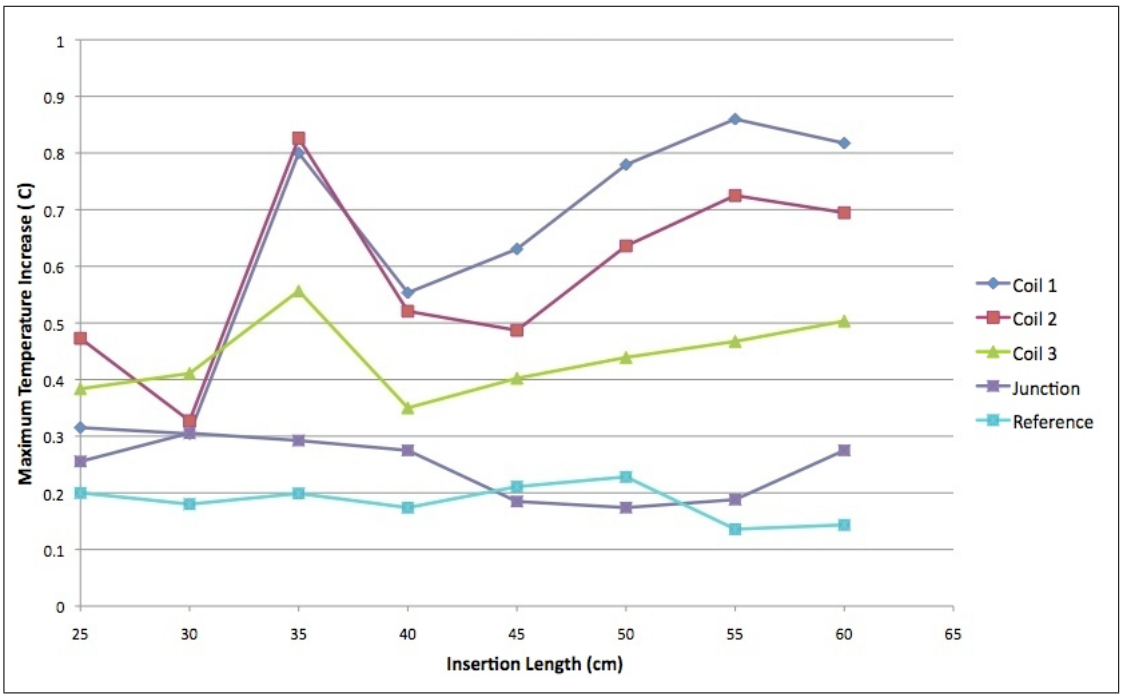

Figure 5.12 Measured temperature rise in the vessel phantom for each insertion length of the active catheter during RF exposure. The phantom was placed in the center of the MR table.

5.3.6 RF Heating Test of the Active Guiding Catheter within the Vessel Phantom

Figure 5.12 represents the temperature increase for the different insertion length of the active catheter that is placed inside the femoral vessel phantom. It was not observed any critical temperature increase for all insertion length values. The max temperature rises were 0.82 ^{0}C and 0.86 ^{0}C for 35 cm and 55 cm insertion length respectively.

5.3.7 Effects of Horizontal Offset of the Guiding Catheter Position on RF Heating

The temperature increase depends on the insertion length of the catheter that was placed in the center of the bore can be seen in Figure 5.13. The maximum temperature rise was observed for 35 cm insertion length. So the insertion length was fixed as 35 cm through all horizontal offset experiment setup. In Figure 5.14, the temperature

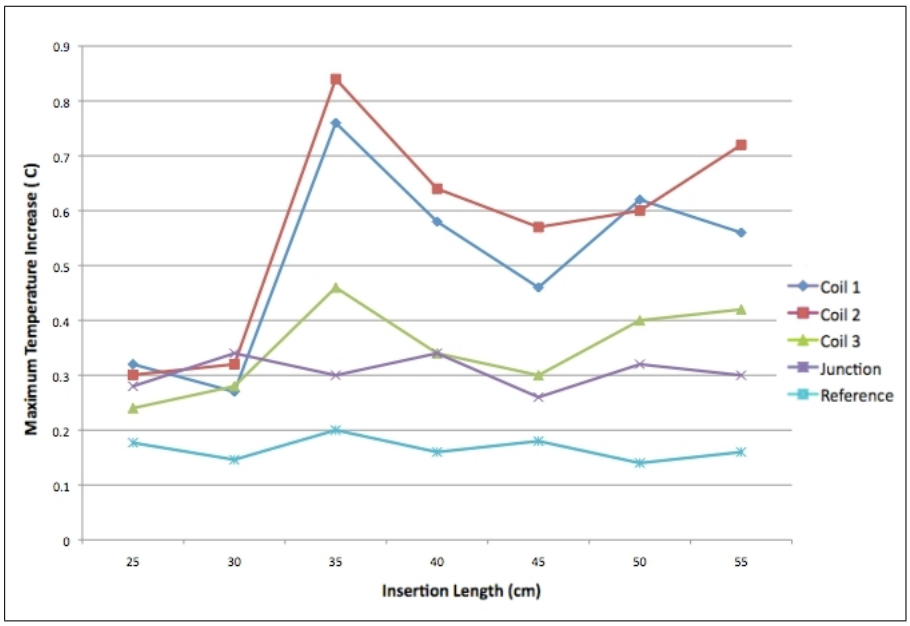

Figure 5.13 Measured temperature rise in the phantom for each insertion length of the active catheter during RF exposure. The active catheter was placed in the center of the phantom.

rise exceeded the 2 ^{0}C when the guiding catheter was positioned 5 inch away from the bore center.

5.3.8 Effects of Insertion Length of the Guiding Catheter placed in Maximum Allowed Horizontal Offset

The maximum temperature increase was observed at 35 cm insertion length as expected. The Figure 5.15 shows that all temperature rise values were within the safety region.

5.3.9 Effects of Landmark Position for Active Guiding Catheter Placed at the Maximum Allowed Horizontal Offset

Figure 5.16 represents the temperature rise graph for different landmark positions relative to the catheter tip position. The highest temperature increase was observed when the isocenter landmark was positioned to the distal tip. The temper-

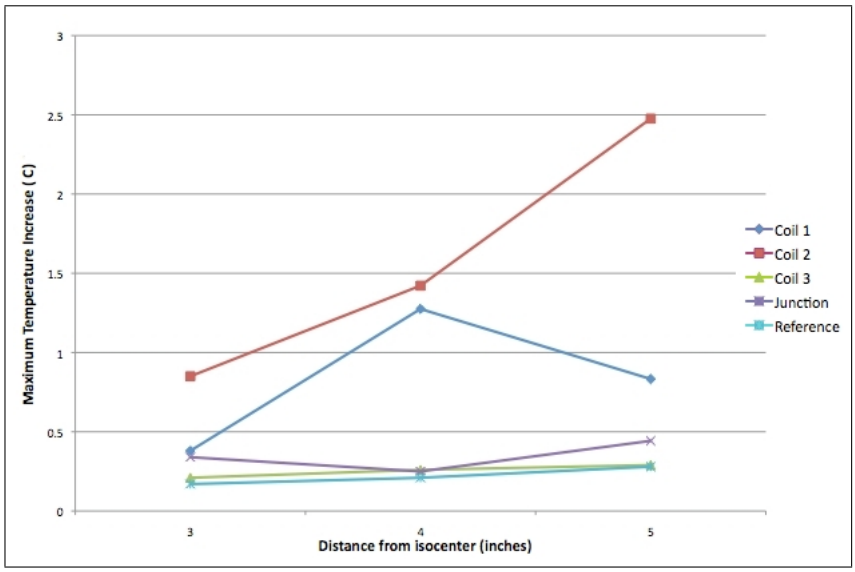

Figure 5.14 Measured temperature rise in the phantom for each horizontal offset of the active catheter during RF exposure. The phantom was placed in the center of the MR table.

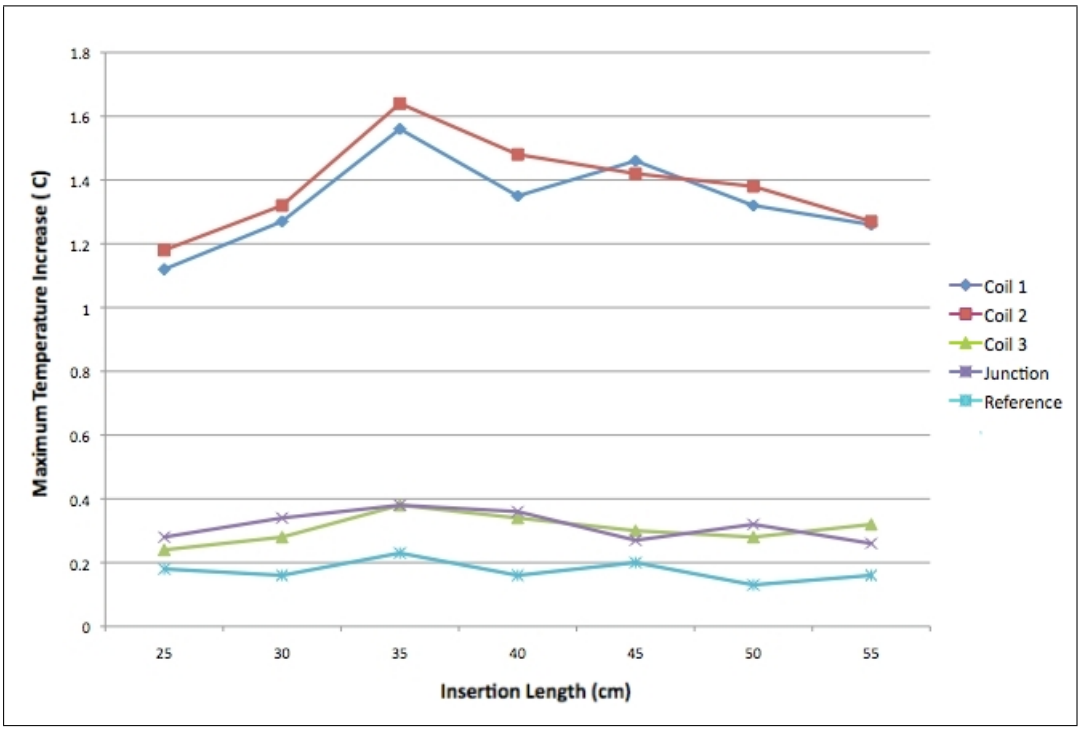

Figure 5.15 Temperature rise measured in the phantom for each insertion length during RF exposure. The active catheter was placed 4 inch away from the isocenter horizontally.

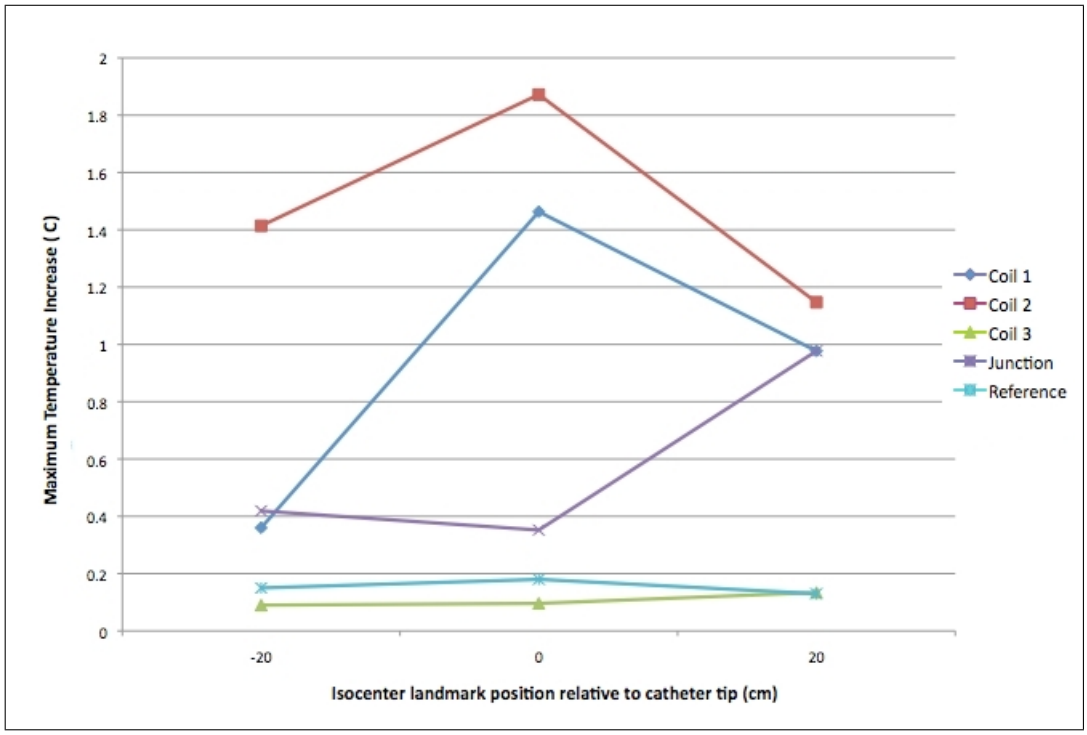

Figure 5.16 Temperature rise measured in the phantom for each isocenter landmark position relative to catheter distal tip. Negative values represent the landmark offset towards to feet. The guiding catheter was placed 4 inch away from the isocenter horizontally and the insertion length was 35 cm.

ature rise values were 1.88 ^{0} and 1.48 ^{0}C for catheter distal tip and loopless antenna junction point respectively. Figure 5.17 shows the temperature increase values for the landmark position changed relative to the phantom center. In this setup, first two distal tip coil showed higher temperature increase compare to junction point of the embedded loopless antenna design. The reading at the distal tip coils and junction point were highest (2.09 ^{0}C, 1.25 ^{0}C and 0.5 ^{0}C respectively) when the isocenter was landmarked 20 cm away from center towards to feet.

5.4 Discussion

The PAA, HEC and saline solution were considered as a phantom material for RF heating experiments. The most important criteria for chosing the phantom material was to have one that illustrates a worst case scenario for heating. The initial experiments with saline solution showed that it was not a good candidate for this pur-

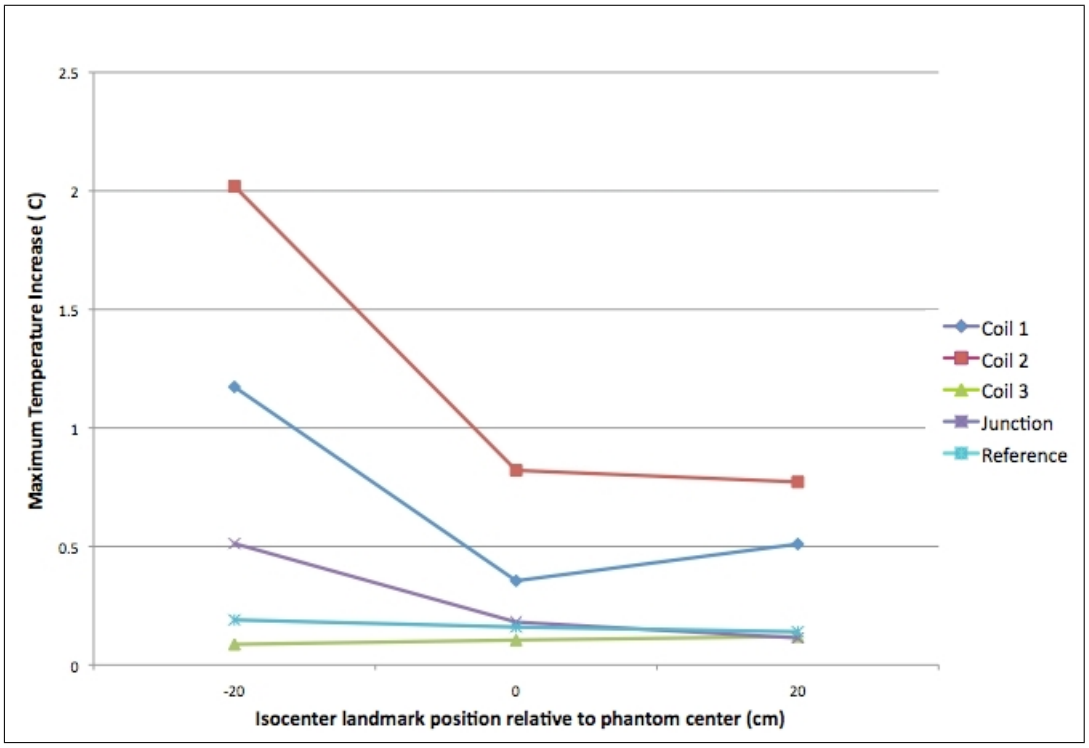

Figure 5.17 Temperature rise measurements for each isocenter landmark position relative to center of the phantom. Negative values represent the landmark offset towards to feet. The guiding catheter was placed 4 inch away from the isocenter horizontally and the insertion length was 35 cm.

pose. Although PAA and HEC gave similar increased heating and reduced convection results, PAA was used as a phantom material because of its less viscosity. It allowed to place femoral vessel model and change acrylic posts position within the phantom during horizontal offset experiments easily.

The overall results of all the experimental measurements in this work show that temperature increase strongly related with device geometry inside the phantom, mainly its offset position relative to the center and insertion length. It was shown that both active guidewire and guiding catheter can be used in a limited safety region without exceeding allowed temperature rise if a certain power level is not exceeded during each scan. The maximum allowed horizontal distance was determined as 4 inches away from the center. This distance allows to keep the device within the safety region for most of the cardiavascular applications. The 30-35 cm and 50-55 cm were determined as the critical insertion length during experiments.

6. Conclusions and Recommendations for Future Work

In the field of cardiovascular interventional MRI, this dissertation has focused on the development of clinical grade active guidewire and catheter that introduce essential tip and shaft visualization simultaneously.

It has been demonstrated that both the loop and loopless antenna design have been successfully utilized inside a 0.035 inch active guidewire package while comprising the essential mechanical characteristics. Simultaneous tip and shaft visibility will reduce the risk of injuring or perforating a vessel during interventional procedure. The main mechanical properties of the guidewire were compared with the representative commercial guidewires. All results were comparable except the very distal tip as expected. The active guidewire prototype was designed to have more rigid distal tip for initial target applications. The tightly wound solenoid coil wire diameter, inner rod diameter or the durometer of the Pebax insulation can be changed to modify distal tip flexibiliy. The other mechanical design considerations such as tensile strength, torque strength should be completed before FDA application for clinical use. Detuning elements like PIN diodes are integrated into the tuning and matching circuitry for each channel of our guidewire to reduce this heating risk. Each channel displayed with different color separately in the real-time MRI display. Device conspicuity and precision of MRI guidewire tip location were confirmed both in vitro and in vivo in pigs.

7 Fr active three channel multi purpose catheter was developed whose whole shaft can be visible under real time MRI by designing a loopless antenna by using current braiding layers embedded into catheter shaft. To visualize the shaft of the polymer catheter, a loopless antenna was designed using nitinol:copper braiding layer over the catheter shaft. These two wires were combined in composite braids and empirically determined an optimum braiding configuration of nitinol:copper 8:8. The resulting design is less stiff than a bigger size commercial steel introducer sheath system as expected, but highly conspicuous for interventional MRI. It was shown that the braiding layer of

the catheters can be manipulated to serve both mechanical and electrical purposes for active catheter design to to address the clinical requirement for whole-shaft visibility. In addition, the catheter shaft was designed to accommodate multiple transmission lines without increasing the catheter profile. Because copper that is relatively soft metal is very difficult to work with during braiding process, nitinol wires can be coated with gold to increase its conductivity and reduce attenuation during signal transmission.

The active device visualization can be a direct result of the amount of MR signal sensible to coil designs and resonant circuitry, both of which may be tuned to optimize SNR. A device with noticeable signal intensity in a phantom setting may not exhibit the same signal profile in vivo due to possible SNR distortion caused by surrounding tissue. To evaluate the active guidewire or catheter performance before animal experiments, SNR evaluation method was developed to compare identical designs by adapting both Single Magnitude Image Method and Double Acquisition Magnitude Image Method adopted from the NEMA standard. The custom made mold was prepared to make sure the device position is the same for each MRI scan. It helped to optimize each antenna channel performance by having quantitative feedback. Based on SNR computations comparing the two methods, there is no appreciable difference between the two noise estimates. The noise standard deviation from double acquisition magnitude image method was lower, resulting in higher SNR values, and the noise standard deviation error is lower as many more pixels are used in the calculation. The described SNR map construction algorithm is not limited to guide wires and catheters, it is applicable to any active device designed for interventional MR procedure, further assisting operators in quantifiable assessments of device profiling functionality. SNR maps of active multi channel devices were performed with the developed Matlab graphic user interface using two main magnitude image techniques. This Matlab GUI facilitated the comparison of active guidewire prototypes and objecive evaluation of any design modifications.

The heating experiments were performed to evaluate the RF safety of both developed active devices in use of targeted applications. It was aimed to determine safety region while manipulating the main parameters such as guidewire insertion length, horizontal offset position and isocenter landmark position relative to guidewire. It

was shown that temperature increase strongly related with device geometry inside the phantom, mainly its offset position relative to the center and insertion length and both active guidewire and guiding catheter can be used in a limited safety region without exceeding allowed temperature rise if a certain power level is not exceeded during each scan. The maximum allowed horizontal distance was determined as 4 inches away from the center. This distance allows to keep the device within the safety region for most of the cardiavascular applications. The 30-35 cm and 50-55 cm were determined as the critical insertion length during experiments. However, the RF safety of these devices can be improved by embedding temperature probe into device body. Low diameter as small as 0.25 mm fiber optic temperature probes are available today and they are flexible enough not to disturb mechanical properties of the active devices. Real time temperature monitoring during in vivo heating experiments may help to have better understanding of RF heating characteristics especially devices in motion.

REFERENCES

1. Carpenter, T. A., and E. J. Williams, "Magnetic Resonance Imaging- from basic knowledge to advanced strategies: hardware.," *Eur Radiol*, Vol. 9, no. 6, pp. 1015–1019, 1999.

2. Anzai, Y., "Preliminary experience with MR-guided thermal ablation of brain tumors," *American Journal of Neuroradiology*, Vol. 16, no. 1, pp. 39–48, 1995.

3. Fischer, U., R. Vosshenrich, D. Keating, H. Bruhn, W. Doler, J. Oestmann, and E. Grabbe, "MR-guided biopsy of suspect breast lesions with a simple stereotaxic add-on-device for surface coils," *Radiology*, Vol. 192, no. 1, p. 272, 1994.

4. Omary, R., R. Frayne, O. Unal, T. Warner, F. Korosec, C. Mistretta, C. Strother, and T. Grist, "MR-guided angioplasty of renal artery stenosis in a pig model: a feasibility study," *Journal of Vascular and Interventional Radiology*, Vol. 11, no. 3, pp. 373–381, 2000.

5. Wildermuth, S., J. Debatin, D. Leung, C. Dumoulin, R. Darrow, G. Uhlschmid, E. Hofmann, J. Thyregod, and G. Von Schulthess, "MR imaging-guided intravascular procedures: initial demonstration in a pig model," *Radiology*, Vol. 202, no. 2, p. 578, 1997.

6. Wacker, F., K. Reither, W. Ebert, M. Wendt, J. Lewin, and K. Wolf, "MR Image-guided Endovascular Procedures with the Ultrasmall Superparamagnetic Iron Oxide SH U 555 C as an Intravascular Contrast Agent: Study in Pigs 1," *Radiology*, Vol. 226, no. 2, pp. 459–464, 2003.

7. Bartels, L. W., and C. J. G. Bakker, "Endovascular interventional magnetic resonance imaging.," *Phys Med Biol*, Vol. 48, pp. R37–R64, Jul 2003.

8. Kleinerman, R. A., "Cancer risks following diagnostic and therapeutic radiation exposure in children.," *Pediatr Radiol*, Vol. 36 Suppl 14, pp. 121–125, Sep 2006.

9. Almen, T., "The etiology of contrast medium reactions.," *Invest Radiol*, Vol. 29 Suppl 1, pp. S37–S45, May 1994.

10. Lautin, E. M., N. J. Freeman, A. H. Schoenfeld, C. W. Bakal, N. Haramati, A. C. Friedman, J. L. Lautin, S. Braha, E. G. Kadish, and S. Sprayregen, "Radiocontrast-associated renal dysfunction: incidence and risk factors.," *AJR Am J Roentgenol*, Vol. 157, pp. 49–58, Jul 1991.

11. Yutzy, S. R., and J. L. Duerk, "Pulse sequences and system interfaces for interventional and real-time MRI.," *J Magn Reson Imaging*, Vol. 27, pp. 267–275, Feb 2008.

12. Niendorf, T., and D. K. Sodickson, "Highly accelerated cardiovascular MR imaging using many channel technology: concepts and clinical applications.," *Eur Radiol*, Vol. 18, pp. 87–102, Jan 2008.

13. Guttman, M. A., C. Ozturk, A. N. Raval, V. K. Raman, A. J. Dick, R. DeSilva, P. Karmarkar, R. J. Lederman, and E. R. McVeigh, "Interventional cardiovascular procedures guided by real-time MR imaging: an interactive interface using multiple slices, adaptive projection modes and live 3D renderings.," *J Magn Reson Imaging*, Vol. 26, pp. 1429–1435, Dec 2007.

14. Lederman, R. J., "Cardiovascular interventional magnetic resonance imaging," *Circulation*, Vol. 112, no. 19, pp. 3009–17, 2005.

15. Seppenwoolde, J.-H., M. A. Viergever, and C. J. G. Bakker, "Passive tracking exploiting local signal conservation: the white marker phenomenon.," *Magn Reson Med*, Vol. 50, pp. 784–790, Oct 2003.

16. Peeters, J. M., J.-H. Seppenwoolde, L. W. Bartels, and C. J. G. Bakker, "Development and testing of passive tracking markers for different field strengths and tracking speeds.," *Phys Med Biol*, Vol. 51, pp. N127–N137, Mar 2006.

17. Reitz JR, M. F., *Foundations of Electromagnetic Theory*, Addison-Wesley, 2000.

18. Bos, C., M. A. Viergever, and C. J. G. Bakker, "On the artifact of a subvoxel susceptibility deviation in spoiled gradient-echo imaging.," *Magn Reson Med*, Vol. 50, pp. 400–404, Aug 2003.

19. Miquel, M. E., S. Hegde, V. Muthurangu, B. J. Corcoran, S. F. Keevil, D. L. G. Hill, and R. S. Razavi, "Visualization and tracking of an inflatable balloon catheter using SSFP in a flow phantom and in the heart and great vessels of patients.," *Magn Reson Med*, Vol. 51, pp. 988–995, May 2004.

20. Krueger, J. J., P. Ewert, S. Yilmaz, D. Gelernter, B. Peters, K. Pietzner, A. Bornstedt, B. Schnackenburg, H. Abdul-Khaliq, E. Fleck, E. Nagel, F. Berger, and T. Kuehne, "Magnetic resonance imaging-guided balloon angioplasty of coarctation of the aorta: a pilot study.," *Circulation*, Vol. 113, pp. 1093–1100, Feb 2006.

21. Glowinski, A., G. Adam, A. Bücker, J. Neuerburg, J. J. van Vaals, and R. W. Günther, "Catheter visualization using locally induced, actively controlled field inhomogeneities.," *Magn Reson Med*, Vol. 38, pp. 253–258, Aug 1997.

22. Quick, H. H., M. O. Zenge, H. Kuehl, G. Kaiser, S. Aker, S. Massing, S. Bosk, and M. E. Ladd, "Interventional magnetic resonance angiography with no strings attached: wireless active catheter visualization.," *Magn Reson Med*, Vol. 53, pp. 446–455, Feb 2005.

23. Dumoulin, C. L., S. P. Souza, and R. D. Darrow, "Real-time position monitoring of invasive devices using magnetic resonance," *Magn Reson Med*, Vol. 29, no. 3, pp. 411–5, 1993.

24. Leung, D. A., J. F. Debatin, S. Wildermuth, G. C. McKinnon, D. Holtz, C. L. Dumoulin, R. D. Darrow, E. Hofmann, and G. K. von Schulthess, "Intravascular MR tracking catheter: preliminary experimental evaluation," *AJR Am J Roentgenol*, Vol. 164, no. 5, pp. 1265–70, 1995.

25. Lardo, A. C., E. R. McVeigh, P. Jumrussirikul, R. D. Berger, H. Calkins, J. Lima, and H. R. Halperin, "Visualization and temporal/spatial characterization of cardiac radiofrequency ablation lesions using magnetic resonance imaging.," *Circulation*, Vol. 102, pp. 698–705, Aug 2000.

26. Ocali, O., and E. Atalar, "Intravascular magnetic resonance imaging using a loopless catheter antenna," *Magn Reson Med*, Vol. 37, no. 1, pp. 112–8, 1997.

27. CA, B., *Antenna Theory*, John Wiley & Sons, 1997.

28. Atalar, E., P. A. Bottomley, O. Ocali, L. C. Correia, M. D. Kelemen, J. A. Lima, and E. A. Zerhouni, "High resolution intravascular MRI and MRS by using a catheter receiver coil," *Magn Reson Med*, Vol. 36, no. 4, pp. 596–605, 1996.

29. Hillenbrand, C. M., D. R. Elgort, E. Y. Wong, A. Reykowski, F. K. Wacker, J. S. Lewin, and J. L. Duerk, "Active device tracking and high-resolution intravascular MRI using a novel catheter-based, opposed-solenoid phased array coil.," *Magn Reson Med*, Vol. 51, pp. 668–675, Apr 2004.

30. Susil, R. C., C. J. Yeung, and E. Atalar, "Intravascular extended sensitivity (IVES) MRI antennas," *Magn Reson Med*, Vol. 50, no. 2, pp. 383–90, 2003.

31. McKinnon, G. C., J. F. Debatin, D. A. Leung, S. Wildermuth, D. J. Holtz, and G. K. von Schulthess, "Towards active guidewire visualization in interventional magnetic resonance imaging," *Magma*, Vol. 4, no. 1, pp. 13–8, 1996.

32. Guttman, M. A., R. J. Lederman, J. M. Sorger, and E. R. McVeigh, "Real-time volume rendered MRI for interventional guidance," *J Cardiovasc Magn Reson*, Vol. 4, no. 4, pp. 431–42, 2002.

33. Quick, H. H., H. Kuehl, G. Kaiser, D. Hornscheidt, K. P. Mikolajczyk, S. Aker, J. F. Debatin, and M. E. Ladd, "Interventional MRA using actively visualized catheters, True-FISP, and real-time image fusion," *Magn Reson Med*, Vol. 49, no. 1, pp. 129–37, 2003.

34. Rubin, D. L., A. V. Ratner, and S. W. Young, "Magnetic susceptibility effects and their application in the development of new ferromagnetic catheters for magnetic resonance imaging," *Invest Radiol*, Vol. 25, no. 12, pp. 1325–32, 1990.

35. Dick, A. J., V. K. Raman, A. N. Raval, M. A. Guttman, R. B. Thompson, C. Ozturk, D. C. Peters, A. M. Stine, V. J. Wright, W. H. Schenke, and R. J. Lederman, "Invasive human magnetic resonance imaging: feasibility during revascularization in a combined xmr suite.," *Catheter Cardiovasc Interv*, Vol. 64, pp. 265–274, Mar 2005.

36. Karmarkar, P. V., D. L. Kraitchman, I. Izbudak, L. V. Hofmann, L. C. Amado, D. Fritzges, R. Young, M. Pittenger, J. W. Bulte, and E. Atalar, "Mr-trackable intramyocardial injection catheter," *Magn Reson Med*, Vol. 51, no. 6, pp. 1163–72, 2004.

37. Zhang, Q., M. Wendt, A. J. Aschoff, J. S. Lewin, and J. L. Duerk, "A multielement RF coil for MRI guidance of interventional devices," *J Magn Reson Imaging*, Vol. 14, no. 1, pp. 56–62, 2001.

38. Liu H, T. C., "A comprehensive interventional society for magnetic resonance in medicine (abstract).," *Proceedings of the 5th scientific meeting and exhibition of the International Society for Magnetic resonance in Medicine*, p. 1921, 1997.

39. Hegde, S., M. E. Miquel, R. Boubertakh, D. Gilderdale, V. Muthurangu, S. F. Keevil, I. Young, D. L. Hill, and R. S. Razavi, "Interactive MR imaging and tracking of catheters with multiple tuned fiducial markers," *J Vasc Interv Radiol*, Vol. 17, no. 7, pp. 1175–9, 2006.

40. Bowick, C., *RF Circuit Design*, Newnes, 1997.

41. Sinnema, W., *Electronic Transmission Technology*, Prentice Hall, 1988.

42. Qiu, B., A.-M. El-Sharkawy, V. Paliwal, P. Karmarkar, F. Gao, E. Atalar, and X. Yang, "Simultaneous radiofrequency (RF) heating and magnetic resonance (MR) thermal mapping using an intravascular MR imaging/RF heating system.," *Magn Reson Med*, Vol. 54, pp. 226–230, Jul 2005.

43. Hoult DI, R. R., "Signal-to-noise ratio of the nuclear magnetic resonance experiment," *Journal of Magnetic Resonance*, Vol. 24, pp. 71–85, 1976.

44. Qiu, B., P. Karmarkar, C. Brushett, F. Gao, R. Kon, S. Kar, E. Atalar, and X. Yang, "Development of a 0.014-inch magnetic resonance imaging guidewire," *Magn Reson Med*, Vol. 53, no. 4, pp. 986–90, 2005.

45. Kajfez, D., and E. J. Hwan, "Q-factor measurement with network analyzer," *IEEE Transactions on microwave theory and techniques*, Vol. 32, pp. 666–670, Jul 1984.

46. Ladd, M. E., G. G. Zimmermann, H. H. Quick, J. F. Debatin, P. Boesiger, G. K. von Schulthess, and G. C. McKinnon, "Active MR visualization of a vascular guidewire in vivo," *J Magn Reson Imaging*, Vol. 8, no. 1, pp. 220–5, 1998.

47. Burl, M., G. A. Coutts, D. J. Herlihy, R. Hill-Cottingham, J. F. Eastham, J. V. Hajnal, and I. R. Young, "Twisted-pair RF coil suitable for locating the track of a catheter," *Magn Reson Med*, Vol. 41, no. 3, pp. 636–8, 1999.

48. Yeung, C. J., P. Karmarkar, and E. R. McVeigh, "Minimizing RF heating of conducting wires in MRI," *Magn Reson Med*, Vol. 58, no. 5, pp. 1028–34, 2007.

49. Henkelman, R. M., "Measurement of signal intensities in the presence of noise in MR images.," *Med Phys*, Vol. 12, no. 2, pp. 232–233, 1985.

50. Henkelman, R., and M. Bronskill, *Artifacts in magnetic resonance imaging*, Pergamon Press, 1987.

51. "Determination of Signal-to-Noise Ratio (SNR) in Diagnostic Magnetic Resonance Imaging," 2008. National Electrical Manufacturers Association (NEMA) standard.

52. Constantinides, C. D., E. Atalar, and E. R. McVeigh, "Signal-to-noise measurements in magnitude images from NMR phased arrays.," *Magn Reson Med*, Vol. 38, pp. 852–857, Nov 1997.

53. Edelstein, W. A., P. A. Bottomley, and L. M. Pfeifer, "A signal-to-noise calibration procedure for NMR imaging systems.," *Med Phys*, Vol. 11, no. 2, pp. 180–185, 1984.

54. Gudbjartsson, H., and S. Patz, "The Rician distribution of noisy MRI data.," *Magn Reson Med*, Vol. 34, pp. 910–914, Dec 1995.

55. Kaufman, L., D. M. Kramer, L. E. Crooks, and D. A. Ortendahl, "Measuring signal-to-noise ratios in MR imaging.," *Radiology*, Vol. 173, pp. 265–267, Oct 1989.

56. Sijbers, J., A. J. den Dekker, J. V. Audekerke, M. Verhoye, and D. V. Dyck, "Estimation of the noise in magnitude MR images.," *Magn Reson Imaging*, Vol. 16, no. 1, pp. 87–90, 1998.

57. Elgort, D. R., E. Y. Wong, C. M. Hillenbrand, F. K. Wacker, J. S. Lewin, and J. L. Duerk, "Real-time catheter tracking and adaptive imaging.," *J Magn Reson Imaging*, Vol. 18, pp. 621–626, Nov 2003.

58. Guttman, M. A., C. Ozturk, A. N. Raval, V. K. Raman, A. J. Dick, R. DeSilva, P. Karmarkar, R. J. Lederman, and E. R. McVeigh, "Interventional cardiovascular procedures guided by real-time MR imaging: an interactive interface using multiple slices, adaptive projection modes and live 3D renderings," *J Magn Reson Imaging*, Vol. 26, no. 6, pp. 1429–35, 2007.

59. Nayak, K. S., C. H. Cunningham, J. M. Santos, and J. M. Pauly, "Real-time cardiac MRI at 3 tesla.," *Magn Reson Med*, Vol. 51, pp. 655–660, Apr 2004.

60. Santos, J. M., G. A. Wright, and J. M. Pauly, "Flexible real-time magnetic resonance imaging framework.," *Conf Proc IEEE Eng Med Biol Soc*, Vol. 2, pp. 1048–1051, 2004.

61. Godart, F., J. P. Beregi, L. Nicol, B. Occelli, A. Vincentelli, V. Daanen, C. Rey, and J. Rousseau, "MR-guided balloon angioplasty of stenosed aorta: in vivo evaluation using near-standard instruments and a passive tracking technique.," *J Magn Reson Imaging*, Vol. 12, pp. 639–644, Oct 2000.

62. Le Blanche, A., J. Rossert, M. Wassef, B. Lévy, J. Bigot, and F. Boudghene, "MR-guided PTA in experimental bilateral rabbit renal artery stenosis and MR angiography follow-up versus histomorphometry," *CardioVascular and Interventional Radiology*, Vol. 23, no. 5, pp. 368–374, 2000.

63. Spuentrup, E., A. Ruebben, T. Schaeffter, W. J. Manning, R. W. Günther, and A. Buecker, "Magnetic resonance–guided coronary artery stent placement in a swine model.," *Circulation*, Vol. 105, pp. 874–879, Feb 2002.

64. Bartels, L., C. Bos, R. van der Weide, H. Smits, C. Bakker, and M. Viergever, "Placement of an inferior vena cava filter in a pig guided by high-resolution MR fluoroscopy at 1.5 T," *Journal of Magnetic Resonance Imaging*, Vol. 12, no. 4, pp. 599–605, 2000.

65. Adam, G., J. Neuerburg, A. Bücker, A. Glowinski, D. Vorwerk, A. Stargardt, J. J. V. Vaals, and R. W. Günther, "Interventional magnetic resonance. initial clinical experience with a 1.5-tesla magnetic resonance system combined with c-arm fluoroscopy.," *Invest Radiol*, Vol. 32, pp. 191–197, Apr 1997.

66. Manke, C., W. R. Nitz, B. Djavidani, M. Strotzer, M. Lenhart, M. Völk, S. Feuerbach, and J. Link, "MR imaging-guided stent placement in iliac arterial stenoses: a feasibility study.," *Radiology*, Vol. 219, pp. 527–534, May 2001.

67. Razavi, R., D. L. G. Hill, S. F. Keevil, M. E. Miquel, V. Muthurangu, S. Hegde, K. Rhode, M. Barnett, J. van Vaals, D. J. Hawkes, and E. Baker, "Cardiac catheterisation guided by MRI in children and adults with congenital heart disease.," *Lancet*, Vol. 362, pp. 1877–1882, Dec 2003.

68. Fink, C., M. Bock, R. Umathum, S. Volz, S. Zuehlsdorff, R. Grobholz, H.-U. Kauczor, and P. Hallscheidt, "Renal embolization: feasibility of magnetic resonance-guidance using active catheter tracking and intraarterial magnetic resonance angiography.," *Invest Radiol*, Vol. 39, pp. 111–119, Feb 2004.

69. Ozturk, C., M. Guttman, E. R. McVeigh, and R. J. Lederman, "Magnetic resonance imaging-guided vascular interventions.," *Top Magn Reson Imaging*, Vol. 16, pp. 369–381, Oct 2005.

70. Bock, M., and F. K. Wacker, "MR-guided intravascular interventions: techniques and applications.," *J Magn Reson Imaging*, Vol. 27, pp. 326–338, Feb 2008.

71. Bakker, C. J., R. M. Hoogeveen, J. Weber, J. J. van Vaals, M. A. Viergever, and W. P. Mali, "Visualization of dedicated catheters using fast scanning techniques with potential for MR-guided vascular interventions," *Magn Reson Med*, Vol. 36, no. 6, pp. 816–20, 1996.

72. Kozerke, S., and S. Plein, "Accelerated CMR using zonal, parallel and prior knowledge driven imaging methods.," *J Cardiovasc Magn Reson*, Vol. 10, no. 1, p. 29, 2008.

73. Magnusson, P., E. Johansson, S. Mansson, J. S. Petersson, C.-M. Chai, G. Hansson, O. Axelsson, and K. Golman, "Passive catheter tracking during interventional MRI using hyperpolarized 13C.," *Magn Reson Med*, Vol. 57, pp. 1140–1147, Jun 2007.

74. Edelman, R. R., P. Storey, E. Dunkle, W. Li, A. Carrillo, A. Vu, and T. J. Carroll, "Gadolinium-enhanced off-resonance contrast angiography.," *Magn Reson Med*, Vol. 57, pp. 475–484, Mar 2007.

75. Dharmakumar, R., I. Koktzoglou, R. Tang, K. Harris, N. Beohar, and D. Li, "Off-resonance positive contrast imaging of a passive endomyocardial catheter in swine," *Physics in Medicine and Biology*, Vol. 53, no. 13, pp. N249–N257, 2008.

76. Kuehne, T., R. Fahrig, and K. Butts, "Pair of resonant fiducial markers for localization of endovascular catheters at all catheter orientations.," *J Magn Reson Imaging*, Vol. 17, pp. 620–624, May 2003.

77. Wong, E. Y., Q. Zhang, J. L. Duerk, J. S. Lewin, and M. Wendt, "An optical system for wireless detuning of parallel resonant circuits," *J Magn Reson Imaging*, Vol. 12, no. 4, pp. 632–8, 2000.

78. Eggers, H., S. Weiss, P. Boernert, and P. Boesiger, "Image-based tracking of optically detunable parallel resonant circuits," *Magn Reson Med*, Vol. 49, no. 6, pp. 1163–74, 2003.

79. Celik, H., A. Uluturk, T. Tali, and E. Atalar, "A catheter tracking method using reverse polarization for MR-guided interventions," *Magn Reson Med*, Vol. 58, no. 6, pp. 1224–31, 2007.

80. Zhang, Q., M. Wendt, A. J. Aschoff, L. Zheng, J. S. Lewin, and J. L. Duerk, "Active MR guidance of interventional devices with target-navigation.," *Magn Reson Med*, Vol. 44, pp. 56–65, Jul 2000.

81. Quick, H. H., J. M. Serfaty, H. K. Pannu, R. Genadry, C. J. Yeung, and E. Atalar, "Endourethral MRI.," *Magn Reson Med*, Vol. 45, pp. 138–146, Jan 2001.

82. Serfaty, J. M., X. Yang, P. Aksit, H. H. Quick, M. Solaiyappan, and E. Atalar, "Toward MRI-guided coronary catheterization: visualization of guiding catheters, guidewires, and anatomy in real time.," *J Magn Reson Imaging*, Vol. 12, pp. 590–594, Oct 2000.

83. Sathyanarayana, S., P. Aksit, A. Arepally, P. V. Karmarkar, M. Solaiyappan, and E. Atalar, "Tracking planar orientations of active MRI needles.," *J Magn Reson Imaging*, Vol. 26, pp. 386–391, Aug 2007.

84. Kutz, M., *Standard handbook of biomedical engineering and design*, McGraw-Hill New York, 2003.

85. Martin, R., and C. Johnson, "Engineering considerations of catheters for intravascular ultrasonic measurements," in *SPIE*, Vol. 1068, pp. 198–206, 1989.

86. Carey, J., D. Emery, and P. McCracken, "Buckling test as a new approach to testing flexural rigidities of angiographic catheters," *Journal of Biomedical Materials Research Part B: Applied Biomaterials*, no. 1, 2006.

87. Carey, J., A. Fahim, and M. Munro, "Design of braided composite cardiovascular catheters based on required axial, flexural, and torsional rigidities," *J Biomed Mater Res B Appl Biomater*, Vol. 70, no. 1, pp. 73–81, 2004.

88. "Determination of signal to noise ratio and image uniformity for single-channel non-volume coils in diagnostic magnetic resonance imaging (MRI)," 2008. National Electrical Manufacturers Association (NEMA) standard.

89. Kellman, P., and E. R. McVeigh, "Image reconstruction in SNR units: a general method for SNR measurement.," *Magn Reson Med*, Vol. 54, pp. 1439–1447, Dec 2005.

90. Yeung, C., R. Susil, and E. Atalar, "RF heating due to conductive wires during MRI depends on the phase distribution of the transmit field," *Magnetic Resonance in Medicine*, Vol. 48, no. 6, pp. 1096–1098, 2002.

91. Nitz, W. R., A. Oppelt, W. Renz, C. Manke, M. Lenhart, and J. Link, "On the heating of linear conductive structures as guide wires and catheters in interventional MRI.," *J Magn Reson Imaging*, Vol. 13, pp. 105–114, Jan 2001.

92. Yeung, C. J., R. C. Susil, and E. Atalar, "RF safety of wires in interventional MRI: using a safety index.," *Magn Reson Med*, Vol. 47, pp. 187–193, Jan 2002.

93. Wildermuth, S., C. L. Dumoulin, T. Pfammatter, S. E. Maier, E. Hofmann, and J. F. Debatin, "MR-guided percutaneous angioplasty: assessment of tracking safety, catheter handling and functionality.," *Cardiovasc Intervent Radiol*, Vol. 21, no. 5, pp. 404–410, 1998.

94. Konings, M. K., L. W. Bartels, H. F. Smits, and C. J. Bakker, "Heating around intravascular guidewires by resonating RF waves.," *J Magn Reson Imaging*, Vol. 12, pp. 79–85, Jul 2000.

95. Polk, C., and E. Postow, *Handbook of biological effects of electromagnetic fields*, CRC press, 1996.

96. "Guidance for the submission of premarket notifivations for magnetic resonance diagostic devices.," 1998. United States Departent of Health and Human Services, Food and Drug Administration.

97. "Characterization of the specific absorption rate for magnetic resonance imaging systems," 2008. National Electrical Manufacturers Association (NEMA) standard.

98. Konings, M., S. Weiss, C. Bakker, L. Bartels, and W. Mali, "Catheters and guidewires in interventional MRI: problems and solutions," *Medicamundi*, Vol. 45, no. 1, pp. 31–39, 2001.

99. Pennes, H. H., "Analysis of tissue and arterial blood temperatures in the resting human forearm. 1948.," *J Appl Physiol*, Vol. 85, pp. 5–34, Jul 1998.

100. Yeung, C. J., and E. Atalar, "Rf transmit power limit for the barewire loopless catheter antenna.," *J Magn Reson Imaging*, Vol. 12, pp. 86–91, Jul 2000.

101. "Standard test method for measurement of radio frequency induced heating near passive implants during magnetic resonance imaging." American Society for Testing and Materials (ASTM) standard.

102. Pictet, J., R. Meuli, S. Wicky, and J. J. van der Klink, "Radiofrequency heating effects around resonant lengths of wire in MRI.," *Phys Med Biol*, Vol. 47, pp. 2973–2985, Aug 2002.

103. Gabriel, C., "Compilation of the dielectric properties of body tissues at RF and microwave frequencies. Brooks Air Force Technical Report AL," *OETE (1996–0037)*, 1996.